



**EXPERIMENTAL EVALUATION OF THE AERODYNAMIC
DESIGN CRITERIA AND PERFORMANCE OF A
TRANSONIC LUDWIG TUBE WIND TUNNEL**

**VON KÁRMÁN GAS DYNAMICS FACILITY
ARNOLD ENGINEERING DEVELOPMENT CENTER
AIR FORCE SYSTEMS COMMAND
ARNOLD AIR FORCE STATION, TENNESSEE 37389**

October 1975

Final Report for Period July 1974 — March 1975

Approved for public release; distribution unlimited.

Prepared for

**DIRECTORATE OF CIVIL ENGINEERING
ARNOLD ENGINEERING DEVELOPMENT CENTER
ARNOLD AIR FORCE STATION, TENNESSEE 37389**

NOTICES

When U. S. Government drawings specifications, or other data are used for any purpose other than a definitely related Government procurement operation, the Government thereby incurs no responsibility nor any obligation whatsoever, and the fact that the Government may have formulated, furnished, or in any way supplied the said drawings, specifications, or other data, is not to be regarded by implication or otherwise, or in any manner licensing the holder or any other person or corporation, or conveying any rights or permission to manufacture, use, or sell any patented invention that may in any way be related thereto.

Qualified users may obtain copies of this report from the Defense Documentation Center.

References to named commercial products in this report are not to be considered in any sense as an endorsement of the product by the United States Air Force or the Government.

This report has been reviewed by the Information Office (OI) and is releasable to the National Technical Information Service (NTIS). At NTIS, it will be available to the general public, including foreign nations.

APPROVAL STATEMENT

This technical report has been reviewed and is approved for publication.

FOR THE COMMANDER



CHARLES V. BENNETT
Facility Development
Division
Directorate of Civil Engineering



ROLAND R. GARREN
Colonel, USAF
Director of Civil Engineering

UNCLASSIFIED

REPORT DOCUMENTATION PAGE		READ INSTRUCTIONS BEFORE COMPLETING FORM
1. REPORT NUMBER AEDC-TR-75-132	2. GOVT ACCESSION NO.	3. RECIPIENT'S CATALOG NUMBER
4. TITLE (and Subtitle) EXPERIMENTAL EVALUATION OF THE AERODYNAMIC DESIGN CRITERIA AND PERFORMANCE OF A TRANSONIC LUDWIEG TUBE WIND TUNNEL		5. TYPE OF REPORT & PERIOD COVERED Final Report-July 1974 - March 1975
		6. PERFORMING ORG. REPORT NUMBER
7. AUTHOR(s) M. O. Varner, D. W. Stallings, and R. F. Starr, ARO, Inc.		8. CONTRACT OR GRANT NUMBER(s)
9. PERFORMING ORGANIZATION NAME AND ADDRESS Arnold Engineering Development Center (DE) Arnold Air Force Station, Tennessee 37389		10. PROGRAM ELEMENT, PROJECT, TASK AREA & WORK UNIT NUMBERS Program Element 63723F
11. CONTROLLING OFFICE NAME AND ADDRESS Arnold Engineering Development Center (DYFS) Arnold Air Force Station Tennessee 37389		12. REPORT DATE October 1975
		13. NUMBER OF PAGES 107
14. MONITORING AGENCY NAME & ADDRESS (if different from Controlling Office)		15. SECURITY CLASS. (of this report) UNCLASSIFIED
		15a. DECLASSIFICATION/DOWNGRADING SCHEDULE N/A
16. DISTRIBUTION STATEMENT (of this Report) Approved for public release; distribution unlimited.		
17. DISTRIBUTION STATEMENT (of the abstract entered in Block 20, if different from Report)		
18. SUPPLEMENTARY NOTES Available in DDC		
19. KEY WORDS (Continue on reverse side if necessary and identify by block number) experimental data aerodynamics transonic flow Reynolds number test facilities Ludwieg tube development		
20. ABSTRACT (Continue on reverse side if necessary and identify by block number) This report presents the results of studies into the details of the aerodynamic processes which govern the operation of a Ludwieg tube transonic wind tunnel. Experimental studies, conducted in a pilot facility, complimented by theoretical analyses of optimized transonic nozzle design, optimized starting process with minimum start times, plenum volume and auxiliary flow system response and design, steady-state and transient pressure-		

UNCLASSIFIED

UNCLASSIFIED

20. ABSTRACT (Continued)

loading distributions on the test section porous walls and ejector flaps, and diffuser design are presented. Emphasis is placed on understanding and describing the fundamental mechanisms which govern the aerodynamic behavior of the tunnel, allowing for the establishment of meaningful performance estimates that are applicable to a full-scale facility.

UNCLASSIFIED

PREFACE

The work presented herein was conducted by the Arnold Engineering Development Center (AEDC), Air Force Systems Command (AFSC), under Program Element 63723F. The results were obtained by ARO, Inc. (a subsidiary of Sverdrup & Parcel and Associates, Inc.), contract operator of AEDC, AFSC, Arnold Air Force Station, Tennessee. The research was conducted under ARO Project No. V37A-32A. The authors of this report were M. O. Varner, D. W. Stallings, and R. F. Starr, ARO, Inc., and the manuscript (ARO Control No. VKF-TR-75-82) was submitted for publication on June 19, 1975.

CONTENTS

	<u>Page</u>
1.0 INTRODUCTION	9
2.0 EXPERIMENTAL APPARATUS	
2.1 Pilot Transonic Tunnel, Pilot HIRT	10
2.2 Instrumentation	11
3.0 NOZZLE DESIGN AND PRESSURE DISTRIBUTIONS	16
4.0 TEST SECTION AERODYNAMICS	19
5.0 PLENUM VOLUME AND THE AUXILIARY FLOW SYSTEM	25
5.1 Plenum Volume	25
5.2 Auxiliary Flow during the Starting Process	26
5.3 A Model for Minimum Start Time	27
5.4 Steady-State Auxiliary Flow	30
6.0 TEST SECTION WALL AND FLAP AERODYNAMICS LOADS	37
6.1 Experimental Procedure	37
6.2 Experimental Results, Test Section Wall Loading	38
6.3 Wall Loading Process Model	40
6.4 Flap Loading	44
7.0 DIFFUSER PERFORMANCE	
7.1 Experimental Procedure and Results	73
7.2 Diffuser Modeling	77
8.0 CONCLUDING REMARKS	101
REFERENCES	102

ILLUSTRATIONS

Figure

2.1 Pilot HIRT Elevation Line Drawing	12
2.2 Cross-Sectional View of Pilot HIRT Nozzle, Test Section, Diffuser, and Main Valve System	13
2.3 Interior View of Pilot HIRT Test Section	14
2.4 Plenum Exhaust System	14
2.5 Exterior View of Pilot HIRT Plenum Shell and Nozzle	15

<u>Figure</u>	<u>Page</u>
3.1 Theoretical Mach Number Distributions in Pilot HIRT Nozzle	17
3.2 Nozzle Static Pressure Tubing Installation	18
3.3 Nozzle Static Pressure Measurements	18
4.1 Centerline Pipe Installation	22
4.2 Test Section Mach Number Distributions - 165 msec at a Wall Porosity of 4.5 percent	23
4.3 Standard Deviation for Data in the Test Region at a Wall Porosity of 4.5 percent	24
4.4 Plenum - Test Section Mach Number Relationships at a Wall Porosity of 4.5 percent	24
5.1 Plenum Static Pressure Time History Showing the Effect of Auxiliary Flow on Tunnel Start Time	31
5.2 Minimum Start Time as a Function of Plenum Volume with and without Auxiliary Flow	31
5.3 Auxiliary Flow Area Time History during the Starting Process in Pilot HIRT	32
5.4 Excess Auxiliary Flow Area Required to Achieve Minimum Start time	32
5.5 Excess Auxiliary Flow Area as a Function of Time Required to Minimize Start Time, Theoretical	33
5.6 Minimum Start Time as a Function of the Pressure Ratio, μ , Theoretical	33
5.7 Average Excess Flow Area Ratio as a Function of the Nondimensional Start Time for a Fixed Plenum Volume Ratio, Theoretical	34
5.8 Plenum Volume Ratio as a Function of the Nondimensional Start Time for a Given Average Excess Flow Area Ratio, Theoretical	34
5.9 Steady-State Auxiliary Flow Requirements in Pilot HIRT	35
5.10 Total Auxiliary Flow Requirements Required to Attain a Specified Mach Number and Start Time in Pilot HIRT	36

<u>Figure</u>	<u>Page</u>
6.1 Installation View Showing Back of Porous Wall with Differential Transducers	50
6.2 Schematic of Test Section Showing Location of Differential Transducers	50
6.3 Detail of Instrumented Ejector Flap	51
6.4 Wall Loading during the Starting Process at Five Stations as Shown in Fig. 6.2 for Variations in Wall Porosity with $p_{ch} = 100$ psia, $A_f/A_{ts} = 0.0$, 12-in. SSV Starting Device	52
6.5 Wall Loading during the Starting Process at Five Stations as Shown in Fig. 6.2 for Variations in the Charge Pressure, p_{ch} , at a Porosity of 4.5 percent, $A_f/A_{ts} = 0.0$, 12-in. SSV Starting Device.	53
6.6 Wall Loading during the Starting Process at Three Stations as Shown in Fig. 6.2 for Variable Flap Opening at a Wall Porosity of 4.5 percent, $V_p/V_{ts} = 2.5$, 16-in. SSV Starting Device	54
6.7 Maximum Wall Loading during the Starting Process as a Function of Flap Opening and Axial Position Measured from Back of Test Section for a Wall Porosity of 4.5 percent, $V_p/V_{ts} = 2.5$, 16-in. SSV Starting Device	55
6.8 Maximum Wall Loading during the Starting Process as a Function of Flap Opening and Axial Position Measured from Back of Test Section for a Wall Porosity of 4.5 percent, $V_p/V_{ts} = 2.5$, Diaphragm Starting Device	55
6.9 Maximum Wall Loading during the Starting Process as a Function of Porosity, τ_w , Flap Opening and Axial Position for $V_p/V_{ts} = 2.5$, Diaphragm Starting Device	56
6.10 Schematic of Plenum Discharge Process	57
6.11 Model of Plenum Discharge Process.	57
6.12 Illustration of Main Valve Opening as a Function of Time	57
6.13 Simplified Wave Diagram for Diffuser and Valve	58

<u>Figure</u>	<u>Page</u>
6.14 Pressure Histories of Start Process at Stations A and B as Depicted in Fig. 6.13	58
6.15 Nondimensional Differential Pressure across the Porous Wall as a Function of Nondimensional Time, t/τ_T , for Various Values of τ_V/τ_T , Theoretical	59
6.16 Maximum Differential Pressure Coefficient and the Ratio τ_V/τ_T versus the Nondimensional Peak Time, τ_p/τ_T , Theoretical	60
6.17 Maximum Differential Pressure Coefficient as a Function of the Ratio τ_V/τ_T , Theoretical	61
6.18 Illustration of Model of Axial Pressure Differential.	62
6.19 Porous Wall Flow Coefficient versus Porosity, τ_w	62
6.20 Ejector Flap Flow Coefficient versus Area Ratio, A_f/A_{ts}	62
6.21 Maximum Differential Pressure Coefficient as a Function of the Ratio τ_V/τ_T Showing Data for $\tau_V = 5.5$ msec, Diaphragm Case	63
6.22 Maximum Differential Pressure Coefficient versus A_f/A_{ts} Showing Influence of τ_w for $\tau_V = 100$ msec, $V_p/V_{ts} = 2.5$, Theoretical	64
6.23 Time Histories of Flap Loading at Station 7 (See Figs. 6.2 and 6.3) for Variations in Characteristic Valve Opening Time, τ_V , and Flap Open Area, A_f/A_{ts}	65
6.24 Streamwise Maximum Flap Differential Pressure Coefficient during the Starting Process with $\tau_w = 4.5$ percent, $V_p/V_{ts} = 2.5$, and $\dot{w}_A = 0$	66
6.25 $(\Delta p/p_{ch})_{max}$ Averaged over Flap Length as a Function of τ_V/τ_T	67
6.26 $(\Delta p/p_{ch})_{max}$ at Downstream Edge of Flap as a Function of τ_V/τ_T	68
6.27 Ratio of Maximum Flap Load to Steady-State Flap Load as a Function of A_f/A_{ts} for Two Cases of Diffuser Flow in Pilot HIRT	69

<u>Figure</u>	<u>Page</u>
6.28 Schematic of Ejector Flaps for Pilot and Envisioned Full-Scale HIRT Showing Geometric Differences	70
6.29 HIRT Ejector Flap Load Distribution for Flap in Full Open Position during Starting Process for Pivot Point as Shown	70
6.30 Peak $(\Delta p/p_{ch})_{max}$ for HIRT with Distribution as Given in Fig. 6.29 for $A_f/A_{ts} > 0.25$	71
6.31 Maximum Pressure Coefficient Distribution at the Upstream and Downstream Edge of a Typical HIRT Flap Configuration as a Function of A_{DE}/A_{UE}	72
7.1 Pilot HIRT Diffuser System	80
7.2 Ejector Flap Section of Pilot HIRT	81
7.3 Installation View of Sector in Upstream End of Diffuser of Pilot HIRT	82
7.4 Pilot HIRT Diffuser Area Distribution	82
7.5 Pressure Distributions for All Ejector Flaps Closed, $t = 170$ msec, with No Auxiliary Suction, Sector Installed ($\alpha_s = 0$)	83
7.6 Pressure Distributions for All Ejector Flaps Open 0.2 in., $t = 170$ msec, with No Auxiliary Suction	84
7.7 Pressure Distributions for All Ejector Flaps Open 0.4 in., $t = 170$ msec, with No Auxiliary Suction	87
7.8 Pressure Distributions for All Ejector Flaps Open, $t = 170$ msec, with Auxiliary Suction	89
7.9 Influence of Number of Ports Opened on Pressures in Pilot HIRT Diffuser with Sector Removed	91
7.10 Influence of Sector on Diffuser Pressures	93

<u>Figure</u>	<u>Page</u>
7.11 Effect of Ejector Flap Opening on Operating Conditions in Plenum and Manifold without Auxiliary Suction, $t = 170 \text{ msec}$, $p_{t_\infty} = 75 \text{ psia}$	95
7.12 Effects of Sector and Auxiliary Suction on Overall Total-Pressure Ratio, $t = 170 \text{ msec}$, $p_{t_\infty} = 75 \text{ psia}$	96
7.13 Mach Number Function in Mass Flow Equation for Uniform Flow	97
7.14 Mach Number Function for Total-Pressure Ratio with Choked Flow	97
7.15 Critical Total-Pressure Ratio Providing a Choked Flow at the Discharge ($M_d = 1$)	98
7.16 Critical or Minimum Stagnation Pressure Required to Choke at Discharge Area	98
7.17 Maximum Pressure Ratio and Entrance Mach Number for Valve Manifold with Flow-Turning Losses	99
7.18 Estimated Losses in Diffuser System for Range of Discharge Areas at $M_\infty = 1.0$	100
NOMENCLATURE	104

1.0 INTRODUCTION

Experimental and analytical research has been carried out at the Arnold Engineering Development Center (AEDC) in the detailed evaluation of a transonic high Reynolds number facility utilizing a Ludwig tube air storage system (Ref. 1). Previous experimental results and evaluations of this type of facility are given in Refs. 2, 3, and 4. These reports demonstrated the feasibility of utilizing this concept to achieve a high quality, very high Reynolds number, transonic test medium having high quality flow with spatial and temporal uniformity during the few seconds of useful test time.

This report presents the results of continued studies into the details of the aerodynamic processes which govern the operation of a Ludwig tube transonic tunnel. Refinements in the configuration of the flow-conditioning channel (nozzle, test section and diffuser), which represent an improvement over Ref. 4, will be described. Detailed analyses of the starting process, ejector flap performance, and wall loadings during the starting process are covered. Emphasis has been placed on understanding and describing the fundamental mechanisms which govern the aerodynamic behavior such that meaningful performance estimates can be made for facilities of different size or slightly different configuration.

2.0 EXPERIMENTAL APPARATUS

2.1 PILOT TRANSONIC TUNNEL, PILOT HIRT

The AEDC-Von Kármán Gas Dynamics Facility (VKF) Pilot High Reynolds Number Facility (Pilot HIRT) is a one-thirteenth scale model of a high Reynolds number transonic facility which was proposed for construction at AEDC. A schematic drawing of the pilot tunnel is given in Fig. 2.1. It can be charged to 800 psia and produces a maximum stagnation pressure of about 500 psia in the transonic speed range. The Ludwig tube storage system (charge tube) is 13.9 in. in diameter and is 111 ft long. A transition section with a contraction ratio of 2.25 channels the flow from the circular charge tube into a rectangular test section which is 7.34 by 9.15 in. The test section-plenum chamber is shown in a more detailed schematic in Figure 2.2. The porous walls are of conventional design with 60-deg inclined holes. The porosity can be varied manually by moving one porous plate relative to another (two plates constitute a wall). When the holes are fully aligned, the porosity is ten percent and the cutoff plate motion is upstream to reduce porosity. The test section is shown photographically in Fig. 2.3. An ejector flap section is located at the back of the porous plates. The flaps are on all four walls and can be set to a greater opening during the tunnel starting process and then reduced during the steady run. The plenum chamber which encloses the test section has a volume which is about 1.8 times the test section volume (neglecting the volume of the wall support structure). The plenum is exhausted directly to atmosphere through the choked orifice-valve system shown schematically in Fig. 2.4. The desired auxiliary flow rate through the plenum system is obtained by adjusting the orifice and by opening or closing the quick-acting valve shown in the figure. The plenum exhaust flow is initiated by rupturing a diaphragm in the line. The volume of the plenum chamber and the plenum exhaust lines is about 2.5 times the test section volume. A photograph of the nozzle, plenum shell, and plenum exhaust lines is presented in Fig. 2.5. A model support section, diffuser, and main starting device are located downstream of the test section (Fig. 2.2). Three main starting devices were used in the experimental work which will be described. A 16-in. -diam sliding sleeve valve (see Fig. 2.2) was used in many of the experiments which required the accurate simulation of an aerodynamically clean diffuser system. This valve opens in about 80 msec. A 12-in. -diam fast acting sliding sleeve valve which opens in 20 to 30 msec was also used (Fig. 2.2). For tests which required effective valve opening times somewhat shorter

than these, a diaphragm was employed as the main starting device essentially (0 msec opening time). All of the exhaust air is channeled out of the building through the exhaust sphere (Fig. 2.1).

After the tunnel is pressurized to the desired pressure, a tunnel run is initiated by opening the main starting device and the plenum exhaust system if Mach numbers above 0.95 are desired. The duration of the first cycle of the run of this pilot tunnel is about 185 msec and the tunnel starting process consumes the first 30 to 80 msec of this time. The duration of the steady portion of the run is about 100 to 150 msec. The tunnel operating conditions are established from a stagnation pressure measurement made in the charge tube just ahead of the nozzle and from a plenum chamber pressure measurement made at the plenum shell wall near the center of model rotation (see Fig. 2.2).

2.2 INSTRUMENTATION

The pressure measurements required during this series of experiments were obtained with Tabor[®] strain-gage and small Kulite[®] semiconductor transducers located external to the tunnel and connected to the pressure orifice in the tunnel through tubes about 0.07-in. ID and 2 ft. long. The tunnel monitoring pressure measurements (stagnation and plenum pressures) were obtained similarly. The response time of these tubing configurations to a step input is about 20 msec at the pressures at which Pilot HIRT operates. A few test section wall static pressure and tunnel monitoring pressure measurements were also obtained with the transducer located at the point of measurement to eliminate tube lag and give a truer picture of time variants during the starting process and run.

The analog voltage output of the transducer is amplified, multiplexed, and converted to digital form at about 20,000 samples per second. The raw data is stored in a minicomputer for reduction after the run. One data sample is obtained on each channel about every 2 msec. The possible precision of measurement of this transducer-data recording system is better than 0.25 percent. However the high-speed data recording system was installed just prior to most of the experiments which will be described and this high precision was not achieved until some system errors were eliminated. The analog signals from selected channels are also paralleled to an oscillograph to allow a quick postrun evaluation of the data in visual form and to display the more rapid time variants in the starting process for which one sample every 2 msec does not reveal an adequate picture.



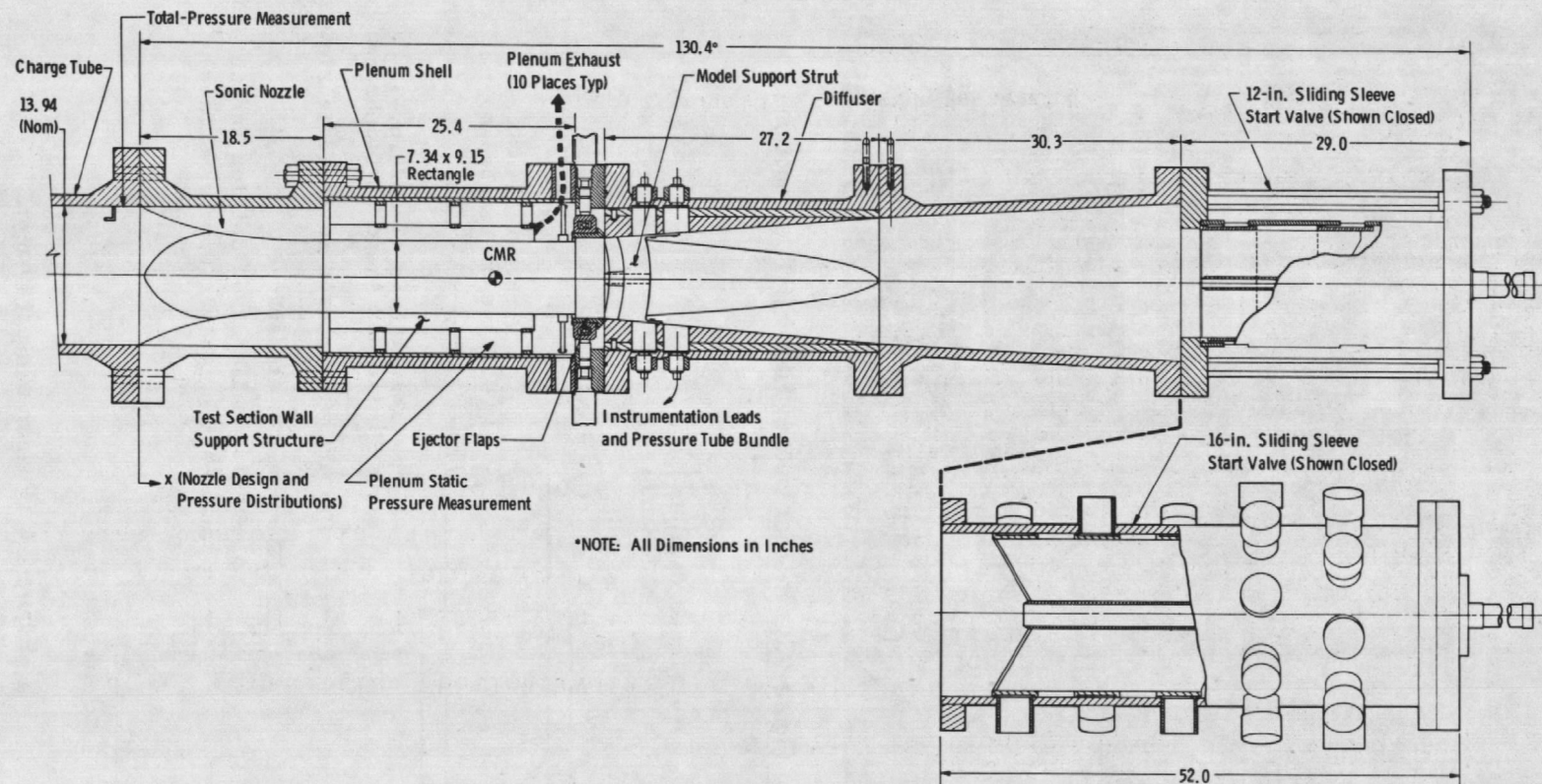


Figure 2.2. Cross-sectional view of Pilot HIRT nozzle, test section, diffuser, and main valve system.

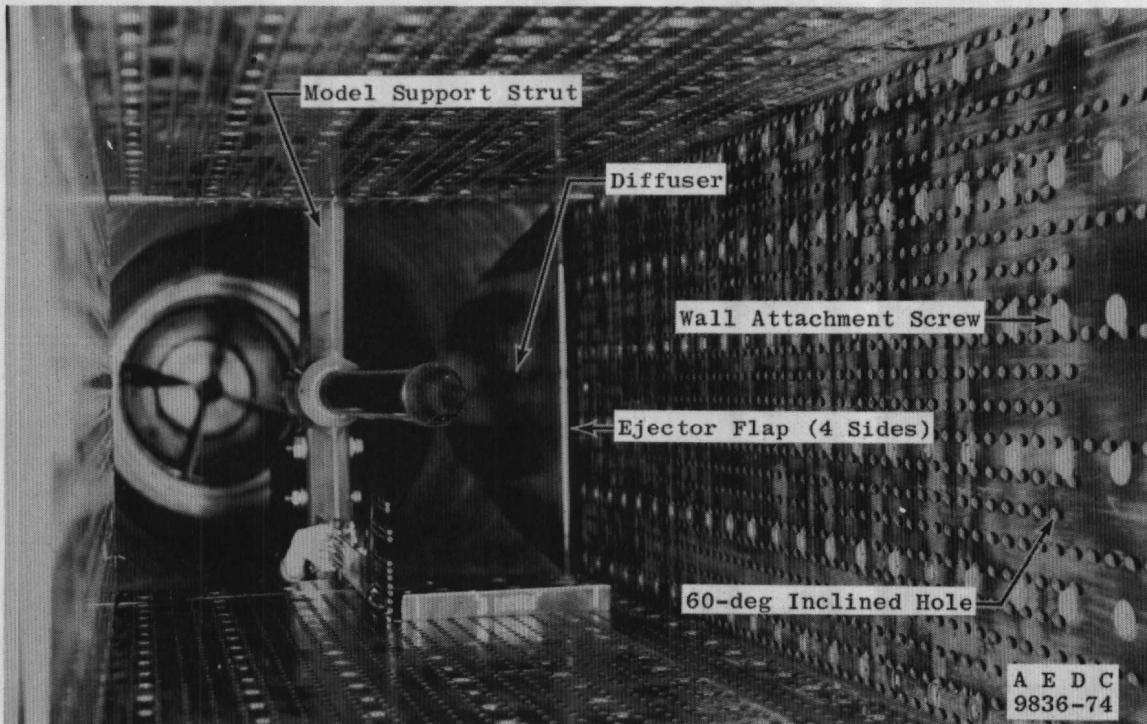


Figure 2.3. Interior view of Pilot HIRT test section.

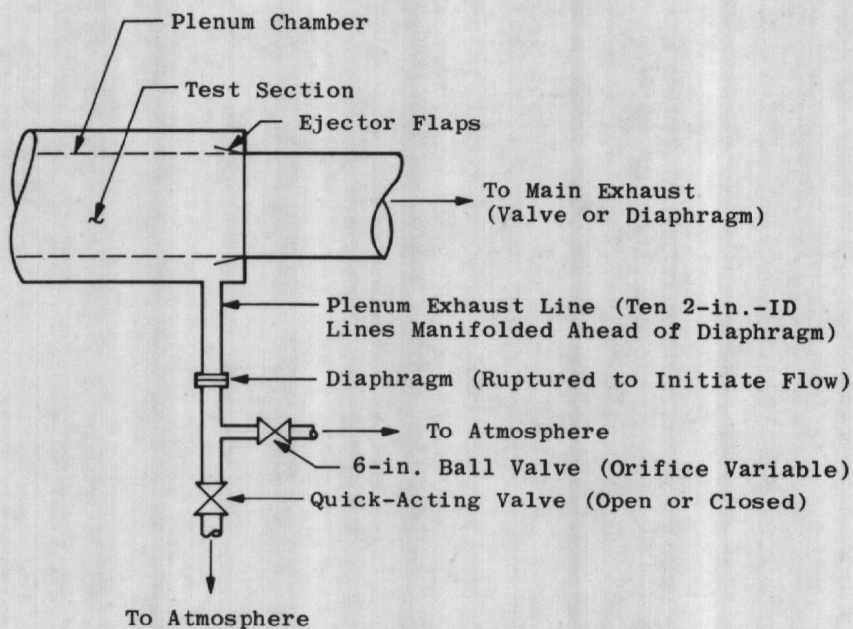


Figure 2.4. Plenum exhaust system.

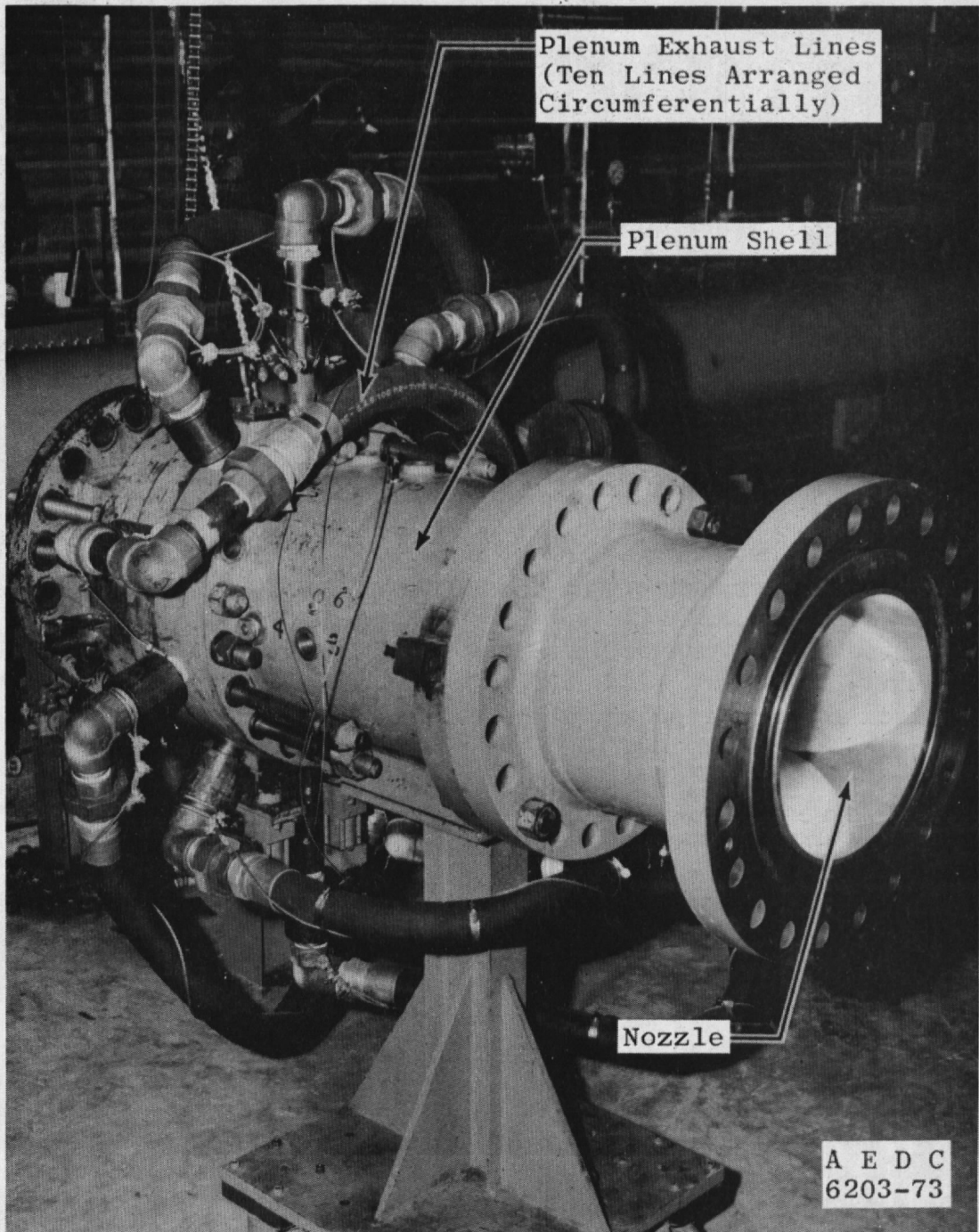


Figure 2.5. Exterior view of Pilot HIRT plenum shell and nozzle.

3.0 NOZZLE DESIGN AND PRESSURE DISTRIBUTIONS

The sonic nozzle for the Pilot HIRT facility is designed to provide a transition from the circular supply tube to the rectangular cross section of the test section. The design philosophy employed in determining the nozzle contours is discussed in Ref 5. The nozzle to be discussed here is a 0.0765-scale version of a 19-ft-long nozzle for a typical full-scale HIRT facility. Theoretical Mach number (Ref. 5) distributions for the Pilot HIRT nozzle are shown in Fig. 3.1. Significant differences between the wall and centerline Mach numbers are indicated near the nozzle entrance and are indicative of finite length nozzles.

Direct experimental evaluation of this nozzle consisted of static pressure measurements at several axial stations. Both wall and centerline pressures were measured. The wall pressures were obtained using 0.064-in. -diam tubing fastened to the wall with epoxy, as shown in the installation photograph, Fig. 3.2. The location of the orifices may be seen on the photograph by marks on the nozzle walls. Care was taken to insure that the tubes were aerodynamically clean ahead of, and several diameters downstream of, the orifices. The centerline data were obtained using a 0.75-in. -diam centerline pipe which extended approximately 2 ft ahead of the nozzle into the charge tube (see Fig. 4.1).

The experimental results are presented in Fig. 3.3, in the form of the measured ratio of static to total pressure as a function of axial location. The calculated pressure distribution used for comparison was obtained from the Mach number distributions of Fig. 3.1. The bars shown with each symbol represent the scatter in the data over a series of five runs.

The agreement between theory and experiment is reasonably good. Two points should be noted. First, the predicted difference between wall pressure and centerline or axis pressure near the nozzle inlet is substantiated by the measurements. Second, the area of worst agreement between theory and experiment occurs in the vicinity of and just upstream of the position where the contour blocks first intersect to form a corner ($x \approx 7$ in., see Figs. 3.2 and 3.3). The gradual change from circular inlet to a rectangular area in the nozzle is not modeled properly by the axisymmetric theory; thus, significant differences exist between theory and experiment in this region for the axis pressure distribution. Moreover, a local flow separation could explain the high corner wall pressure when compared to the bottom and side wall measurements at position $x \approx 7$ in.

A new nozzle, approximately 27-percent longer than the present nozzle and designed to eliminate the difference between wall and axis Mach number near the entrance, was designed and fabricated for the Pilot Tunnel. Static pressure orifices were drilled in the contour blocks during fabrication. However, this nozzle had not yet been installed at the time Pilot Tunnel operations were terminated (December 1974).

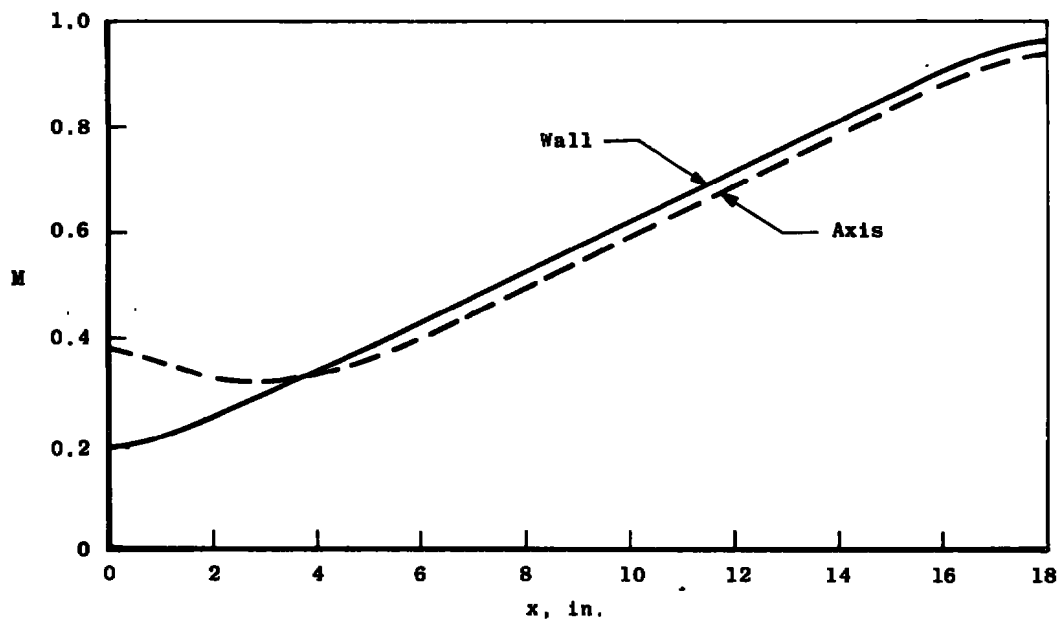


Figure 3.1. Theoretical Mach number distributions in Pilot HIRT nozzle.

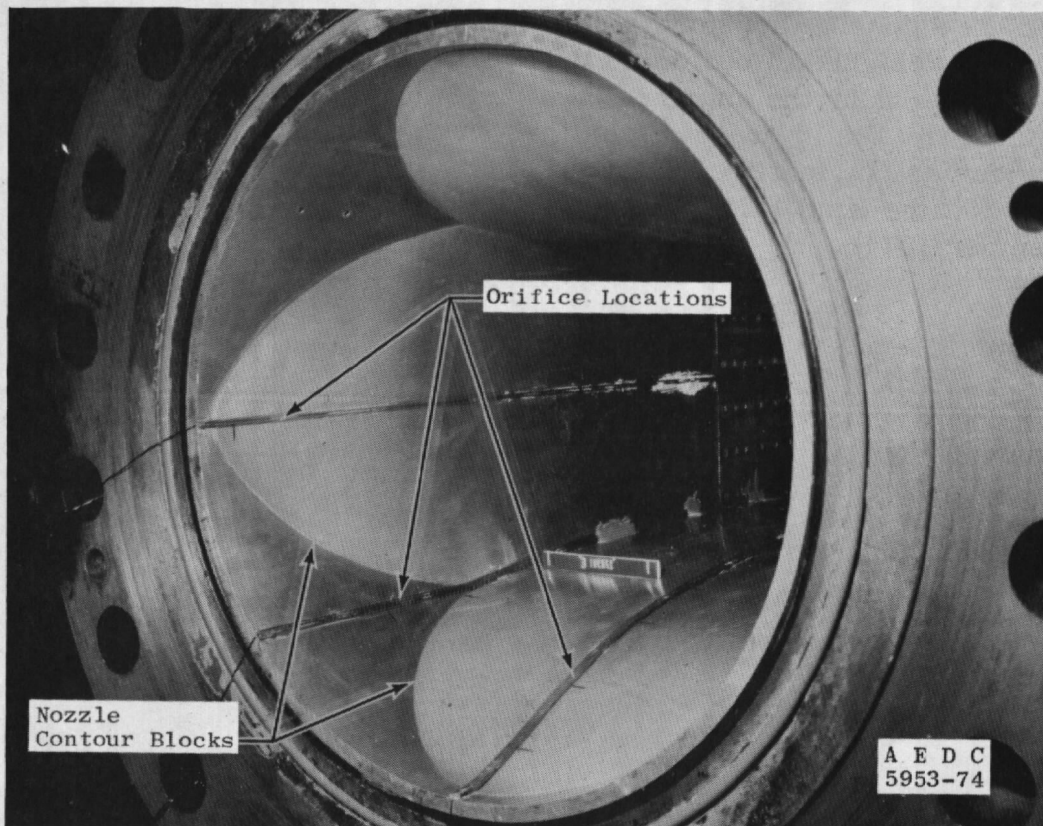


Figure 3.2. Nozzle static pressure tubing installation.

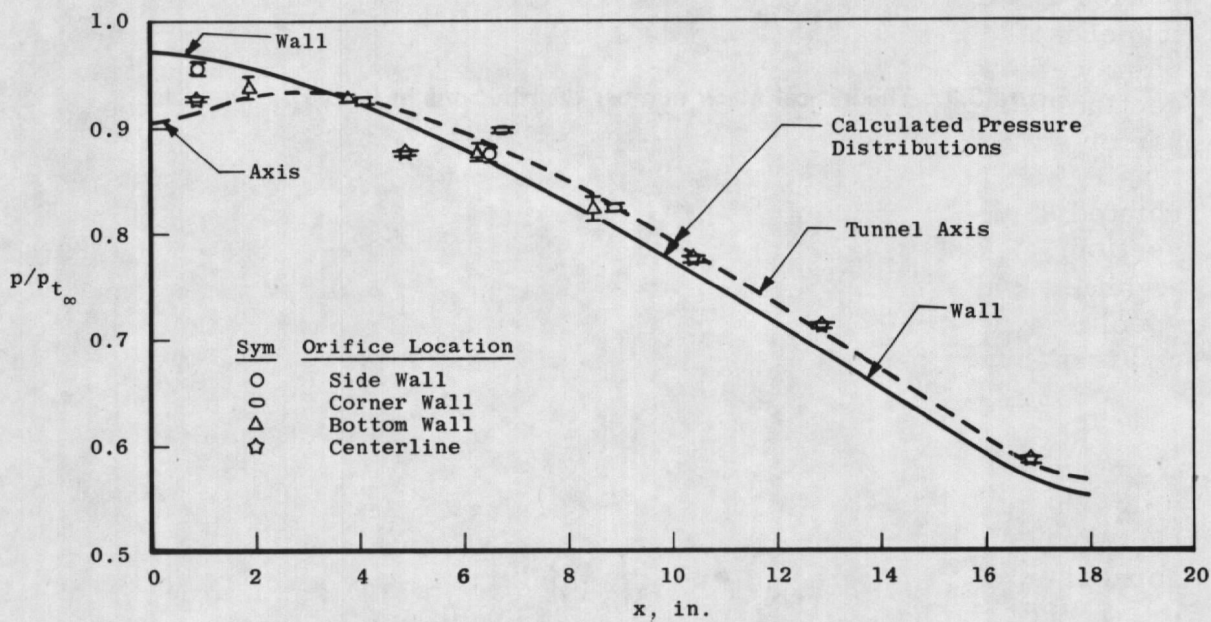


Figure 3.3. Nozzle static pressure measurements.

4.0 TEST SECTION AERODYNAMICS

The flow in the Pilot HIRT test section has been investigated on previous occasions by using a centerline pipe to obtain axial pressure distribution data. The Mach number distributions in the test section were shown to be similar to other comparable transonic tunnels, and calculations of the standard deviation as a function of free-stream Mach number in the test region gave 2σ values of 0.005 to 0.008 for Mach numbers up to 1.05, increasing to 0.015 at 1.2 Mach number, Ref. 4. The difference between the average Mach number in the test region and plenum chamber Mach number was about 0.005 at $M_\infty = 1$ and about -0.005 at $M_\infty = 1.2$. All these early data were obtained prior to the installation of the ejector flaps and a new diffuser system.

After the installation of the new diffuser assembly, including ejector flaps, it was desired to repeat the centerline pipe tests to determine whether or not the flow in the test section had been significantly altered. For this purpose, a new pipe was fabricated, with about four times as many pressure taps as the pipe used in the previous tests.

The centerline pipe used to obtain the pressure measurements was 0.75 in. in diameter and contained 42 orifices arranged in a spiral pattern. Because of limitations in the number of channels in the present data system only 20 centerline pipe pressures were recorded. The orifice diameter was 0.045 in. An installation view of the pipe in the tunnel is shown in Fig. 4.1. As can be seen, the pipe extended from a point well upstream of the nozzle in the charge tube, through the test section to a support strut at the diffuser inlet. The mounting at the sector support strut was such that the pipe was under a fairly high tensile load. The arms on the upstream support yoke, which is shown rotated 90 deg for illustration purposes, had a diamond shaped cross section. The axial locations of four representative orifices are indicated. Significant bias errors introduced by particular data channels and/or specific pressure orifices were eliminated by interchanging data channels and translating the pipe along the centerline.

Samples of the test section Mach number distributions derived from the pressure measurements are shown in Fig. 4.2. The location of the 20 centerline pipe orifices used in this test are indicated. The center of model rotation is marked, as is the test region which is approximately 9 in. long. The Mach number determined from plenum

pressure measurements (located as shown in Fig. 4.1) is also indicated on the figure for comparison purposes. The dotted line through the data in the test region is the average value of the data in that region.

As mentioned previously, it was established that some orifice effect problems were present in the data. While it was not possible during the course of this test to obtain all the information necessary to completely account for these effects, an effort was made during the data analysis to at least partially correct the measurements. This correction is based on the assumption that the orifice effect is manifested as an error in the pressure coefficient. This is consistent with results from the AEDC-PWT tunnels (Ref. 6). Thus, a correction factor was obtained by assuming that for $M_\infty \approx 0.6$, each of the measured pressure values in the test region should be equal to the average of all the measurements. The adjustment required to attain this for each orifice, expressed as a fraction of the dynamic pressure, was used as a correction factor for that orifice, and was applied at all the other Mach number conditions, using the corresponding value of dynamic pressure. This technique was applied only to the data in the test region as given in Figs. 4.2, 4.3, and 4.4, and some improvement in the amount of scatter was noted.

The data of Fig. 4.2 indicate a uniform distribution at low Mach numbers, with a slight s-shaped variation developing at higher Mach numbers. This variation has been observed previously in Pilot HIRT data and also in the PWT tunnels, Ref. 6, and indicates an incorrect porosity setting for supersonic Mach numbers and/or overexpansion effects associated with the tapered porosity region. Figure 4.2 also shows the effect of flap opening on the test section Mach number distribution. In the test region, no significant effect is present for variations in flap opening from 0.2 to 0.4 in. Some differences in the Mach number distribution attributable to the flaps is evident, however, in the region over the ejector flaps. This is indicative of the sensitive nature of the flow process just upstream of the sector leading edge which plays a major role in determining the mean test section flow conditions for the present diffuser and main valve characteristics.

The standard deviation of the Mach number in the test region has been calculated for a series of more than 20 runs similar to those shown in Fig. 4.2. The results are presented in Fig. 4.3, where 2σ is given as a function of the average test region centerline Mach number. The scatter in the data is considerably less than in previous Pilot HIRT test (Ref. 4) due to the increased precision of the new data system. The general trends are in agreement with the earlier Pilot HIRT results

(Ref. 4) and with PWT data (Ref. 7), although the increase in 2σ at Mach numbers greater than one occurs more sharply.

The difference between the average test section Mach number and the plenum Mach number is shown in Fig. 4.4 for both early (120 msec) and late (165 msec) times into the run. In Fig. 4.4a this parameter is given as a function of charge pressure for Mach numbers in the range 0.9 to 1.1. The difference appears to be nearly invariant with charge pressure and time into the run for the pressure range covered in this test. The variation of this parameter with Mach number at a constant charge pressure of 100 psia is shown in Fig. 4.4b. A substantial increase is noted at Mach numbers greater than one for the late time points (165 msec). This parameter is nearly invariant, however, with Mach numbers for the early time points in the run. Also included in the figure for comparison purposes are PWT/4T mean curves at five- and six-percent porosity (Ref. 7). The apparent difference in effective porosity of the 4T wall as compared to the Pilot HIRT walls is due to the differences in cross flow resistances caused by differing wall and flow geometries. A detailed investigation of the change in effective porosity due to timewise boundary-layer growth on the wall is given in Ref. 8.

One of the anticipated benefits from the use of ejector flaps was the reduction or elimination of the variation of test section Mach number with wall porosity as has been the experience in PWT/4T. Although a systematic study of this area of test section aerodynamics was not carried out, examination of the data from test conducted subsequent to the installation of the flaps indicates that this goal was not achieved. There apparently still exists a measurable effect of wall porosity on test section Mach number in the Pilot HIRT. With regard to test section aerodynamics, the addition of ejector flaps to the Pilot HIRT diffuser system appears not to have had the desired effects on tunnel operation. This is probably attributable to the fact that structural considerations made it necessary to have the flaps only about one-third as long as is customary in other transonic tunnels, thereby greatly reducing their effectiveness and apparent accommodation to other test section variations. A complete examination of the effects of the ejector flaps and new diffuser on the test section aerodynamics was not completed prior to the time tunnel operations were terminated.

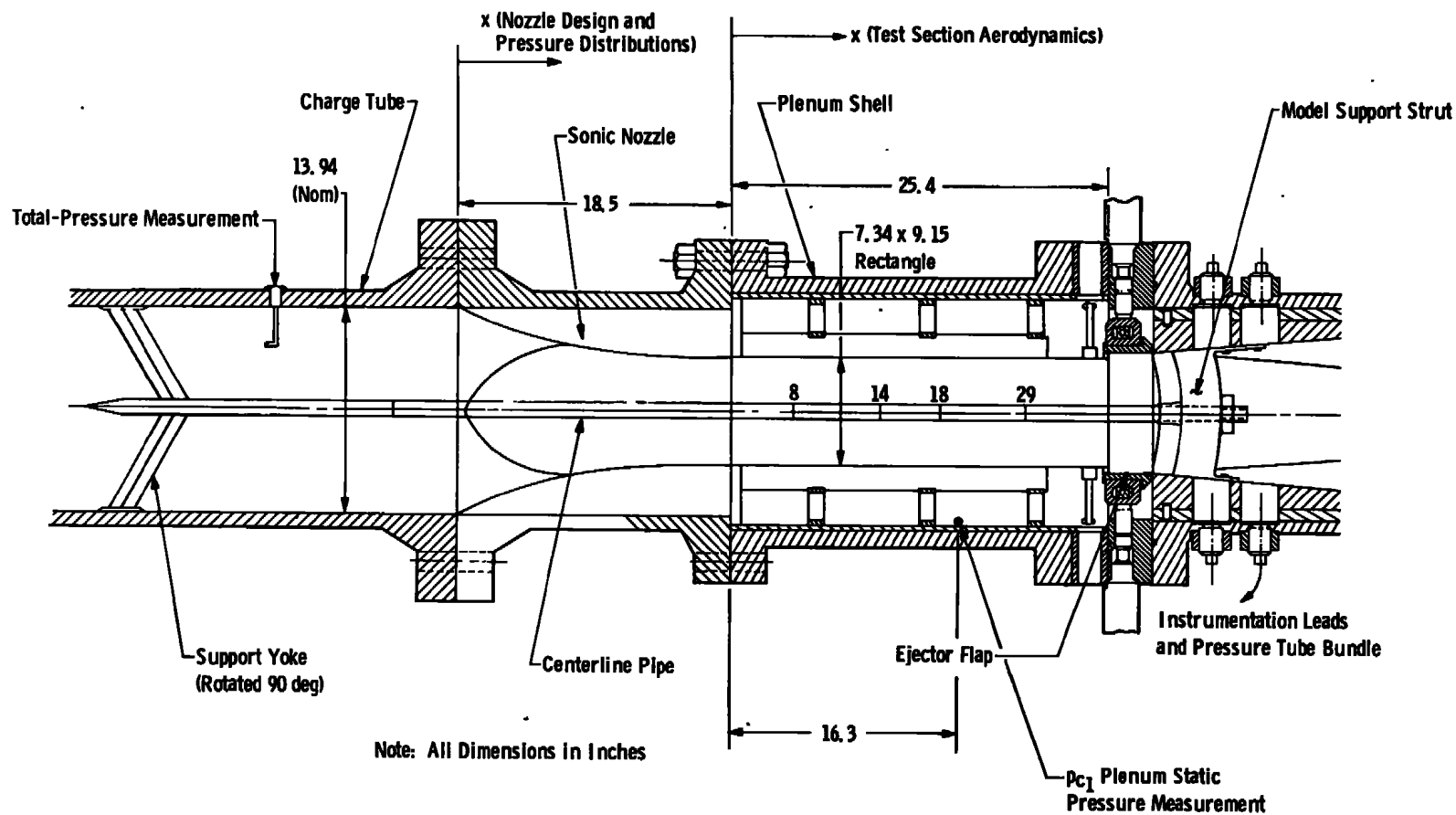


Figure 4.1. Centerline pipe installation.

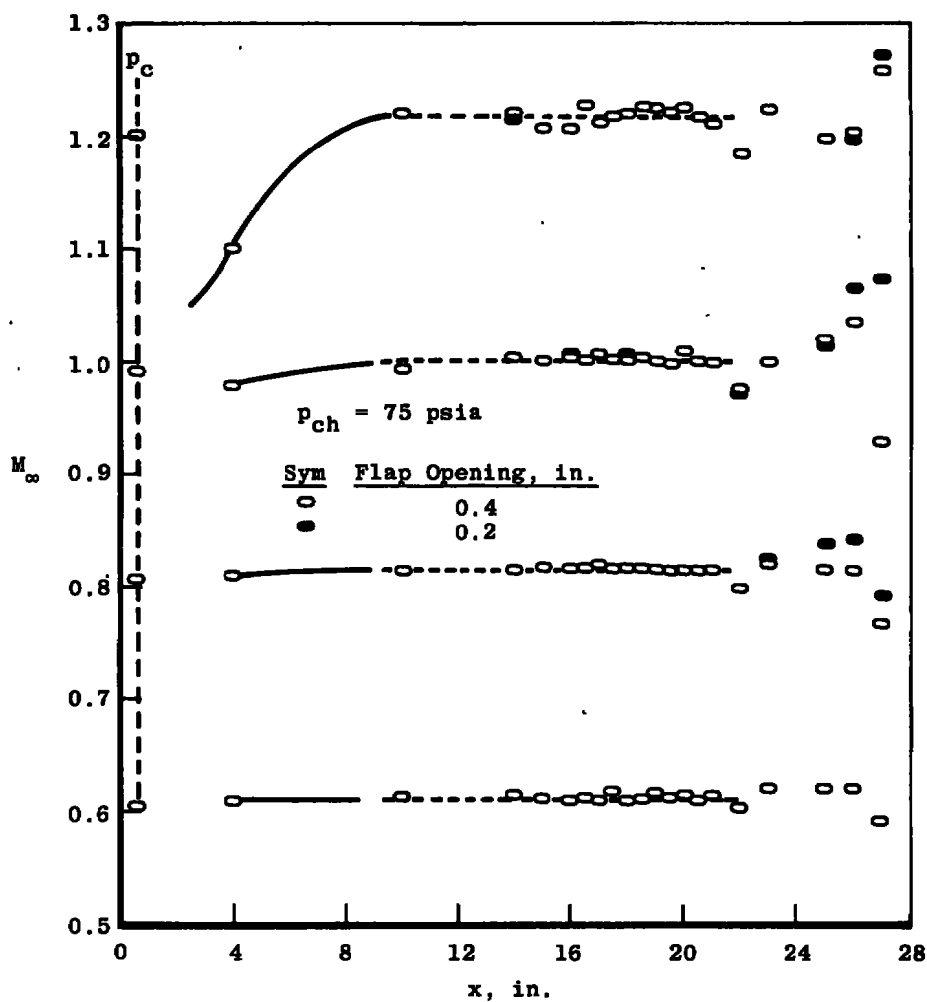
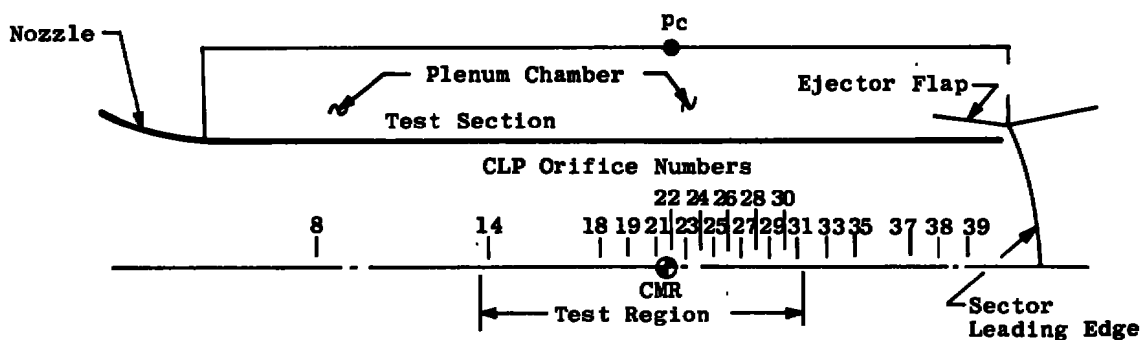


Figure 4.2. Test section Mach number distributions — 165 msec at a wall porosity of 4.5 percent.

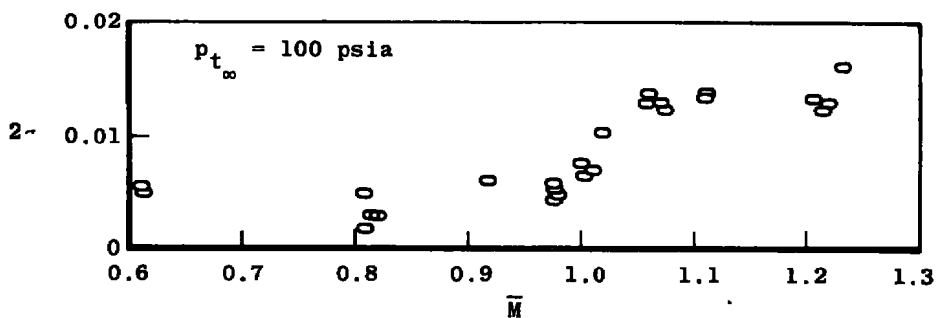
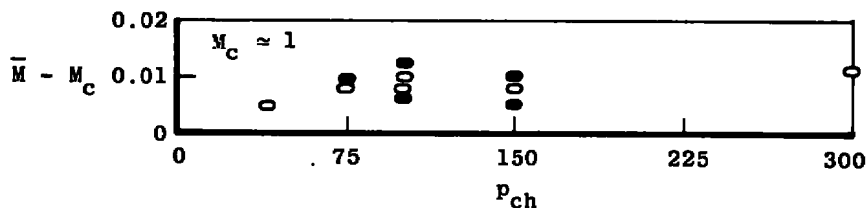
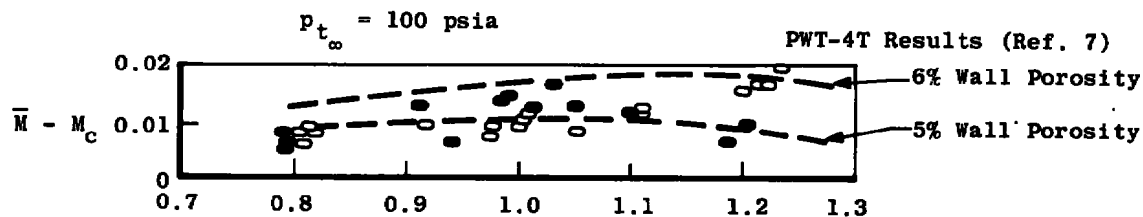


Figure 4.3. Standard deviation for data in the test region at a wall porosity of 4.5 percent.



a. Variation with charge pressure

- 180 msec into the Run
- 120 msec into the Run (Extremes)



b. Variation with Mach number

Figure 4.4. Plenum — test section Mach number relationships at a wall porosity of 4.5 percent.

5.0 PLENUM VOLUME AND THE AUXILIARY FLOW SYSTEM

A principal area of concern in the earliest Ludwig tube studies at AEDC involved the starting process and starting time of this type transonic facility. Analog studies indicated that the start time could be reduced by incorporating three "quick start" techniques into the facility design (Refs. 3 and 4) as follows: (1) a plenum exhaust which can be opened independently from the main tunnel exhaust, (2) a controllable plenum exhaust system which can provide an excess plenum exhaust during the starting process, and (3) a flap system in the tunnel wall which can be opened to provide increased plenum flow area during the tunnel start. Early in the experimental program, it became obvious that some of the assumptions in the analog program were oversimplified. In the absence of a more exact mathematical model, experimental observations to determine the interplay of the governing parameters were made. The importance of the starting time in a transonic facility which runs for only a few seconds cannot be overemphasized when data of ± 0.25 -percent uncertainty are required. The thrust of all of the HIRT effort in this regard has been to provide a start time short enough to allow data productivity in excess of one model attitude position per run. The experimental data which will be presented are intended to supplement, confirm, and expand earlier observations on this aspect of facility operation (Refs. 3 and 4), especially since the addition of ejector flaps and a modified diffuser system to the pilot facility.

5.1 PLENUM VOLUME

A series of experiments was conducted in the pilot tunnel for a range of plenum volumes. The ratio of the volume of the plenum system to the volume of the test section was 1.75 (small), 2.8 (medium), and 4.0 (large) in this study. The results are best illustrated by the timewise variation in plenum pressure given in Fig. 5.1. Note that the time constant, or start time of the system, increases almost proportionately with the plenum volume. The start time is defined as the time required for the plenum static pressure to become invariant within ± 0.25 percent. These runs were made at about Mach 1.0 and utilized the diaphragm main starting device to insure that the main valve opening time did not obscure or override the plenum volume effect. The ejector flaps were also open to a normal run setting of $\delta_f = 0.4$ in. and obviously contributed to the flow out of the plenum chamber in addition to the flow through the porous walls. Runs were also made with extra auxiliary flow in the starting process for the medium volume case and it should be noted that the time constant

(proportional to the start time) is reduced markedly (Fig. 5.1). This aspect of the starting phenomena will be discussed in more detail in a subsequent section.

A summary plot of the start time for the range of plenum volume ratios tested is given in Fig. 5.2 for runs with and without extra auxiliary flow during the starting process. An increased main valve opening time would shift the intersection of the curves with the ordinate upward and would decrease the slope with V_p/V_{ts} . The start times given here can be scaled directly with a linear test section dimension to obtain estimates for a larger facility if the tunnel geometry is similar. For instance, a tunnel ten times the size of Pilot HIRT would be expected to start in ten times the start time given in Fig. 5.2.

5.2 AUXILIARY FLOW DURING THE STARTING PROCESS

Previous experimental work with the HIRT pilot tunnel has clearly demonstrated the advantage of an excess auxiliary flow rate during the starting process if rapid start times are desired (Ref. 4). The excess flow areas associated with this auxiliary flow rate can be quantified based on more recent experiments.

The variation of the auxiliary flow area, A_A , during the starting process and run in Pilot HIRT is given in Fig. 5.3. On any run on which the plenum exhaust diaphragm is opened, the effective flow area is large during the start and approaches a steady-state value which is dependent on the ball valve setting (see Fig. 2.4). The solid curves denote a small and moderate ball valve opening. The magnitude of this steady-state auxiliary flow area, which produces the higher transonic Mach numbers, will be discussed in the next section. The duration of the large starting flow area can be extended as illustrated by the dashed curve in Fig. 5.3 by changing the time at which the closure of the quick acting valve (see Fig. 2.4) is initiated. For any given steady-state flow area, the flow area above that value is termed the excess auxiliary flow area, A_{AE} , and is represented by the cross-hatched region in Fig. 5.3. The flow areas as discussed here are effective or equivalent choked flow areas. Any other variations in the timewise character of the auxiliary flow area in Pilot HIRT are not possible with the present hardware.

Within the constraints of this auxiliary flow area curve, some observations of the excess auxiliary flow area required to achieve reduced start times can be made. Figure 5.4 gives the variation of the excess auxiliary flow area ratio, A_{AE}/A_{ts} , with start time. One band is for a triangular-shaped excess area curve as in Fig. 5.3. The other band is for a

rectangular-shaped excess area curve of the same integrated area (or the average of the triangular-shaped curve over the time interval 0 to t shown in Fig. 5.3). Obviously there is a factor of two difference in the number or size of auxiliary flow valves, dependent on which of these shapes is actually required. As was already shown in Fig. 5.1, Fig. 5.4 shows that the reduction in the start time is dramatic with the judicious application of excess flow area during the tunnel starting process. The data in Fig. 5.4 are for a specific plenum volume ratio of 2.5 and the bands represent the observed spread in data for $0.8 < M_\infty < 1.2$ and $0 \leq \delta_f \leq 0.4$ in. It appears that for a plenum volume ratio of 1.8, the required excess auxiliary flow area would be about 70 percent of that shown in Fig. 5.4 for a fixed start time (see Fig. 5.1). In making predictions of the excess auxiliary flow area which is actually required to minimize the start time, an average of the triangular and rectangular shapes (trapezoidal) will be assumed.

5.3 A MODEL FOR MINIMUM START TIME

As noted in the preceding section, many parameters affect the tunnel start time. In designing a typical HIRT facility, an optimization of the parameters would be required to achieve the best compromise of plenum volume and excess auxiliary mass flow in order to minimize the start time. In this section a simple model will be formulated that predicts the interrelationship of excess auxiliary flow, plenum volume, and anticipated test section Mach number as influenced by the opening characteristics of the main valve starting device.

Let us first assume that the transient process in the test section interacts strongly with the waves generated by the opening of the main valve as modified in the diffuser. Thus, we require that the ratio of the characteristic valve opening time, τ_v (to be defined in Section 6.3), to the characteristic response time of the test section, L/a_∞ , where L is the test section length, is of order one. When $\tau_v a_\infty / L$ is large, the main valve opening characteristic dominates the starting process and will be discussed in a subsequent portion of this section. Therefore, it will be assumed that the strong wave interaction resulting when $\tau_v a_\infty / L$ is of order one may be approximated by an exponential process. Hence, the transient static pressure in the test section may be described by Eq. (5.1) (to be developed in Section 6.3)

$$\frac{p}{p_{ch}} = \mu + (1 - \mu) e^{-t/\tau_v} \quad (5.1)$$

where

$$\mu = p_\infty / p_{ch}$$

In order to achieve the minimum starting time for a particular flow configuration, the plenum volume must be discharged in such a way that no flow perturbations are introduced into the transient test section flow process. This condition will assure an optimum auxiliary mass flow, plenum volume relationship for a given start time, t_s . Here, t_s is defined as the time required for the test section static pressure to approach the steady-state value within 0.25 percent. Thus, Eq. (5.2) may be derived (refer to Section 6.3) which gives the proper choked excess flow area as a function of the plenum pressure for minimum start times.

$$\frac{d}{dt} P_i + 0.0165 \frac{RT^{1/2}}{V_p} A_{AE} P_i = 0 \quad (5.2)$$

Here, R is the gas constant, T is the tunnel charge temperature, V_p is the plenum volume, and A_{AE} is the required excess auxiliary flow area. Solving Eq. (5.2) with Eq. (5.1) and defining the excess auxiliary flow area ratio, A_{AE}/A_{ts} , and the plenum volume ratio, V_p/V_{ts} , the timewise variation of A_{AE}/A_{ts} may be evaluated and is given in Eq. (5.3).

$$\frac{A_{AE}}{A_{ts}} \frac{V_{ts}}{V_p} \frac{r_{v\infty}}{L} = 1.73 \left[1 + \frac{\mu}{1-\mu} e^{t/\tau_v} \right]^{-1} \quad (5.3)$$

This relationship is plotted in Fig. 5.5 and shows that as the value of μ decreases, corresponding to an increase in the steady-state Mach number, M_∞ , the required excess flow area, A_{AE} , increases in order to maintain the minimum start time. The minimum start time as a function of the characteristic valve time and μ may be derived from Eq. (5.1) and the definition of t_s as given previously and is shown in Fig. 5.6. Hence, once a characteristic valve time, τ_v , and operating pressure ratio, μ , are defined, the minimum start time, t_s , is found from Fig. 5.6 with the excess auxiliary flow area required to attain the minimum start time illustrated in Fig. 5.5 for the transient test section static pressure variation as given in Eq. (5.1).

In Section 5.2 an average excess auxiliary flow area was defined and employed in the presentation in Fig. 5.4 of the Pilot HIRT data. Minimum start times were then established based on this average quantity. An average excess auxiliary flow area, \bar{A}_{AE} , for the minimum start time model may be evaluated through the use of Eqs. (5.3) and (5.4).

$$\int_0^{t_s/\tau_v} A_{AE} dt/\tau_v = \frac{t_s}{\tau_v} \bar{A}_{AE} \quad (5.4)$$

which leads to

$$\frac{\bar{A}_{AE}}{A_{ts}} \frac{V_{ts}}{V_p} \frac{a_\infty t_s}{L} = 1.73 \ln \frac{1}{\mu} \quad (5.5)$$

Figure 5.7 is a plot of the excess auxiliary flow area ratio, \bar{A}_{AE}/A_{ts} , as a function of the nondimensional start time, $a_\infty t_s/L$, for a plenum volume ratio $V_p/V_{ts} = 2.5$ for various values of the pressure ratio, μ ; also included is the data band for Pilot HIRT as given in Fig. 5.4. The Pilot HIRT data is equivalent to $\mu = 0.3$ for values of $a_\infty t_s/L$ near 25 and approaches $\mu = 0.4$ as $a_\infty t_s/L$ increases. Thus, the start time model apparently predicts accurate values of the ratio \bar{A}_{AE}/A_{ts} when compared to the Pilot HIRT results (Fig. 5.4). For values of $a_\infty t_s/L$ less than approximately 70, \bar{A}_{AE}/A_{ts} is inversely related to $a_\infty t_s/L$. As $a_\infty t_s/L$ increases beyond 70, the requirement that $\tau_v a_\infty/L$ be of order one is no longer satisfied and, as a result, Eq. (5.1) is no longer valid. The minimum start time, therefore, may no longer be determined from Fig. 5.6, and, moreover, should approach the valve time, τ_v , as the value of $\tau_v a_\infty/L$ grows without bound. For this situation, Eq. (5.5) is still valid, however. If Eq. (5.1) is replaced by a linear relation between p/p_{ch} and t/τ_v (which approximates the case for $\tau_v a_\infty/L$ large), then the start time becomes exactly τ_v and the average excess flow area \bar{A}_{AE} is expressed, once again, by Eq. (5.5). Thus, Eq. (5.5) is valid for all values of $\tau_v a_\infty/L$ and, therefore, can be used to determine the average excess flow area required to obtain a desired start time for a given plenum and test section configuration.

Figure 5.8 is a plot of the plenum volume ratio versus the nondimensional start time for fixed average excess flow area and shows the linear relationship between the two variables. A comparison of the Pilot HIRT data as given in Fig. 5.2 with Fig. 5.8 indicates validity in this linear representation and further confirms the correctness of Eq. (5.5) in defining the average excess auxiliary area ratio required to obtain the minimum start time for a given main valve system.

5.4 STEADY-STATE AUXILIARY FLOW

The steady-state auxiliary flow rate ratio, $\dot{w}_{AS}/\dot{w}_{TOT}$, required to achieve the higher transonic Mach numbers in the pilot tunnel is given in Fig. 5.9a for several diffuser ejector flap openings. It can be seen that the subsonic performance of the tunnel is enhanced by relatively small ejector flap openings. However, the rather steep rise of auxiliary flow rate with Mach number for the ejector flaps open, compared to the simplified theory denoted by the dashed curve, indicates that the ejector action deteriorates rapidly with increased Mach number. This is not surprising when one considers the Mach number distribution at the back of the test section (Section 4), the relatively short flaps (small area expansion), and the close proximity of the model support strut to the flap hinge line. Alternate design considerations would then be (1) increase flap length to minimize the deterioration in ejector action at the penalty of increased flap loads, (2) location of the sector further aft which results in unacceptable sector moments and sting distortion, or (3) the provision of extra auxiliary flow to make up for the deteriorated flap action at the higher Mach numbers. The latter alternative appears to be the most palatable. The flow rate ratio is expressed in terms of flow area in Fig. 5.9b for the range of ejector flap openings.

The total auxiliary flow area, which is a summation of the excess auxiliary area (Fig. 5.4) and the steady-state auxiliary area (Fig. 5.9), is given in Fig. 5.10 for the transonic Mach number range. These curves are valid for $V_p/V_{ts} = 2.5$ and ejector flaps open, $\delta_f/H \approx 0.05$. For a pilot tunnel start time of about 50 msec, an effective auxiliary flow area of about 30 percent of the test section cross-sectional area is required at Mach 1.2. Similarly, a tunnel ten times the size of the pilot tunnel could be started in 0.5 sec at Mach 1.2 with $A_A/A_{ts} = 0.3$ for the same plenum volume ratio and flap height ratio.

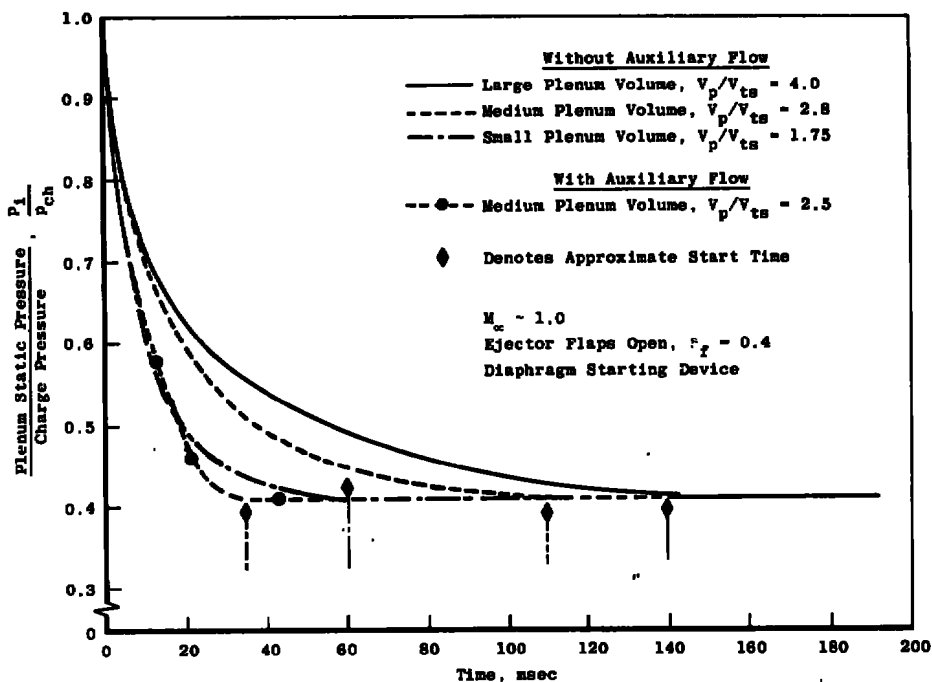


Figure 5.1. Plenum static pressure time history showing the effect of auxiliary flow on tunnel start time.

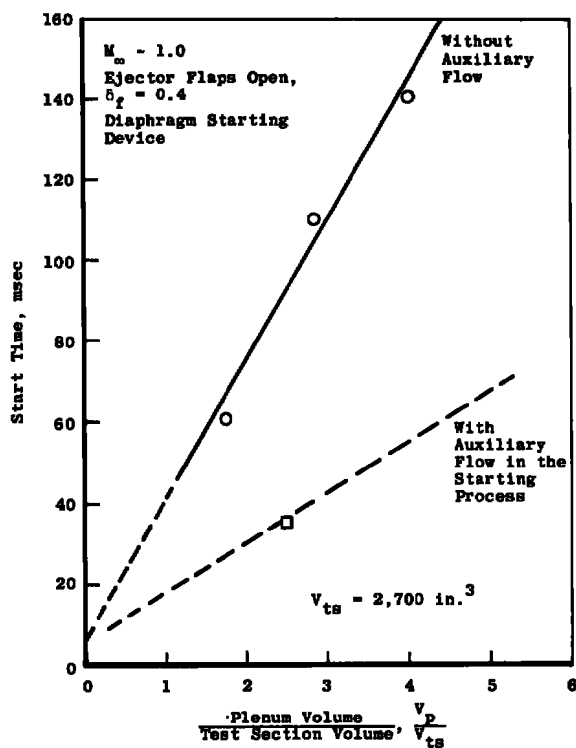


Figure 5.2. Minimum start time as a function of plenum volume with and without auxiliary flow.

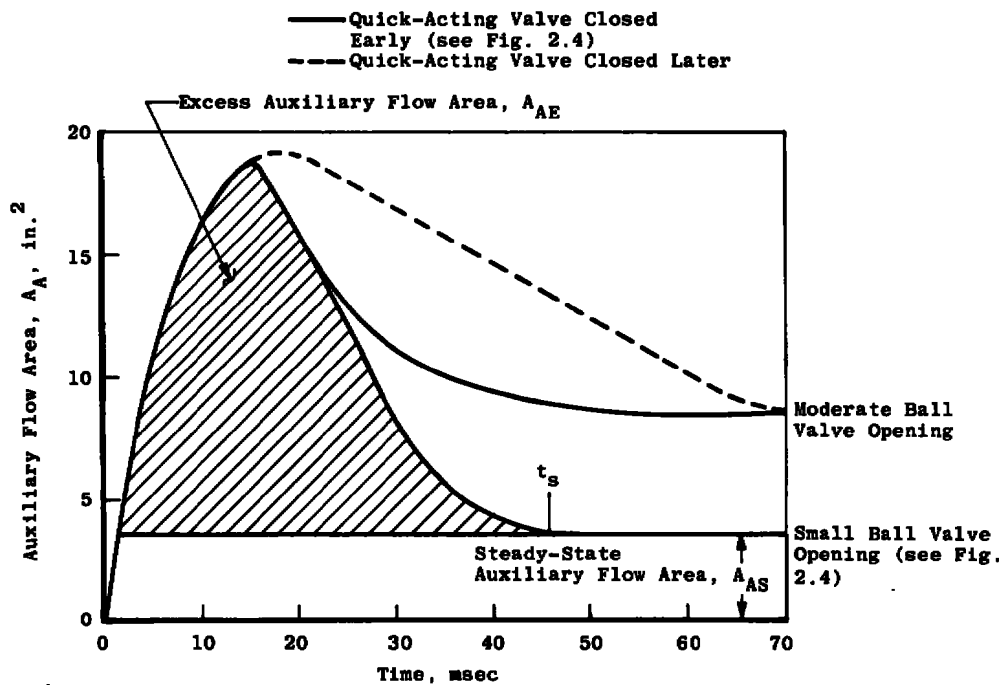


Figure 5.3. Auxiliary flow area time history during the starting process in Pilot HIRT.

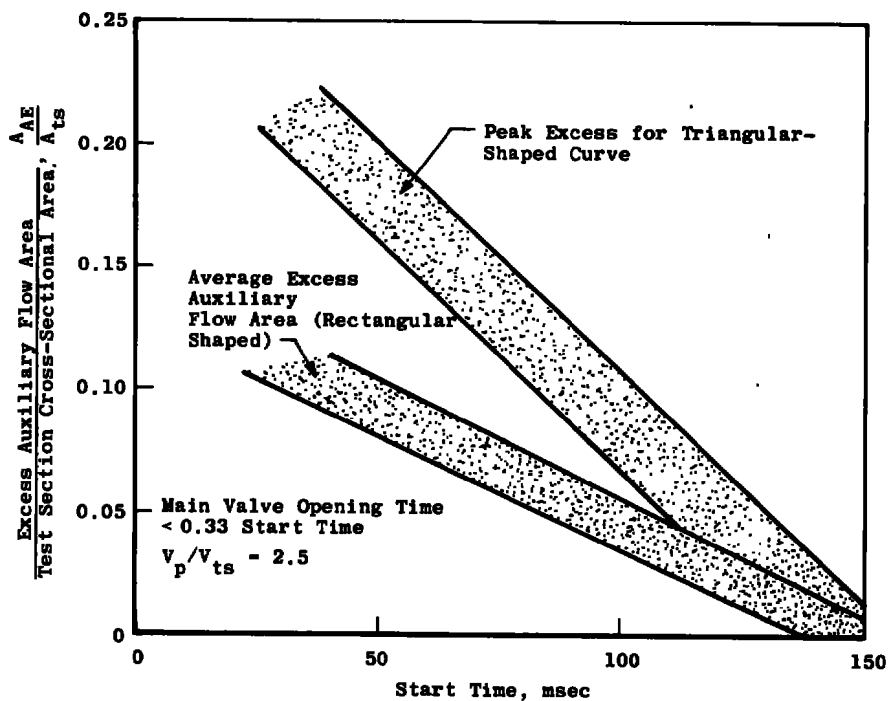


Figure 5.4. Excess auxiliary flow area required to achieve minimum start time.

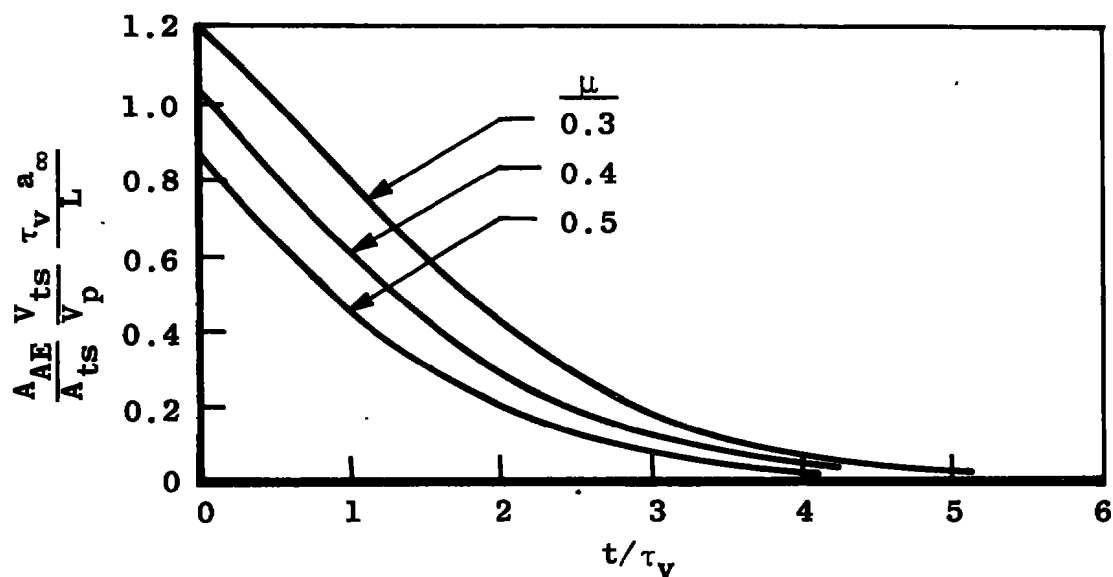


Figure 5.5. Excess auxiliary flow area as a function of time required to minimize start time, theoretical.

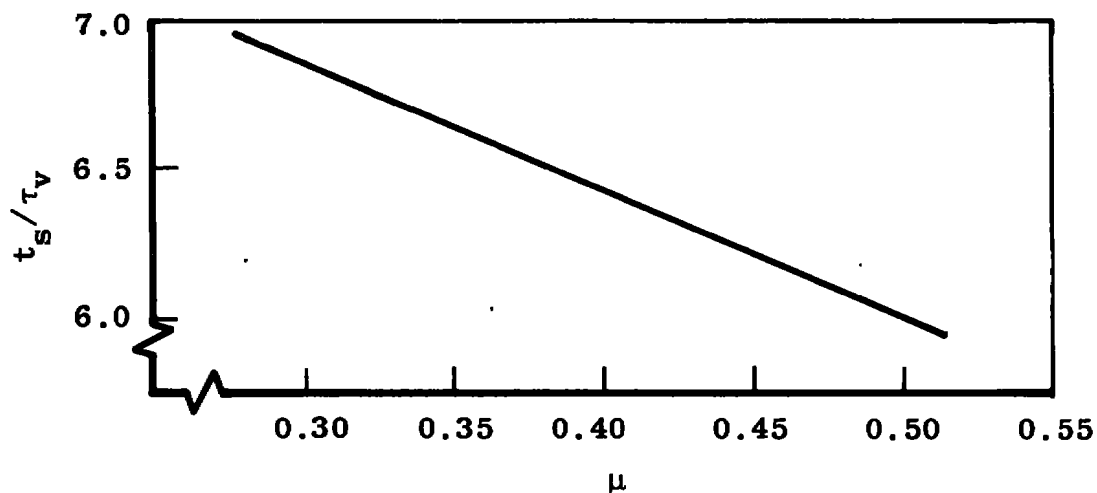


Figure 5.6. Minimum start time as a function of the pressure ratio, μ , theoretical.

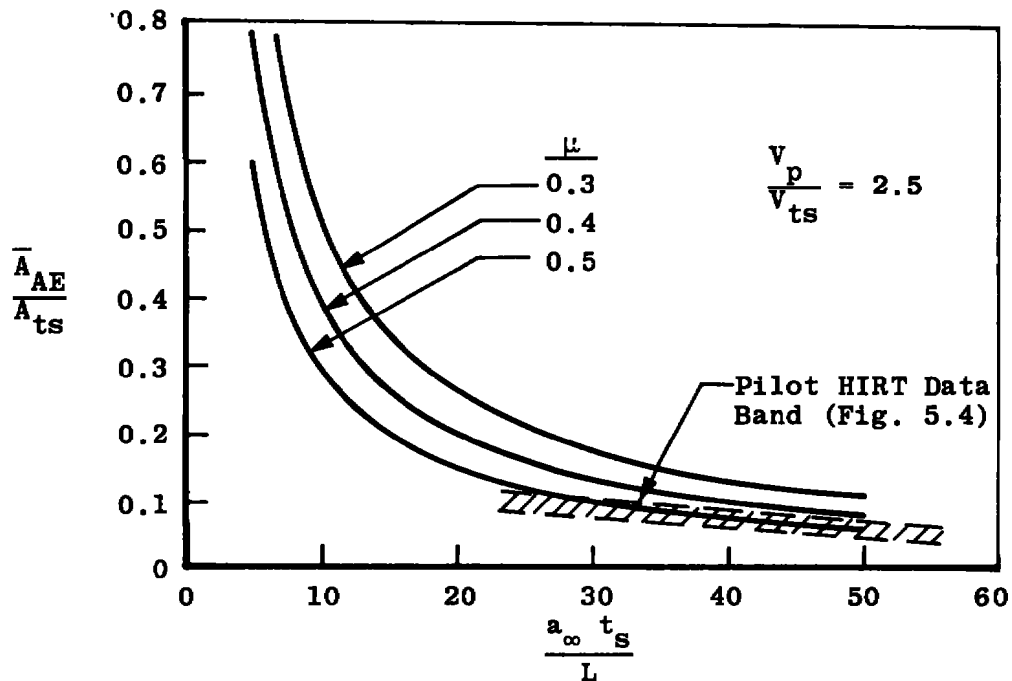


Figure 5.7. Average excess flow area ratio as a function of the nondimensional start time for a fixed plenum volume ratio, theoretical.

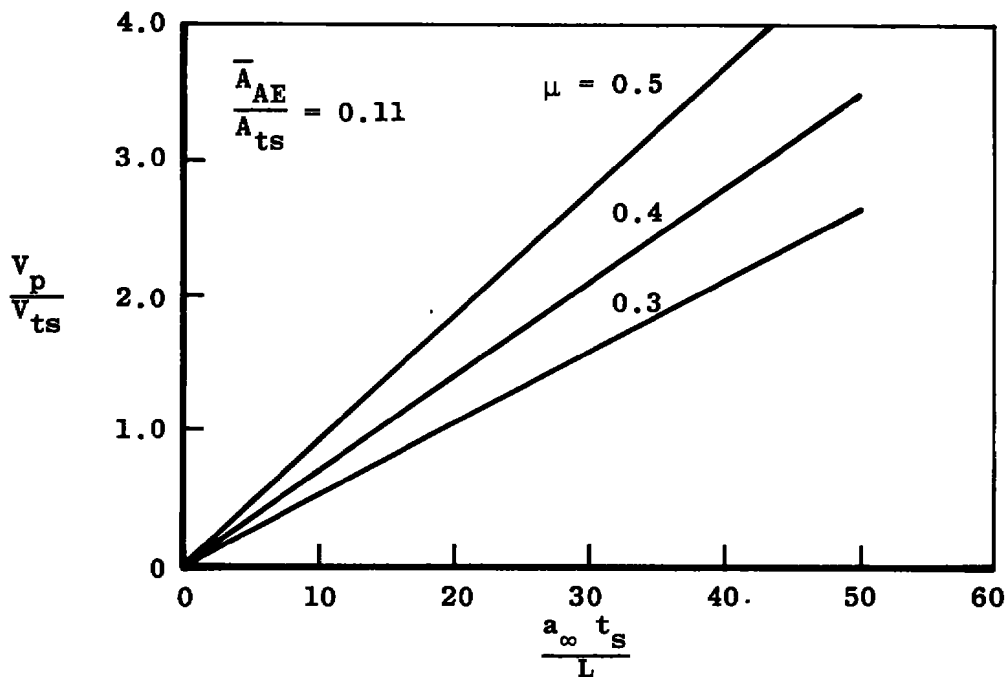
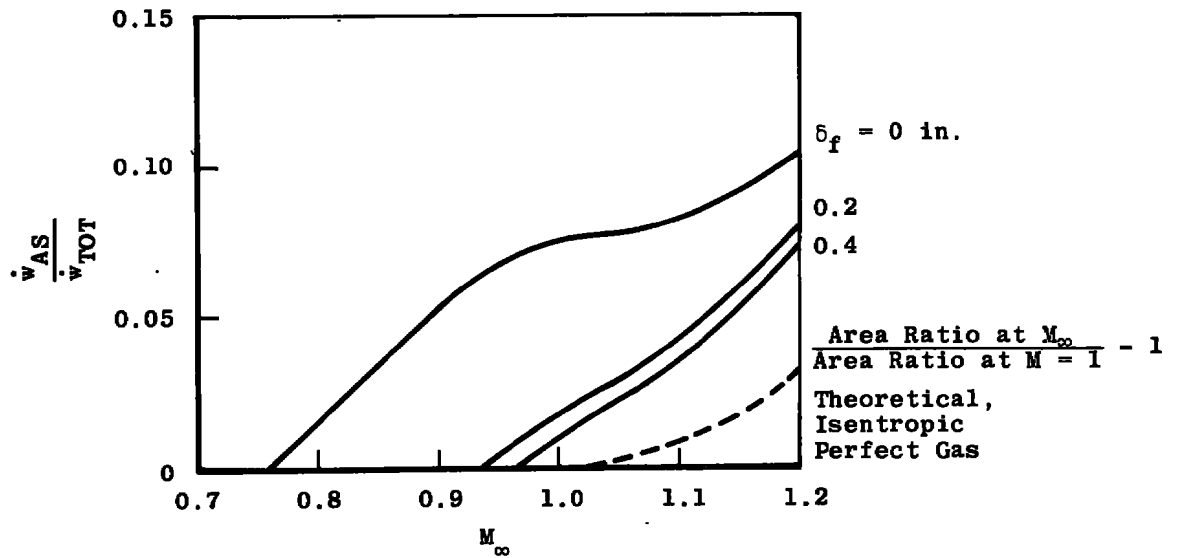
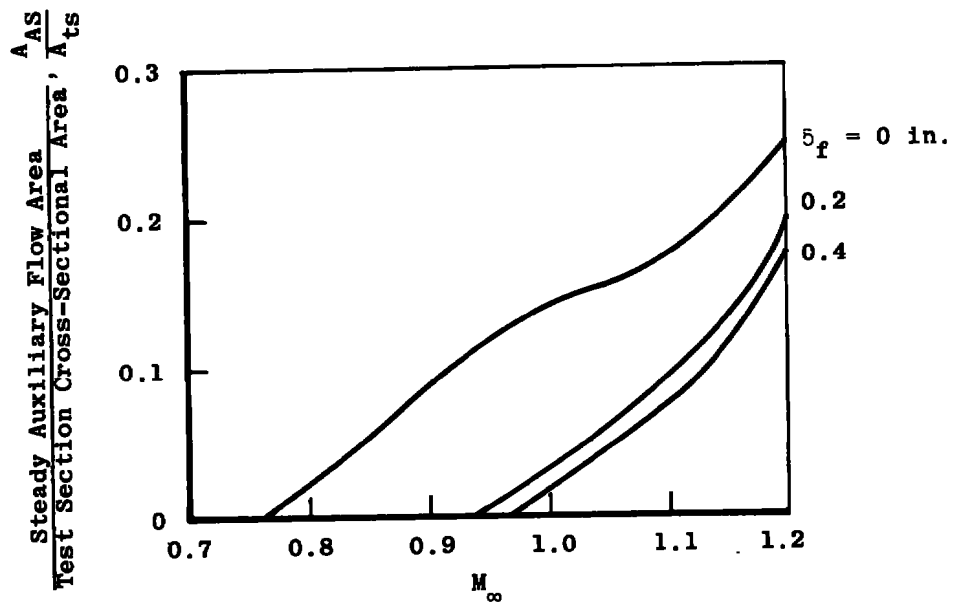


Figure 5.8. Plenum volume ratio as a function of the nondimensional start time for a given average excess flow area ratio, theoretical.



a. Steady-state flow rate ratio for a range of Mach numbers



b. Steady-state auxiliary area ratio for a range of Mach numbers
Figure 5.9. Steady-state auxiliary flow requirements in Pilot HIRT.

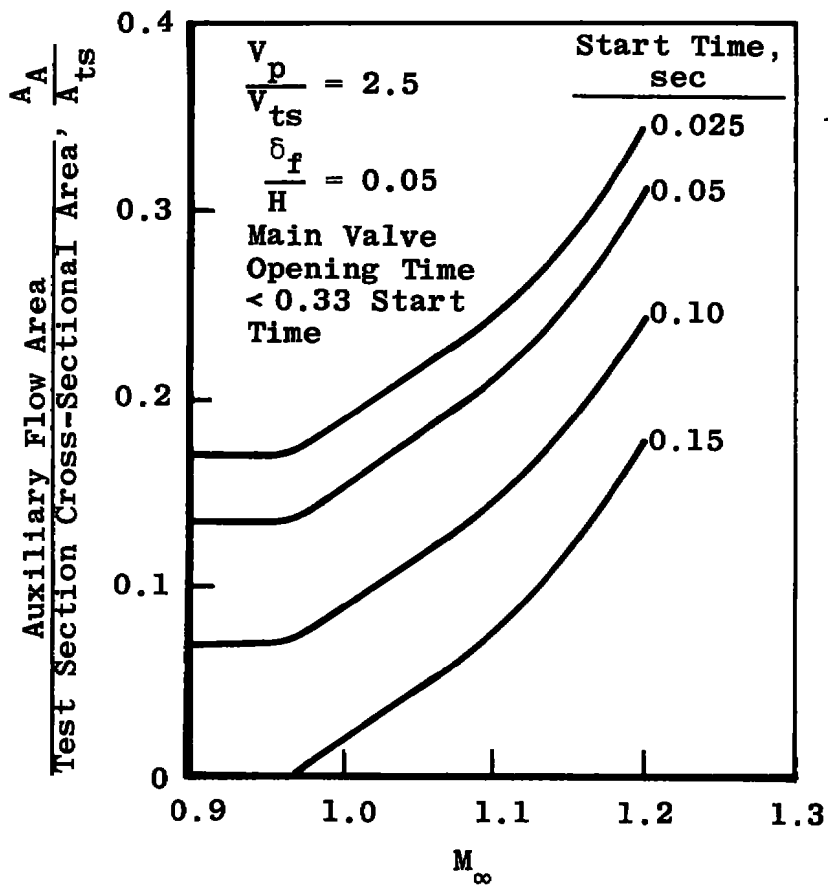


Figure 5.10. Total auxiliary flow requirements required to attain a specified Mach number and start time in Pilot HIRT.

6.0 TEST SECTION WALL AND FLAP AERODYNAMIC LOADS

During the starting process in Pilot HIRT, the test section walls and ejector flaps are subjected to a differential pressure attributable to the inability of the plenum chamber pressure to follow the test section static pressure gradient with time and position. Because of the transient nature of a HIRT-type facility, rapid starting process is required in order to assure the highest possible productivity. It was anticipated that test section wall loads and ejector flap loads would be influenced by the starting process and by other geometric and aerodynamic flow constraints. Thus, in order that the best possible design criteria be established for the loads on the test section walls and on the ejector flaps of a full-scale HIRT facility, an extensive experimental parametric study was undertaken in the Pilot HIRT. To aid in the interpretation of the data and extrapolation of the results to a larger scale facility, the flow process was modeled using experimentally obtained flow coefficients. With the evaluation of the wall loading for the pilot facility, design criteria for a full scale HIRT-type facility has been established.

6.1 EXPERIMENTAL PROCEDURE

In order to measure the differential pressure distribution during the tunnel starting process, fast response transducers of relatively high sensitivity were required. To satisfy these requirements, variable reluctance differential transducers with a response time on the order of 1 msec were used for a majority of the differential pressure measurements on the test section walls. Five gages placed along the top porous wall as shown in Fig. 6.1 gave time-varying output during a run which was recorded on a high-speed oscillograph. These gages were located close to the middle of the transverse plane of the porous plate as illustrated in Figs. 6.1 and 6.2. Each gage was mounted such that it responded to differential static pressure changes across the test section wall. In addition, one differential pressure transducer was mounted at the rear of the test section on a short section of the wall as shown in Fig. 6.2. The ejector flaps were instrumented with four 100-psi strain-gage differential transducers with response times on the order of 1 msec. Three gave the differential between static pressure on the flow side of the ejector flap and the local plenum pressure, and the fourth measured the streamwise pressure gradient along the flap. All four flap gages were installed on one side flap, and all test section wall differential gages were located on the top porous plate. Figures 6.2 and 6.3 illustrate the axial location of the differential pressure gages on the ejector flap.

It was assumed that the wall and flap loads would be a function of the time required to start the tunnel, the degree of mass removal from the plenum by auxiliary or ejector flap pumping during the starting process, the porosity of the test section wall, the volume of the plenum cavity, the tunnel charge pressure, and the streamwise development of the unsteady test section and diffuser flow. In order to evaluate the effects of tunnel start time, the opening time of the main valve system was varied by using a 16-in. -ID sliding sleeve valve (SSV) having an opening time ($\Delta\tau_v$) of 40 to 80 msec depending upon the number of ports opened on the valve body, a 12-in. -ID SSV with an opening time of 25 msec and a diaphragm device giving essentially an instantaneous opening time. The effect of variations in plenum pumping on the wall and flap loads was examined by independently changing flap settings and the quantity of auxiliary mass flow removed from the plenum chamber.

6.2 EXPERIMENTAL RESULTS, TEST SECTION WALL LOADING

During the starting process, the porous test section wall will be subjected to a differential pressure that is a function of axial location along the wall, a plenum response time, a characteristic valve time, and the rate of auxiliary mass flow removal. The plenum response time, τ_T , is a function, in particular, of the wall crossflow resistance, the flow resistance across the flaps, and the plenum chamber geometry. The characteristic valve time, τ_v , on the other hand, is a function of the actual time necessary to open the main valve system to obtain the desired test condition, the manner in which the valve is opened, and the spreading of the expansion wave as it travels to the rear of the test section through the diffuser system.

Figures 6.4 and 6.5 give the wall loading during the starting process as a function of porosity, τ_w , and charge pressure, p_{ch} , with stations as indicated in Fig. 6.2. Wall loading was also examined as a function of test section Mach number, M_∞ , by variation of the amount of excess and auxiliary plenum pumping. It was found that the condition of maximum Mach number with no excess or auxiliary pumping produced the most severe wall loading and, further, described the general time variation in pressure during the start for the desired Mach numbers from 0.75 to 1.2. Thus, results presented are for the conditions of maximum M_∞ with no excess or auxiliary pumping.

Figure 6.4 shows the effect of porosity on the wall starting loads. As the porosity is decreased, the differential pressures, as reflected in the differential pressure coefficient, $\Delta p/p_{ch}$ (equal to $(p_i - p)/p_{ch}$

where p_i , p , and p_{ch} are the local plenum chamber, test section static and charge pressures, respectively), increase proportionately. An extreme gradient between stations 4 and 5 (see Fig. 6.2) in the differential pressure also exists and is enhanced by increasing porosities. This effect is due to the gradient in the static pressure along the tunnel center-line during the starting process. According to Fig. 6.4, at station 5 (5.2 in. upstream of the rear of the test section) a maximum differential pressure coefficient of nine percent at 15 msec into the run is present with an increase to 13 percent at 18 msec into the run for a decrease in porosity from 4.5 percent to 2.25 percent, respectively.

Wall loading as a function of charge pressure is shown in Fig. 6.5 for charge pressures of 100, 150, and 200 psia. The results confirm expectations that the wall pressure differential is directly proportional to the tunnel charge pressure, p_{ch} . Since the experimental measurements given in Figs. 6.4 and 6.5 show that the extreme loading conditions on the walls during the starting process occur at the downstream end of the test section, the remainder of this section will concentrate on the load distribution over the rear one-third of the test section and will assume that loading scales with charge pressure.

Figure 6.6 presents some typical results of loading versus time for stations 4, 5, and 6 (see Fig. 6.2) using ejector flap pumping. The differential pressure, $\Delta p = p_i - p$, is given as a function of the flap open area, A_f , using the 16-in. sliding sleeve valve with a valve opening time, $\Delta \tau_v$, of 40 msec. As the flap opening is increased from 0 to $0.46 A_{ts}$, where A_{ts} is the test section cross sectional area, the differential pressure coefficient, $\Delta p/p_{ch}$, decreases at each of the stations. At station 6, steady-state values of the differential pressure were always much less than the corresponding peak loads. There also is an apparent shift in the time location of the peak load for each of the stations. Figure 6.7 shows the peak value of the differential pressure coefficient, $(\Delta p/p_{ch})_{max}$, plotted against test section length. Curves of constant A_f/A_{ts} , where A_f is the flap flow area, show a similar trend when compared to one another. Notice that as the flap area opens from 0 to $0.46 A_{ts}$, the maximum of $(\Delta p/p_{ch})_{max}$ decreases from 0.15 to 0.015, a factor of 10 in load. The peak value also occurs at the same axial location for all flap settings.

Following the study using the 16-in. SSV tunnel starting device, the effect of characteristic valve time on the maximum wall loading during the starting process was studied by incorporating a diaphragm device for the main valve. This gave, for all practical purposes, an instantaneous

opening time. Coupled with the approximate wave spreading effect due to the presence of the diffuser, a characteristic valve time of about 5.5 msec resulted for the diaphragm system. Thus, a variation in characteristic valve time by a factor of 8 was possible to show the effects of characteristic valve time on maximum wall loading. The trend of $(\Delta p/p_{ch})_{max}$ versus axial location for the diaphragm was similar to the corresponding results for the 16-in. SSV (Fig. 6.7). The magnitude, however, of $(\Delta p/p_{ch})_{max}$ locally and as a function of A_f/A_{ts} was considerably higher for the diaphragm cases as compared to the 16-in. valve case. $(\Delta p/p_{ch})_{max}$ versus axial location for the diaphragm case is given in Fig. 6.8. These results are as expected since the stronger expansion fan is generated by the faster valve action.

It was noted that wall porosity influenced the wall loading as depicted in Fig. 6.4. Figure 6.9 is a plot of $(\Delta p/p_{ch})_{max}$ using the diaphragm as the starting device illustrating the effects of wall porosity on the wall load distribution. This figure indicates that there is some change in the general shape of the 1.5-percent porosity curves when compared to the 4.5-percent porosity curves. Generally speaking, however, the load distribution trend appears to be maintained for variations in wall porosity. Moreover, Fig. 6.9 shows that as the flap opening, represented by the flap open area, A_f , is increased, the influence of wall porosity on the maximum of $(\Delta p/p_{ch})_{max}$ decreases. Thus, for $A_f/A_{ts} \gtrsim 0.1$, variations in τ_w are of second-order effect as compared to effects caused by diaphragm opening times on $(\Delta p/p_{ch})_{max}$.

6.3 WALL LOADING PROCESS MODEL

In order to model the wall loading process, some simplifying assumptions will be made. As the model is developed, the assumptions needed in the development will be stated and their effect on the actual process examined. The experimental data, as presented in Figs. 6.6 through 6.9, give all the information necessary to evaluate undetermined parameters. Thus, only data obtained using the 16-in. valve (41-msec characteristic valve time) will be used to fix empirical constants. Results for the diaphragm case (characteristic valve time of 5.5 msec) will then be used to indicate the accuracy of the model.

Figure 6.10 illustrates schematically the plenum discharge process. As the head of the expansion wave reaches the rear of the test section from the main valve, the static pressure on the flow side of the test section wall begins dropping from the charge condition to the anticipated run pressure. Since the flap open area and wall open area have a nonzero flow resistance,

the plenum chamber cannot respond instantaneously to the static pressure change at the rear of the test section; thus, a finite wall pressure differential as a function of time develops.

In accord with this physical description, the process may be modeled as illustrated in Fig. 6.11. Let the bottle volume be the plenum volume, V_p , the pressure and density inside the plenum cavity be p_i and ρ_i , respectively, and the temperature inside the cavity and in the flow be uniform, constant, and equal to T . The flow areas of the flaps and porous wall are defined as A_f and A , respectively, with corresponding uniform velocities of u_f and u_i through these areas. The flow quantities $p(t)$ and $\rho(t)$ are the specified pressure and density driving the discharge process.

From continuity, we may show that

$$\rho A u_i + \rho A_f u_f = -V_p (d\rho_i/dt) \quad (6.1)$$

Assume that the flow resistance across the porous walls and through the ejector flap open area may be represented by

$$p_i - p = \rho u_i k a_\infty \quad (6.2)$$

$$p_i - p = \rho u_f k_f a_\infty \quad (6.3)$$

where k is the flow coefficient for the porous walls and k_f is the corresponding parameter for the flap open areas. When substituted into Eq. (6.1), Eq. (6.4) results.

$$\frac{dp_i}{dt} + \left(1 + \frac{A_f k}{A k_f}\right) \frac{p_i}{\tau} = \left(1 + \frac{A_f k}{A k_f}\right) \frac{p}{\tau} \quad (6.4)$$

Here the equation of state has been used, $\rho_i = p_i/RT$ and $\tau = V_p k a_\infty / ART$, where τ corresponds to the plenum chamber response time with the ejector flaps closed. Next, we assume a time variation for p so that Eq. (6.4) may be solved. Since the pressure at the back of the test section must begin at p_{ch} , followed by a drop to p_∞ at the steady-state run condition, an exponential variation in p with time is assumed. This is a reasonable approximation in light of the physical process involved and the observed experimental data. Hence,

$$p = p_\infty \left[1 + (p_{ch}/p_\infty - 1) e^{-t/\tau} \right] \quad (6.5)$$

The parameter τ_v is the characteristic valve time. This characteristic time is a local value, i. e., descriptive of the pressure variation at the rear of the test section. Figure 6.12 shows the contribution to the valve time due to the finite opening rate of the main valve system, $\Delta\tau_v$. Along with this contribution must be added an effective time due to spreading of the expansion wave as it travels up the diffuser. This effect may be approximated by adding to the valve time, $\Delta\tau_v$, the time spreading, $\Delta\tau_s$, at the rear of the test section of a centered expansion wave with origin at the exit of the diffuser. With $\Delta\tau_s$ and $\Delta\tau_v$ known for a particular situation, τ_v may be evaluated.

$$\tau_v = \Delta\tau_v + \Delta\tau_s \quad (6.6)$$

This concept is illustrated in Figs. 6.13 and 6.14. For Pilot HIRT, a $\Delta\tau_s$ of 5.5 msec was calculated based on a tail wave Mach number of $u/a_\infty = 0.5$ (see Fig. 6.13).

Substituting Eq. (6.5) into Eq. (6.4) and defining the characteristic plenum chamber response time for $A_f \geq 0$ as

$$\tau_T \equiv \tau \left(\frac{1}{1 + \frac{k}{k_f} \frac{A_f}{A}} \right) \quad (6.7)$$

we have

$$\frac{d}{dt} p_i + p_i/\tau_T = p_{ch}/\tau_T \left[\mu - (1-\mu) e^{-t/\tau_v} \right] \quad (6.8)$$

where $\mu = p_\infty/p_{ch}$. The solution to Eq. (6.8) subject to the boundary condition that $p_i(t) = p_{ch}$ at $t = 0$ is

$$p_i/p_{ch} = \mu + \frac{1-\mu}{1-\tau_T/\tau_v} \left[e^{-t/\tau_v} - \frac{\tau_T}{\tau_v} e^{-t/\tau_T} \right] \quad (6.9)$$

or

$$\frac{\Delta p}{p_{ch}} = \frac{p_i - p}{p_{ch}} = \frac{1-\mu}{\tau_v/\tau_T - 1} \left[e^{-t/\tau_T(\tau_T/\tau_v)} - e^{-t/\tau_T} \right] \quad (6.10)$$

Equation (6.10) gives the pressure differential across the porous wall during the starting process as a function of the ratio τ_v/τ_T , the charge pressure, p_{ch} , and μ . Figure 6.15 is a plot of $\Delta p/p_{ch}(1-\mu)$ versus nondimensional time, t/τ_T , for variations in t_v/t_T . Thus, wall loads are similar for different configurations if τ_v/τ_T , τ_T , p_{ch} , and μ remain constant. From Fig. 6.15, it is also apparent that for a given τ_v/τ_T there is a maximum in $\Delta p/p_{ch}(1-\mu)$ located at a unique t/τ_T . Thus, define the unique value of t/τ_T where $\Delta p/p_{ch}(1-\mu)$ is maximum as t_p/τ_T . Figure 6.16 is a plot of this relationship. As an example, let $\tau_v/\tau_T = 4.7$, then the peak occurs at $t_p/\tau_T = 2$ and the maximum dimensionless differential pressure, $[\Delta p/p_{ch}(1-\mu)]_{max}$, is 0.135. Figure 6.17 is a composite plot of $[\Delta p/p_{ch}(1-\mu)]_{max}$ versus τ_v/τ_T where t_p/τ_T has been eliminated.

This is, in essence, the information necessary to scale the pilot tunnel wall load data to a larger scale facility. Before this can be done, however, a careful examination of the parameters characterizing the wall differential pressure must be made.

In order to evaluate the parameter, τ_T , the wall and ejector flap flow coefficients along with the effective flow areas, A and A_f , must be evaluated. For the flap, the flow area A_f is simply the flap open area normal to its flow. The porous wall flow area, however, is not quite as obvious. It must depend on both porosity and flow distribution as indicated in Figs. 6.7, 6.8, and 6.9. The wall flow area will be defined such that the integral of the maximum wall differential during the starting process (proportional to the maximum flow rate across the wall), as shown in Fig. 6.7, over the test section wall area is equal to the maximum wall differential for each configuration times the flow area, A . This leads to a definition of the wall flow area, A , given by

$$A \cong 0.17 \tau_w A_W \text{ for } A_f \geq 0, \tau_w \geq 0 \quad (6.11)$$

where τ_w is the wall porosity and A_W is the total test section wall area. Figure 6.18 illustrates the application of the previous concept to obtain Eq. (6.11).

With the establishment of the flow areas A_f and A , the values of the flow coefficients k and k_f were evaluated using data from the 16-in. valve case only (Fig. 6.7) as inputs to the model as given in Fig. 6.17 and Eq. (6.7). The variation of k with porosity was found using the applicable results of Jacocks and Banks (Ref. 9). The flow coefficients k and k_f where k is a function of porosity and k_f is a function of flap open area

are presented in Figs. 6.19 and 6.20, respectively. The nature of these coefficients is assumed to remain the same in scaling from the Pilot HIRT to larger scale configurations for similar wall and flap geometry. Here, the values obtained for k and k_f assume that T is constant and equal to the charge temperature, T_{ch} , of 530°R . For scaling purposes, the variation of T with time is not significant. Pilot HIRT studies have shown that the plenum chamber temperature and flow static temperature at the rear of the test section are different, and moreover, that the local plenum chamber temperature variation with time drops from T_{ch} (530°R) to values near T_o (480°R) during a run, the exact value depending upon the test section Mach number. The time variation of T , however, is still of secondary importance compared to p in defining the wall pressure differential.

As a check on the ability of the model developed to predict maximum wall loads, data obtained using the diaphragm starting device were reduced and plotted on the curve of $[\Delta p/p_{ch}(1-\mu)]_{\max}$ versus τ_v/τ_T (Fig. 6.17), and is given in Fig. 6.21. The data presented includes variations in flap area from $0.1 A_{ts}$ to $0.46 A_{ts}$ and porosity ($\tau_w = 4.5$ and 1.5 percent) for a characteristic valve time of 5.5 msec. Agreement of this data and the theoretical curve is seen to be quite good. Since a full-scale facility with a nominal test section cross-sectional area of 80 sq ft would have a characteristic valve time on the order of 170 msec (13 msec scaled to Pilot HIRT), which is bounded by the diaphragm and 16 -in. valve cases, the evaluation of full-scale wall loads by the present method is expected to be sufficiently accurate.

Figure 6.22 is a plot of the maximum differential pressure coefficient versus the flap open area ratio, A_f/A_{ts} for different values of porosity, τ_w for a typical HIRT with $\tau_v = 100$ msec, $T = 530^\circ\text{R}$, and $V_p/V_{ts} = 2.5$ where V_{ts} is the test section volume. This figure gives conservative estimates of the maximum wall pressure differential for a full-scale tunnel since τ_v should be about 170 msec (100 -msec valve open time plus 70 -msec wave spreading) and V_p/V_{ts} would normally be less than two which would lower the magnitude of these curves significantly. The plot does show, however, the strong influence of τ_w at low A_f/A_{ts} and the marked reduction of $[\Delta p/p_{ch}(1-\mu)]_{\max}$ for increasing A_f/A_{ts} .

6.4 FLAP LOADING

The experimental investigation of ejector flap loading in the Pilot HIRT involved the determination of the maximum flap loading anticipated in the routine operation of the facility. In order to provide this information, the parameters influencing these loads are reviewed. The ejector flap design as tested in Pilot HIRT is schematically indicated in Fig. 6.3, and

the experimental flap loads presented here are restricted to this configuration. The tunnel operating conditions which influence flap loads are charge pressure, p_{ch} ; test section Mach number, M_∞ ; ejector flap opening, A_f/A_{ts} ; wall porosity, τ_w ; plenum volume, V_p/V_{ts} ; plenum auxiliary flow rate, \dot{w}_A ; and the characteristic valve opening time, τ_v . Each of the parameters, with its contribution to the maximum flap loads, will be discussed.

The maximum flap loading occurs during the starting process of the tunnel when the expansion fan from the flow starting mechanism arrives at the flaps. This drops the pressure over the surface of the flaps very rapidly while setting the gas in the test region in motion. The pressure drop behind the flaps, inside the plenum, lags the primary flow pressure drop because of the flow resistance of the flap opening and test section wall holes. When auxiliary plenum flow is used as an operational parameter, the plenum response time can be much reduced, which tends to reduce these flap loads. Thus, the maximum anticipated flap loads would occur when testing at the maximum test section Mach number (near $M_\infty = 1.0$) where auxiliary plenum flow is not required.

Throughout this flap load study, the plenum-volume-to-test-section-volume ratio, V_p/V_{ts} , was 2.5. Recent Pilot HIRT results indicate that as V_p/V_{ts} is decreased to about 1.8 the flap loads are also decreased.

Figure 6.3 indicates the location of the four differential pressure transducers mounted on the flap, which provide the Δp time histories over the flaps. Typical pressure time histories are shown in Fig. 6.23 and these data show the time at which the maximum Δp loading occurs is dependent on the characteristic valve opening time, τ_v , and on the flap open area ratio, A_f/A_{ts} . During the experiment, τ_v was varied from 5.5 msec using the Mylar[®] diaphragm opening mechanism to near 80 msec using the 16-in. sliding sleeve valve opening mechanism. The characteristic opening time, τ_v , for the 16-in. sliding sleeve valve ranged from 40 msec (24 ports case) to 80 msec (14 ports case).

Figure 6.24 shows the variation of the streamwise maximum differential pressure coefficient $[\Delta p/p_{ch}]_{max}$ over the flap surface. These data indicate that the magnitude of the maximum flap loading is largely dependent on the characteristic valve opening time which determines the severity of the pressure gradient within the starting expansion fan and that the maximum flap loading can be substantially decreased by increasing τ_v and A_f/A_{ts} .

The data presented have been for set wall porosities, τ_w , of about 4.5 percent. When two-thirds of the wall holes were taped closed, leaving a τ_w of about 1.5 percent, the results indicated no significant loading change over the flaps for the case where $A_f/A_{ts} = 0.2$ and $\tau_v = 5.5$ msec.

Figure 6.25 is a plot of the maximum flap load averaged over the flap length against the ratio of the characteristic valve time, τ_v , to the characteristic response time of the plenum, τ_T . Figure 6.26 shows the maximum flap load trend at the downstream edge of the flap versus the characteristic response parameter, τ_v/τ_T . From these data, one can see a slight chord-wise load gradient over the flap for the configurations of interest, i. e., $1 < \tau_v/\tau_T < 10$.

Figure 6.27 displays the pilot tunnel results indicating the ratio of maximum pressure load on the flap to the steady-state measurements for two cases of diffuser flow as a function of flap open area. These data indicate that the maximum flap loading is primarily a function of τ_v/τ_T and is relatively independent of the diffuser flows (subsonic and supersonic) investigated. These Pilot HIRT flap data also indicate at the lower values of A_f/A_{ts} a substantial reduction in the steady-state flap loading as the number of open ports in the 16-in. valve is decreased from 24 to 14. These trends may be indicative of the influence of diffuser performance (shock location) on the flap loading at steady-state flow conditions.

In order to extrapolate the Pilot HIRT flap data, an account must be made of the envisioned flap design for a full-scale facility as compared to the pilot facility. Figure 6.28 shows schematically the pilot and a full-scale facility flap design. As shown, the two flap designs are quite a bit different. The pilot facility design has only one opening at the back of the test section, resulting in loading over the entire flap during the starting process. The modified full-scale design, however, has its hinge point moved forward on the flap (compared to the pilot facility), which allows a reduction in flap loading during the starting process. In the run position, $A_f/A_{ts} \leq 0.2$, though, the full-scale and pilot designs should yield comparable load distributions. Thus, the maximum flap loads, as obtained from Figs. 6.25 and 6.26 will be corrected to include a larger scale facility configuration as depicted in Fig. 6.28. Steady-state flap loads are assumed the same as Pilot HIRT loads for similar configurations.

First, an examination of the case for flaps in the full open position will be made. This would correspond to runs with moderate to high charge pressures (above 400 psia), referring to previous considerations on wall loads. The longitudinal pressure distributions as shown in Fig. 6.29 will be assumed for the proposed configuration where, during the tunnel starting process, flow over the upstream and under the downstream end of the flap is choked. From a physical point of view, this assumption seems reasonable and is strengthened by the Pilot HIRT distributions (Fig. 6.24). Since the area distribution behind the flap is approximately constant for the full open position (see Fig. 6.28), the pressure behind the flap is assumed uniform and equal to the time-dependent value at the upstream end of the flap. Thus, imposing the assumed physical process as described and assuming that the pressure distribution over the top of the flap is similar to the distribution obtained in Pilot HIRT (Fig. 6.25 and 6.26), the peak value of $(\Delta p/p_{ch})_{max}$ may be determined for the larger scale facility ejector flap configuration in its full open position ($A_f \geq 0.35 A_{ts}$ where, now, A_f is the total flow area on both ends of the flap).

The resulting peak $(\Delta p/p_{ch})_{max}$ as a function of τ_v/τ_T is given in Fig. 6.30. This figure indicates that as τ_v is decreased or τ_T is increased, the peak $(\Delta p/p_{ch})_{max}$ decreases. Thus, considering the model proposed, increasing the valve opening time tends to increase peak differential pressures across the flap if all other variables are held constant.

By examination of Figs. 6.28 and 6.29 for small A_f/A_{ts} (< 0.2) the flow area at the downstream end of the plenum side of the flap will be on the order of one-fourth the flow area of the upstream end of the plenum side of the flap assuming the position of pivot point as shown. Therefore, a large portion of the volume on the plenum side of the flap will approach a uniform pressure equal to the unsteady plenum pressure. This implies that the load distribution for a normal run configuration ($A_f/A_{ts} \leq 0.2$) for the larger scale facility flaps is approximately simulated by the Pilot HIRT flaps with the same run configuration and that Figs. 6.25 and 6.26 may be used directly to obtain valid estimates of the maximum flap load distributions for $A_f/A_{ts} \leq 0.2$. Moreover, as $A_f/A_{ts} \rightarrow 0$, the load estimates for the envisioned HIRT flaps will approach monotonically the Pilot HIRT distributions as given in Figs. 6.25 and 6.26.

In order to afford the highest degree of versatility in the modeling of the flap loading process for a larger scale facility, the preceding results will be used to formulate a model of the loading process that is

not restricted by the pivot point location (as indicated in Fig. 6.29) or by the flap open area ratio (i. e., Fig. 6.30). A relaxation of these two restrictions will produce a complete picture of the transient load environment on the flaps for most flap geometries of interest. Let us assume that the streamwise flow area distribution on the plenum side of the flap is single valued and that the flow area on the plenum side of the upstream end of the flap, A_{UE} , is always greater than or equal to the flow area on the plenum side of the downstream end of the flap, A_{DE} . Figures 6.25, 6.26, and 6.30 as applied to the full-scale design give precisely two data points to define loading as a function of flap geometry. Figures 6.25 and 6.26 describe the case for $A_{DE} = 0$ and Fig. 6.30 gives results for $A_{DE}/A_{UE} = 1.0$. Hence, we require the maximum pressure coefficient for the upstream and downstream edge of the flap (assuming a linear variation over the flap length) for $0 \leq A_{DE}/A_{UE} \leq 1.0$.

For A_{DE}/A_{UE} single valued and small, a majority of the flow on the plenum side of the flap will be essentially incompressible leading to a local plenum pressure behind the flap proportional to $(A_{DE}/A_{UE})^2$. As $A_{DE}/A_{UE} \rightarrow 1.0$, the flow on the plenum side of the flap approaches sonic, constant density conditions. Thus, it is reasonable to assume that, locally, the differential pressure coefficient across the flap varies directly with $(A_{DE}/A_{UE})^2$. With the local values of $(\Delta p/p_{ch})_{max}$ known for $A_{DE}/A_{UE} = 0$ and 1.0 , the variation of $(\Delta p/p_{ch})_{max}$ with A_{DE}/A_{UE} is defined explicitly. Figure 6.31 gives the information necessary to calculate the maximum differential pressure coefficient for the upstream and downstream edge of an ejector flap with the pivot point located arbitrarily along its streamwise length (see Fig. 6.28) and for $0 \leq A_{DE}/A_{UE} \leq 1.0$ where $(\Delta p/p_{ch})_{max}$ is assumed to vary linearly. Then, Fig. 6.31 results from a combination of Figs. 6.25, 6.26, and 6.30. With reference to Fig. 6.31, when $A_{DE}/A_{UE} = 0$ $(\Delta p/p_{ch})_{max} = c_{UE}$ for the upstream edge and $(\Delta p/p_{ch})_{max} = c_{DE}$ for the downstream edge which reduces Fig. 6.31a to a composite plot of Figs. 6.25 and 6.26. This case corresponds exactly to the Pilot HIRT flap geometry. As $A_{DE}/A_{UE} \rightarrow 1.0$ holding A_f/A_{ts} constant, the upstream edge $(\Delta p/p_{ch})_{max} \rightarrow 0$ and the downstream edge $(\Delta p/p_{ch})_{max}$ is evaluated from Figs. 6.31a and 6.31c leading to the results as presented earlier.

During a normal Pilot HIRT and a larger scale tunnel run, steady-state conditions are established following the starting process. Thus, maximum values of the steady-state flap loads were determined. It was experimentally found that, for $A_f/A_{ts} \geq 0.1$, flap loads were always less than or equal to a uniform Δp across the flap of $0.1 p_{ch}$ with a simulated sector installed and 14 ports on the 16-in. sliding sleeve

valve open. The 14-port open case scales approximately to a full-scale HIRT with a subsonic diffuser design. This maximum value of the steady-state wall load in all cases considered is less than the maximum starting loads. Therefore, from a design standpoint, the steady-state loading imposes no constraints except that $A_f/A_{ts} \geq 0.1$ during the run. If $A_f/A_{ts} < 0.1$, uniform flap Δp loads of $0.3 p_{ch}$ may be encountered.

During a run, conceivable full-scale tunnel operation would require that the main valves be closed at the end of the first constant pressure plateau, thus conserving high-pressure air. This would produce a transient load situation on the walls and flaps similar to those encountered during the starting process. In order to examine this loading mechanism, an experimental test was undertaken. In order to achieve a simulation of main valve closure, the 12-in. SSV was driven shut early in the pilot tunnel run. An examination of the resulting experimental data indicated that wall and flap loadings occurring during valve closure are of the same order of magnitude as the starting loads, and a streamwise differential pressure gradient along the test section wall forms for the stopping process in a manner similar to the starting process. Thus, from the limited amount of data gathered, it was concluded that stopping loads may be modeled in a manner similar to the starting loads problem and, moreover, that the magnitude of the stopping loads, for all cases of practical interest, will be bounded by and be opposite in direction to the equivalent starting load as described earlier.

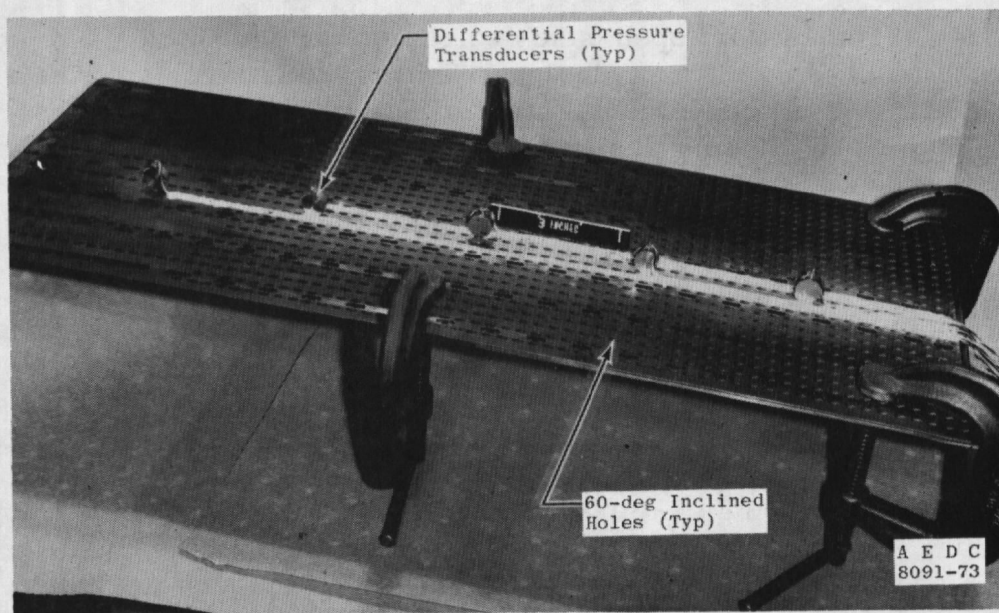


Figure 6.1. Installation view showing back of porous wall with differential transducers.

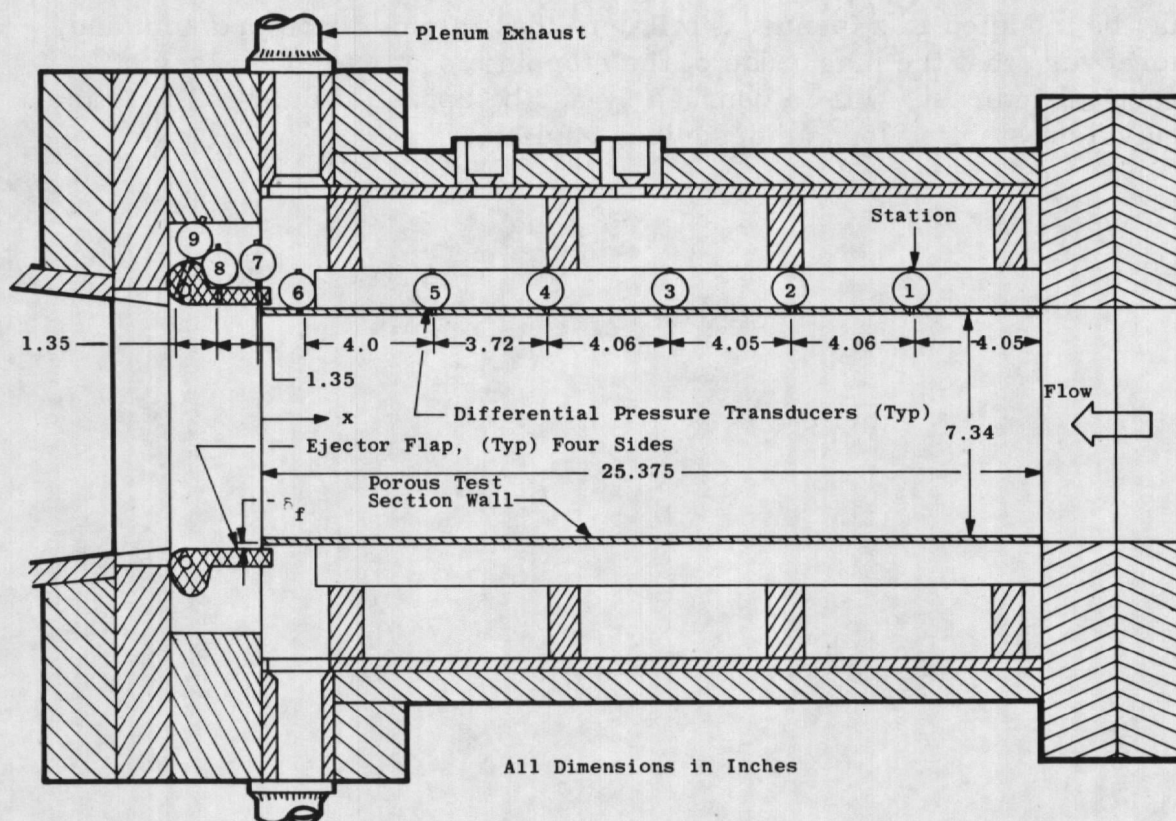


Figure 6.2. Schematic of test section showing location of differential transducers.

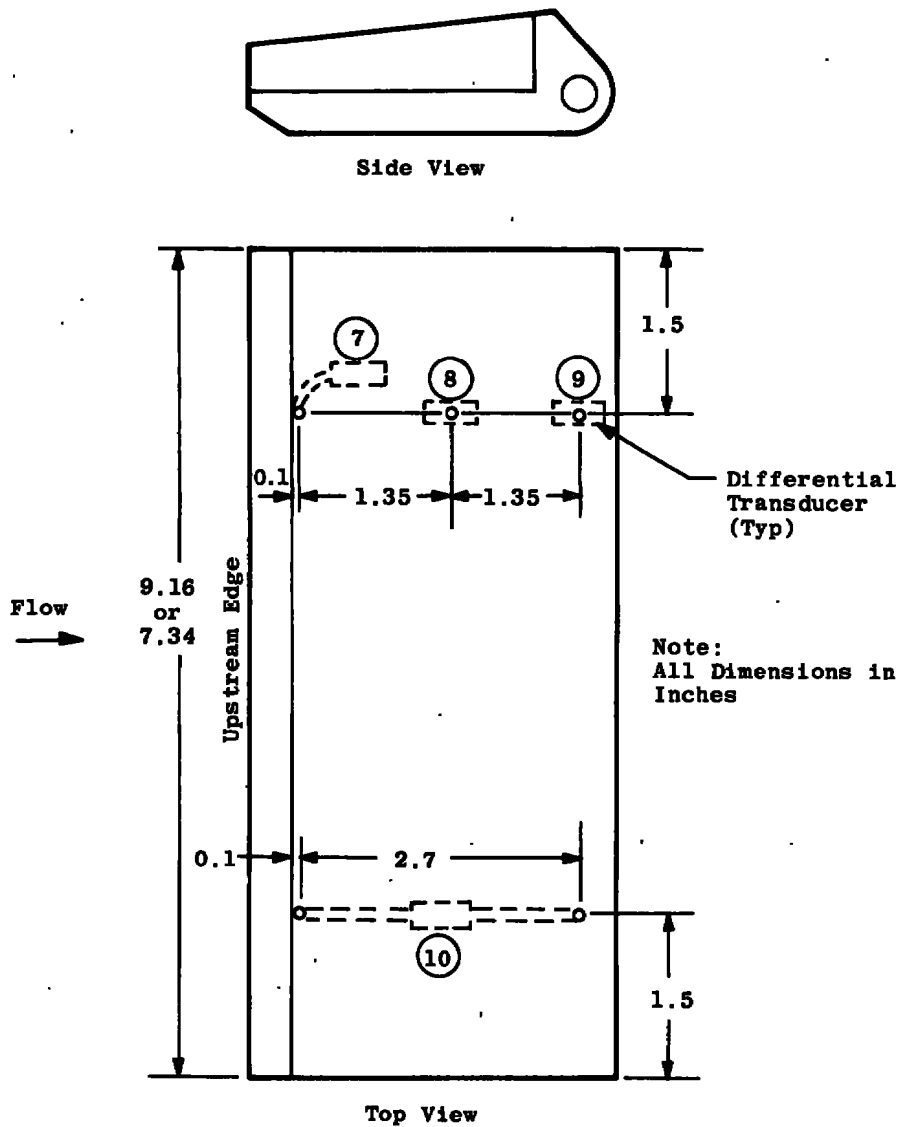


Figure 6.3. Detail of instrumented ejector flap.

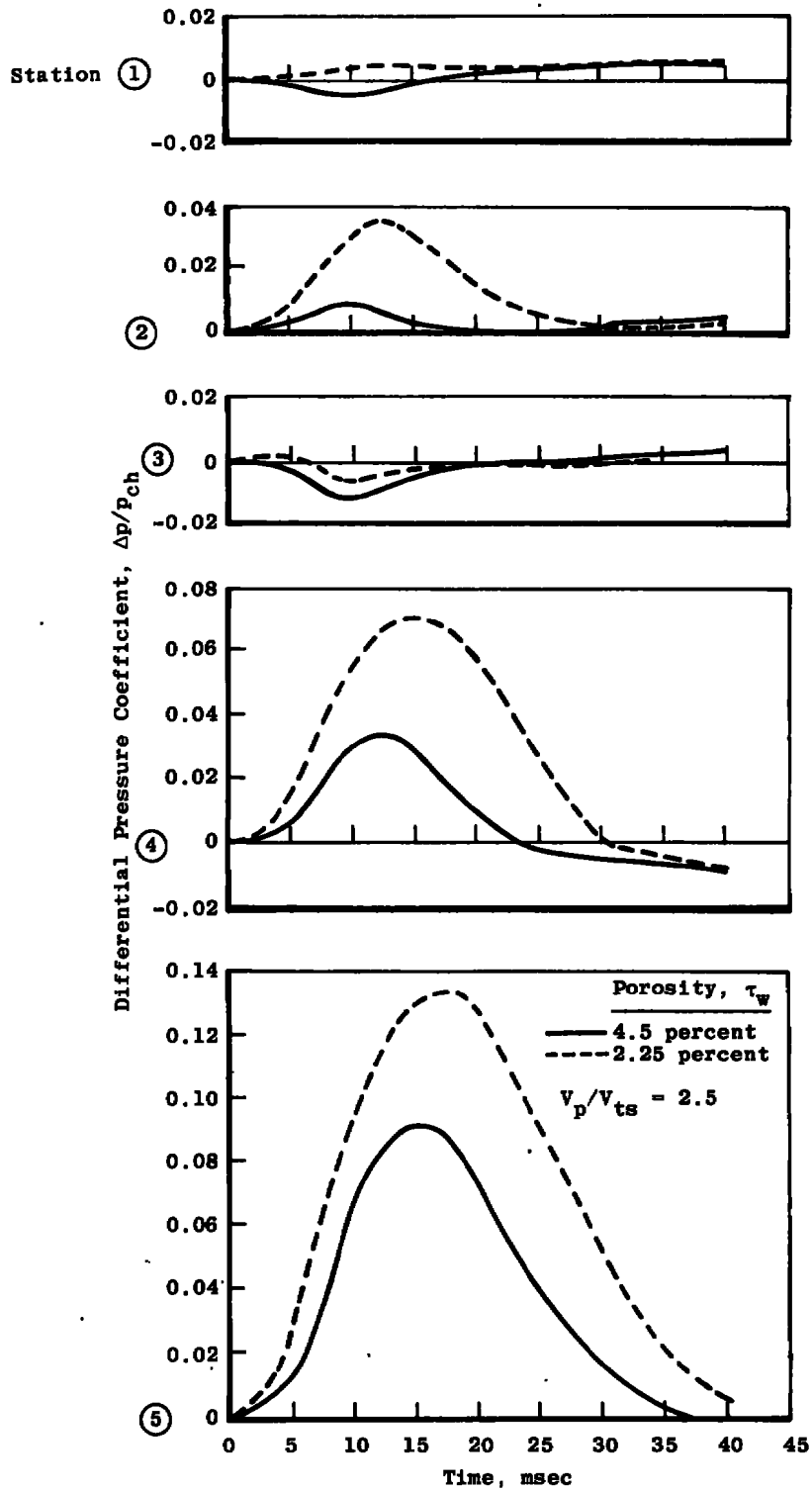


Figure 6.4. Wall loading during the starting process at five stations as shown in Fig. 6.2 for variations in wall porosity with $p_{ch} = 100$ psia, $A_f/A_{ts} = 0.0$, 12-in. SSV starting device.

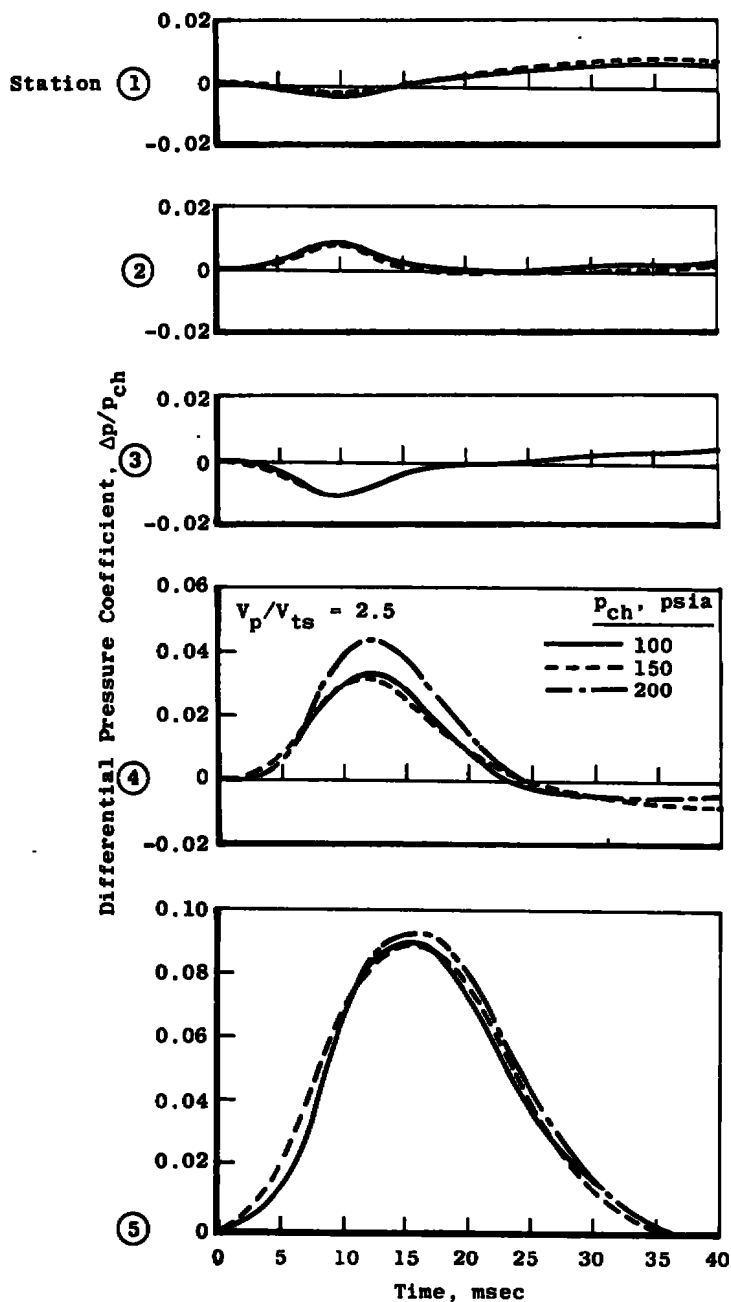


Figure 6.5. Wall loading during the starting process at five stations as shown in Fig. 6.2 for variations in the charge pressure, p_{ch} , at a porosity of 4.5 percent, $A_1/A_{ts} = 0.0$, 12-in. SSV starting device.

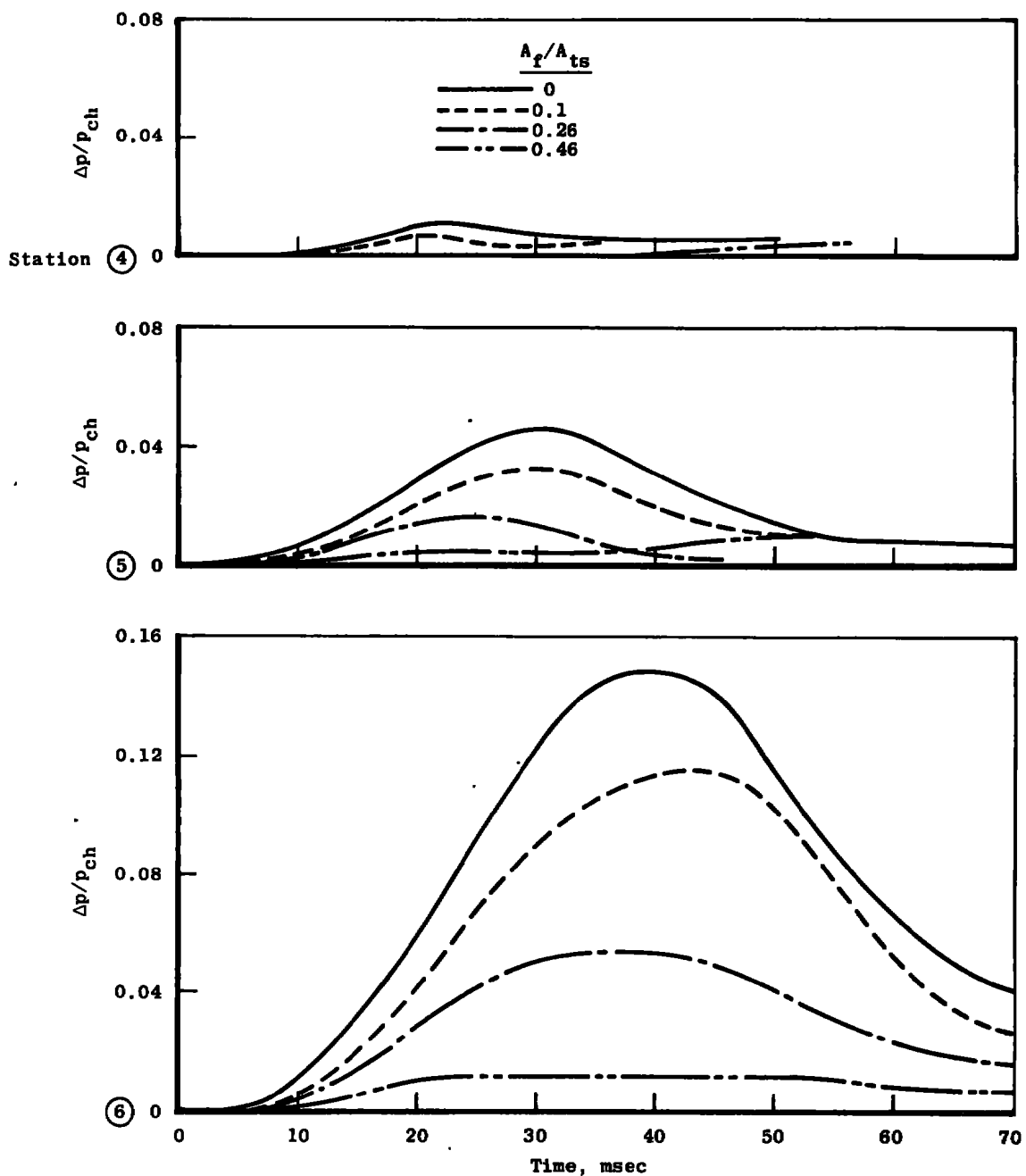


Figure 6.6. Wall loading during the starting process at three stations as shown in Fig. 6.2 for variable flap opening at a wall porosity of 4.5 percent, $V_p/V_{ts} = 2.5$, 16-in. SSV starting device.

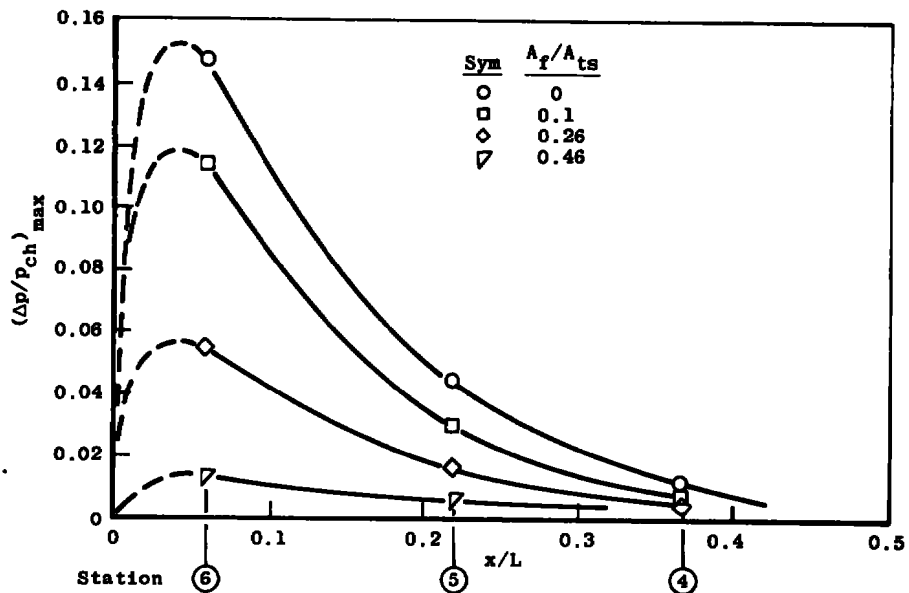


Figure 6.7. Maximum wall loading during the starting process as a function of flap opening and axial position measured from back of test section for a wall porosity of 4.5 percent, $V_p/V_{ts} = 2.5$, 16-in. SSV starting device.

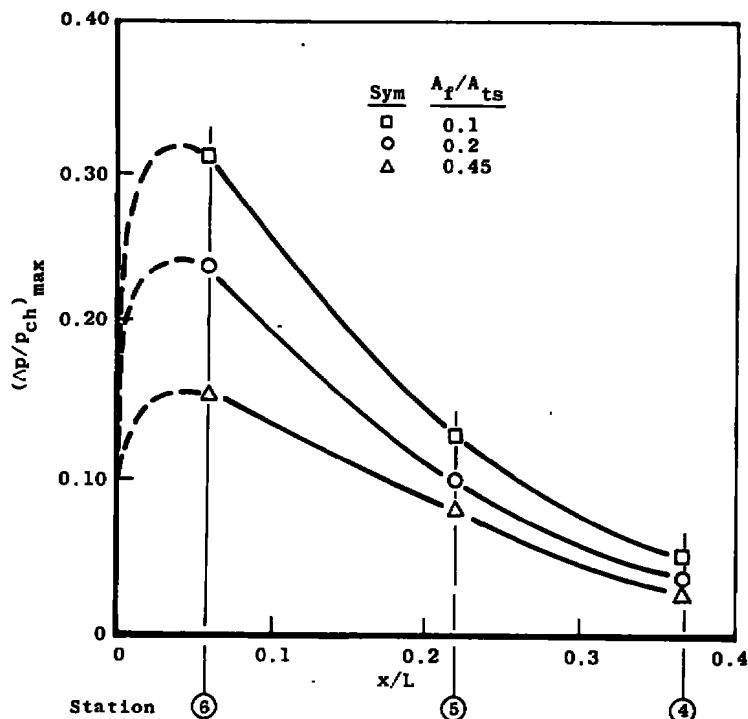


Figure 6.8. Maximum wall loading during the starting process as a function of flap opening and axial position measured from back of test section for a wall porosity of 4.5 percent, $V_p/V_{ts} = 2.5$, diaphragm starting device.

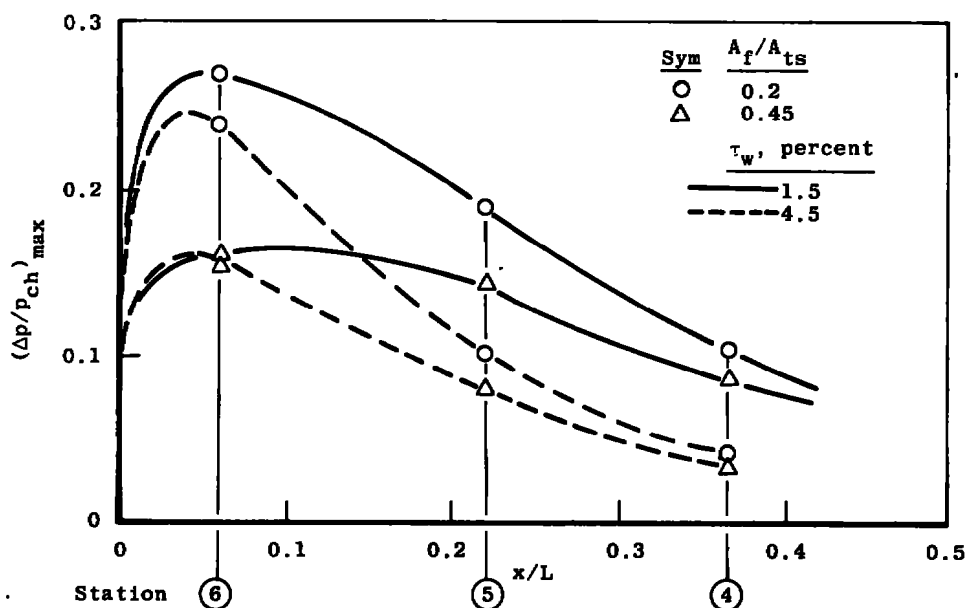


Figure 6.9. Maximum wall loading during the starting process as a function of porosity, τ_w , flap opening and axial position for $V_p/V_{ts} = 2.5$, diagram starting device.

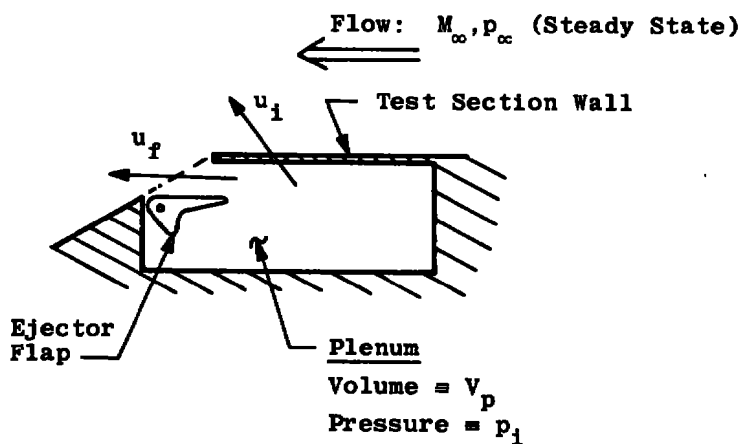


Figure 6.10. Schematic of plenum discharge process.

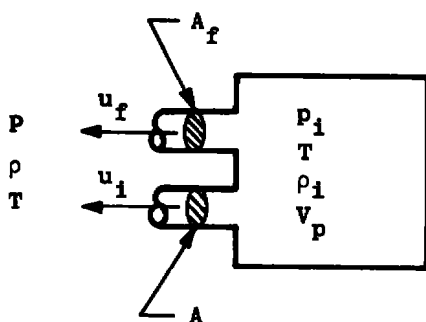


Figure 6.11. Model of plenum discharge process.

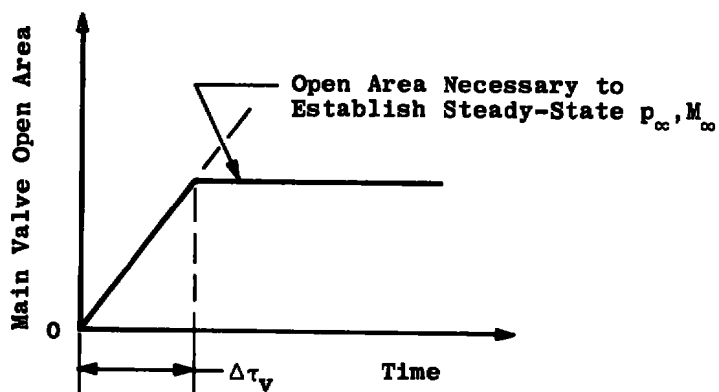


Figure 6.12. Illustration of main valve opening as a function of time.

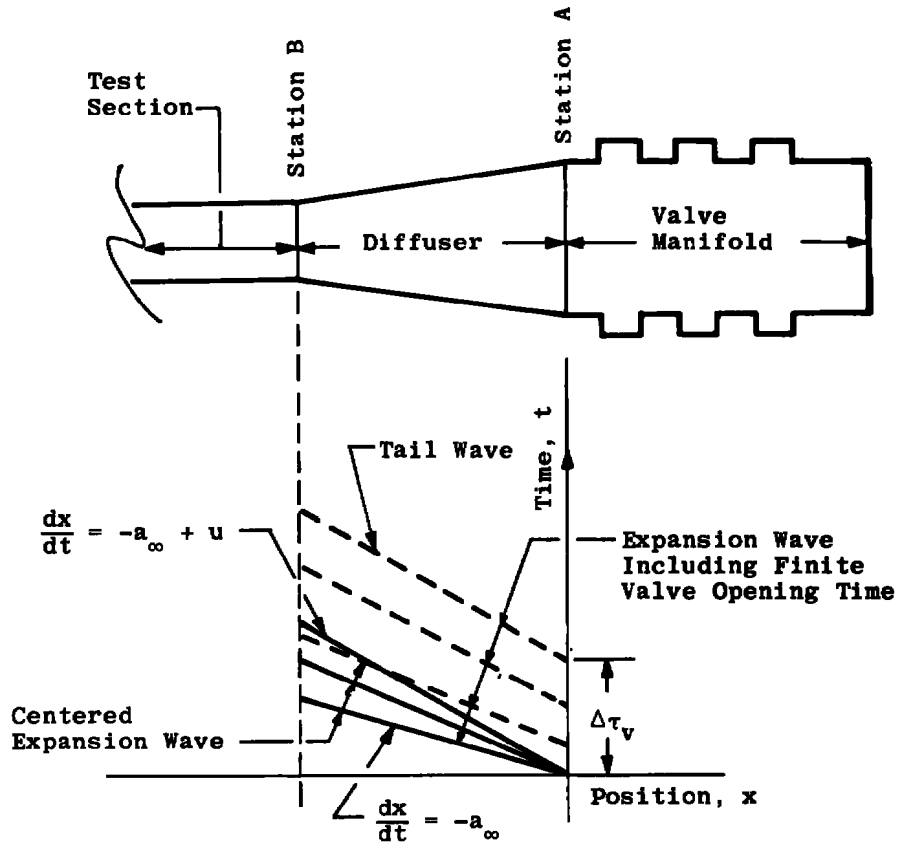


Figure 6.13. Simplified wave diagram for diffuser and valve.

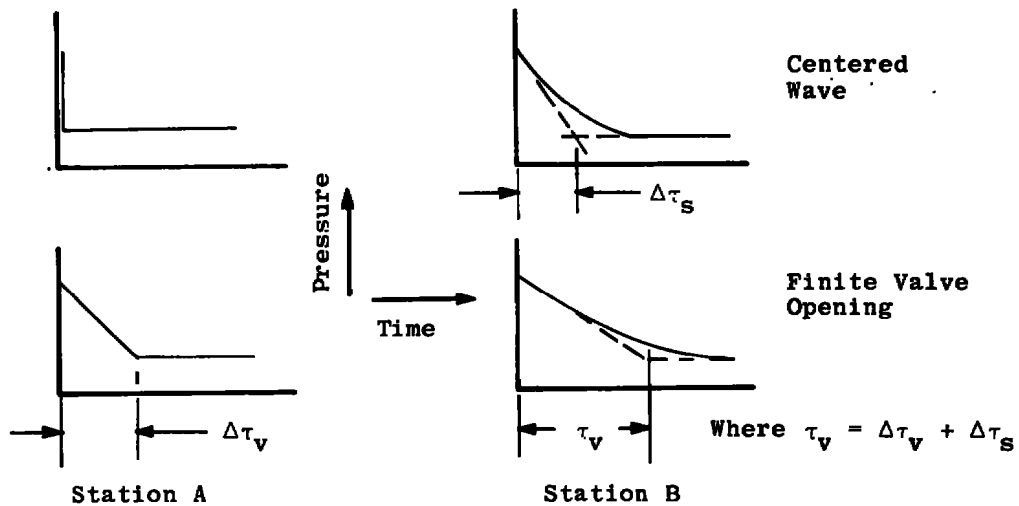


Figure 6.14. Pressure histories of start process at Stations A and B as depicted in Fig. 6.13.

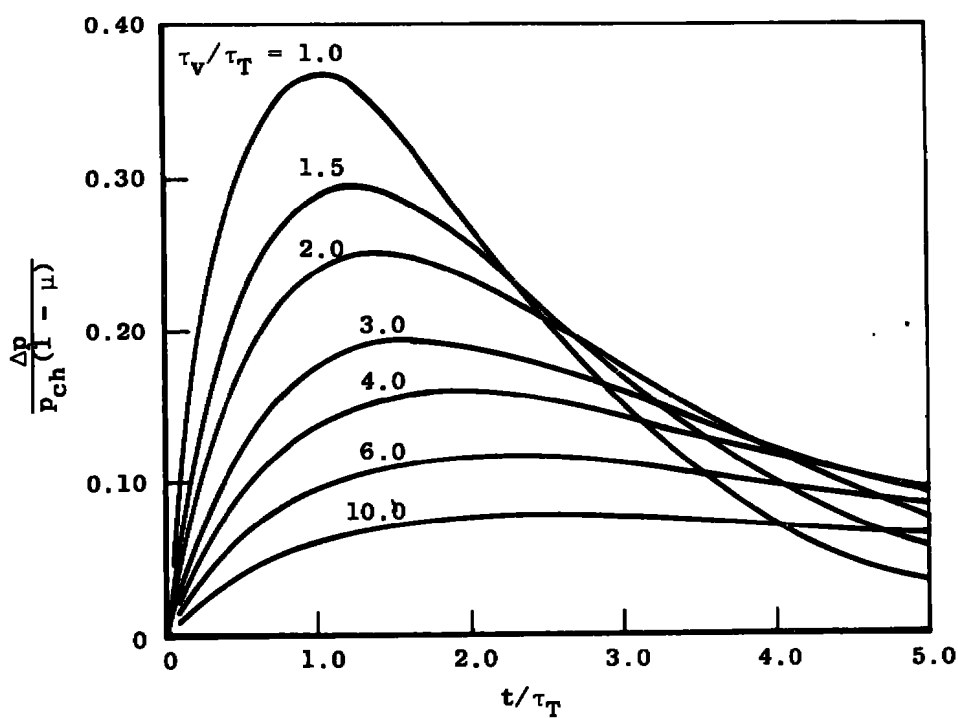


Figure 6.15. Nondimensional differential pressure across the porous wall as a function of nondimensional time, t/τ_T , for various values of τ_v/τ_T , theoretical.

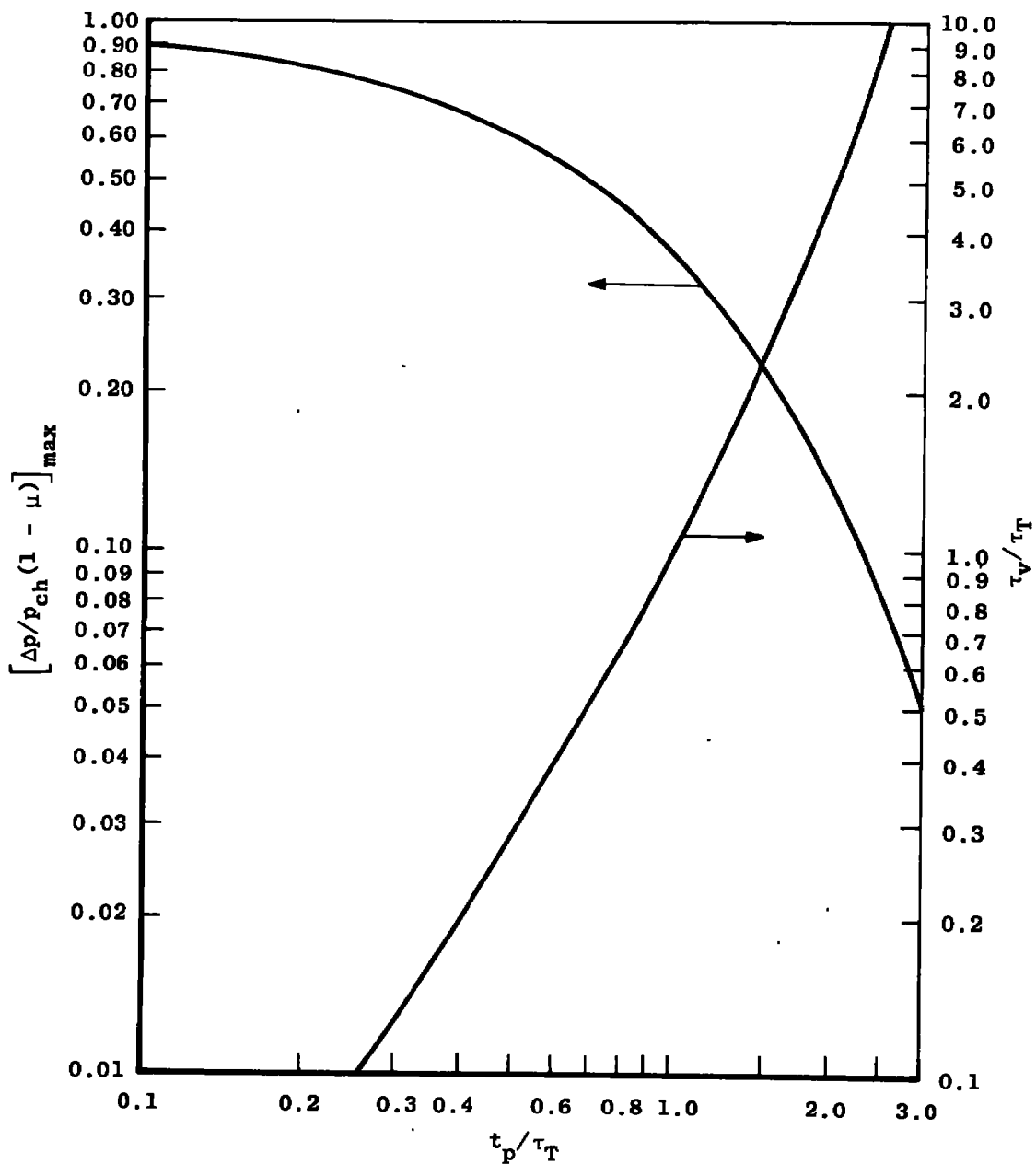


Figure 6.16. Maximum differential pressure coefficient and the ratio τ_v/τ_T versus the nondimensional peak time, t_p/τ_T , theoretical.

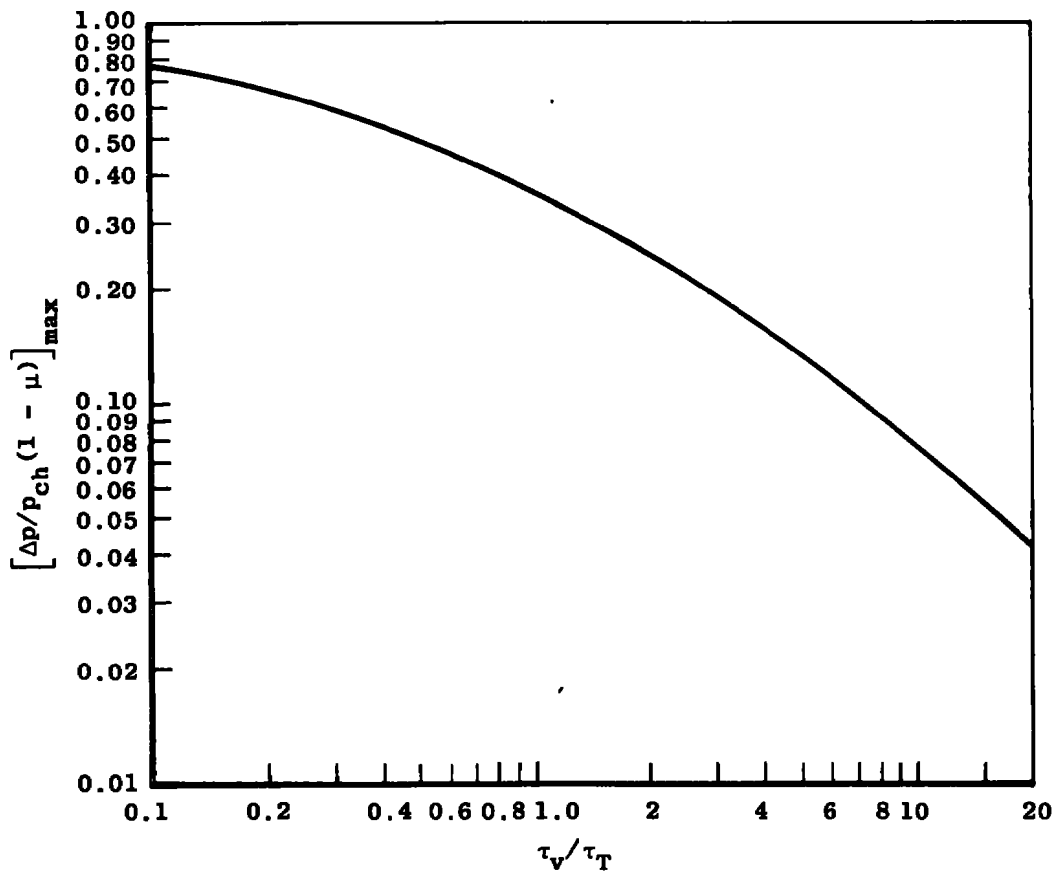


Figure 6.17. Maximum differential pressure coefficient as a function of the ratio τ_v/τ_T , theoretical.

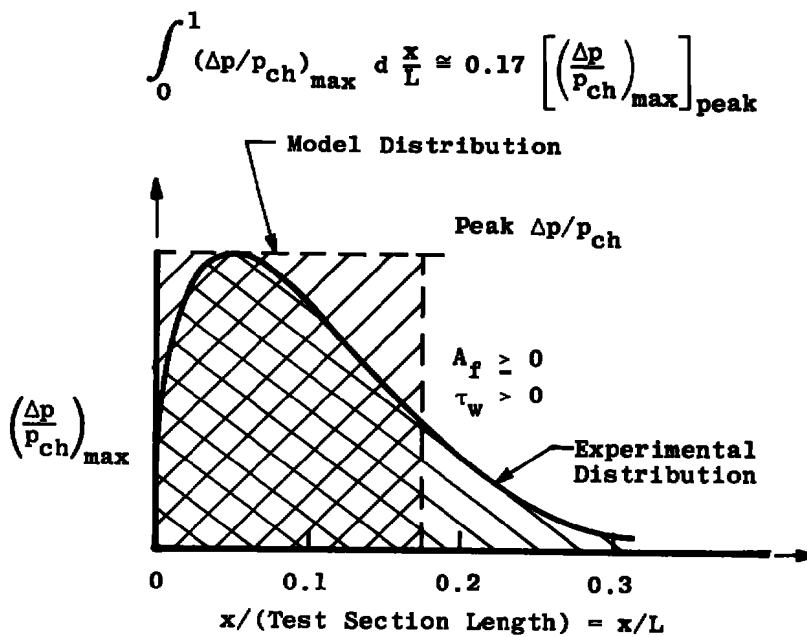


Figure 6.18. Illustration of model of axial pressure differential.

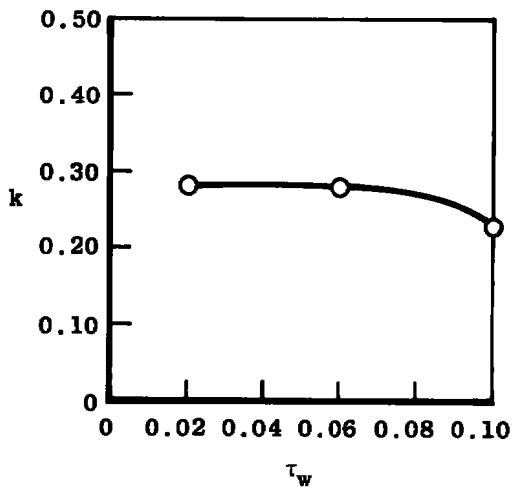


Figure 6.19. Porous wall flow coefficient versus porosity, τ_w .

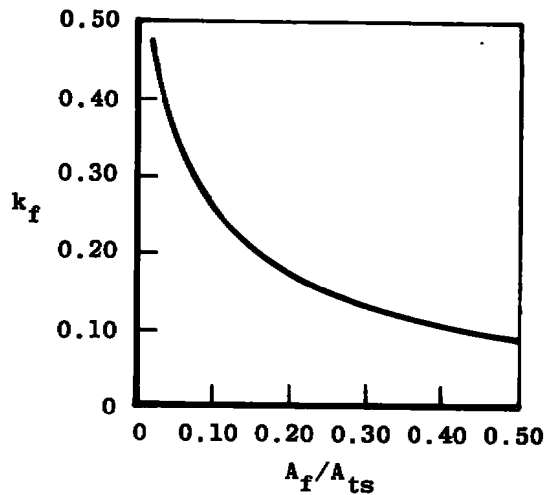


Figure 6.20. Ejector flap flow coefficient versus area ratio, A_f/A_{ts} .

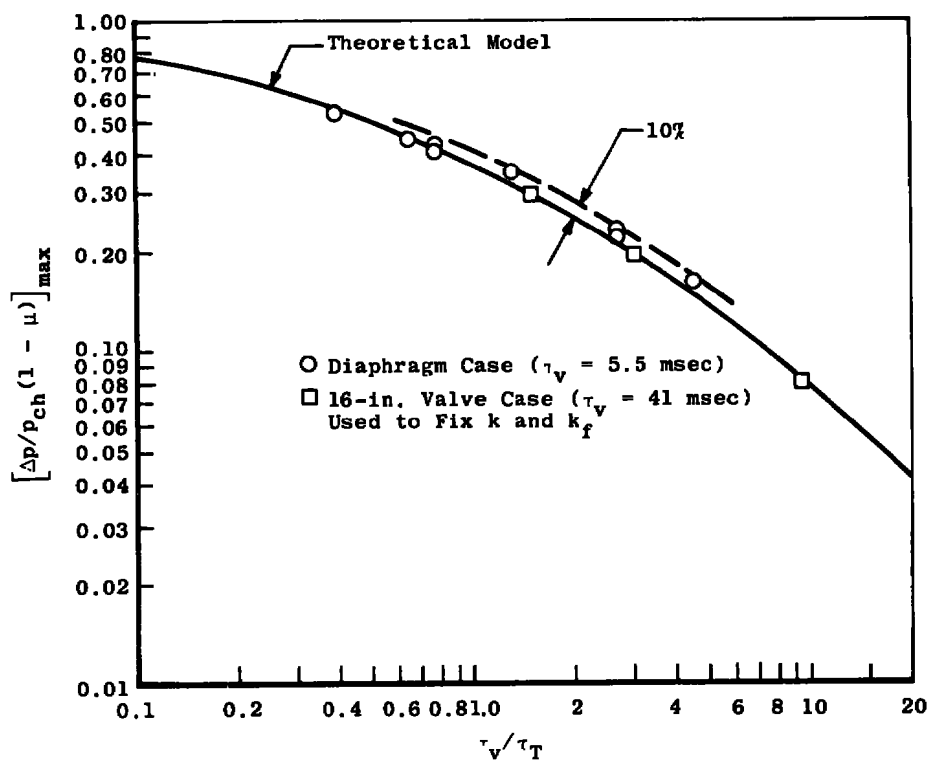


Figure 6.21. Maximum differential pressure coefficient as a function of the ratio τ_v/τ_T showing data for $\tau_v = 5.5$ msec, diaphragm case.

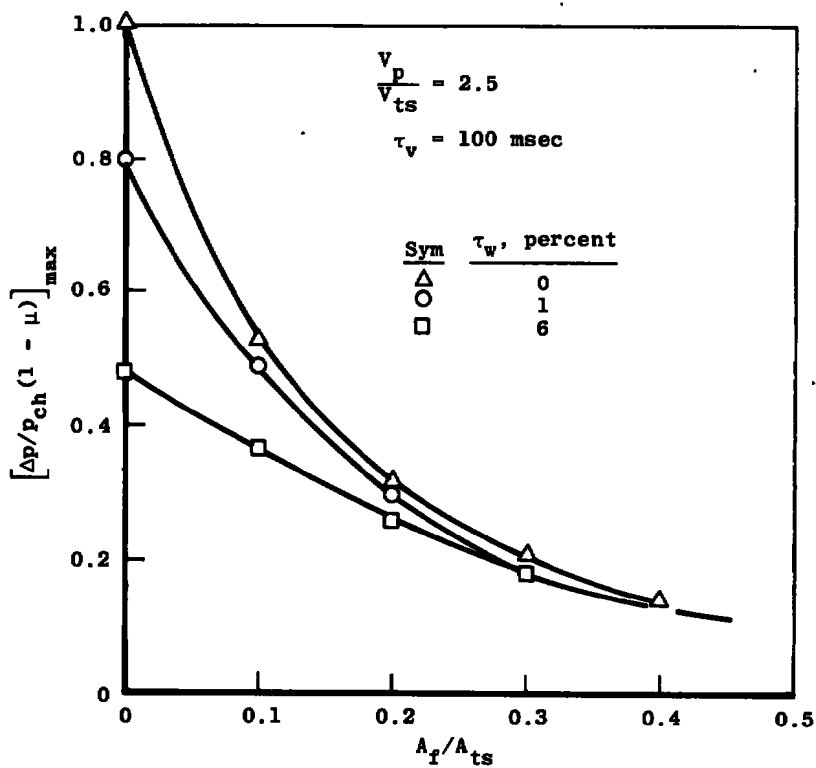


Figure 6.22. Maximum differential pressure coefficient versus A_f/A_{ts} showing influence of τ_w for $\tau_v = 100 \text{ msec}$, $V_p/V_{ts} = 2.5$, theoretical.

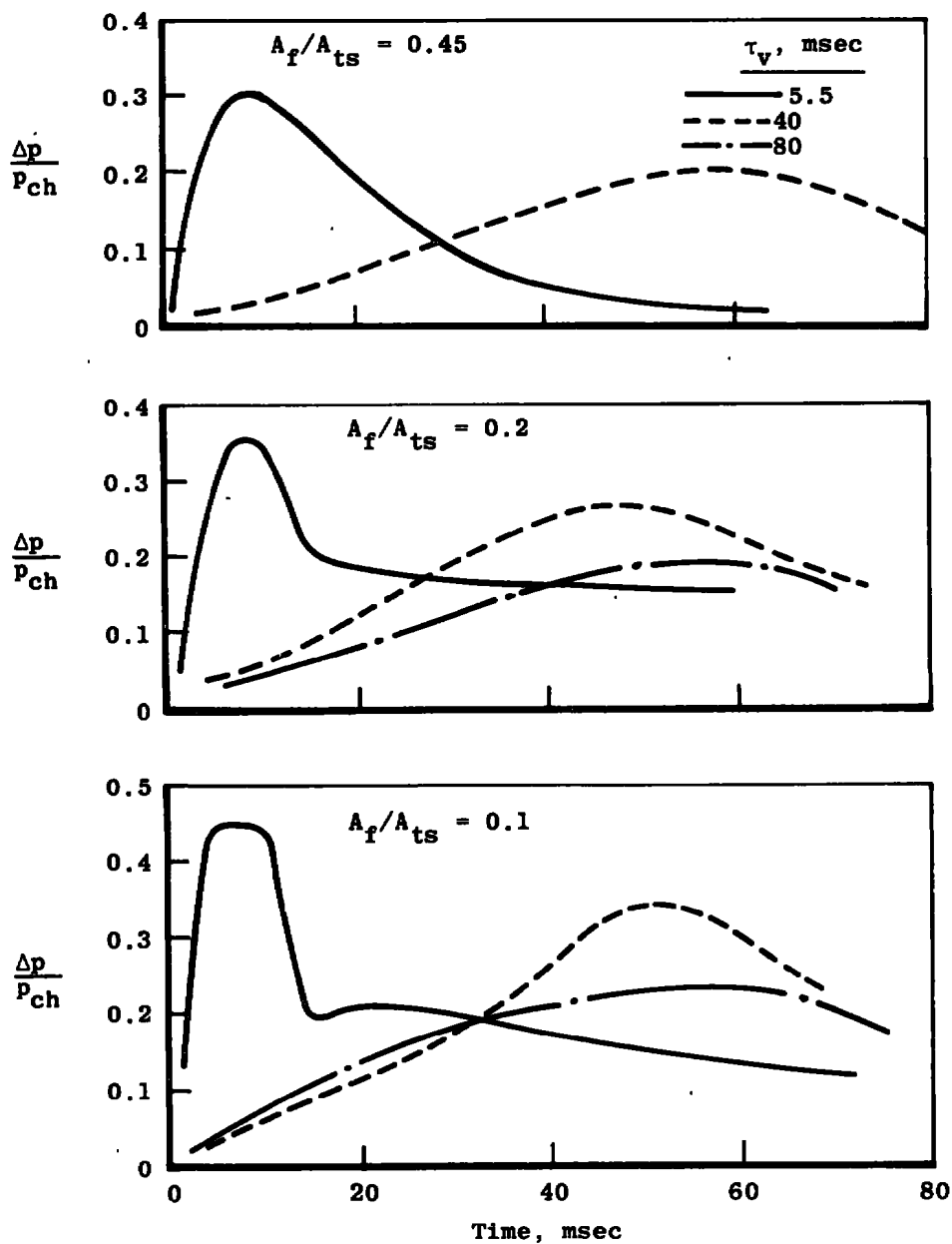


Figure 6.23. Time histories of flap loading at station 7 (see Figs. 6.2 and 6.3) for variations in characteristic valve opening time, τ_v , and flap open area, A_f/A_{ts} .

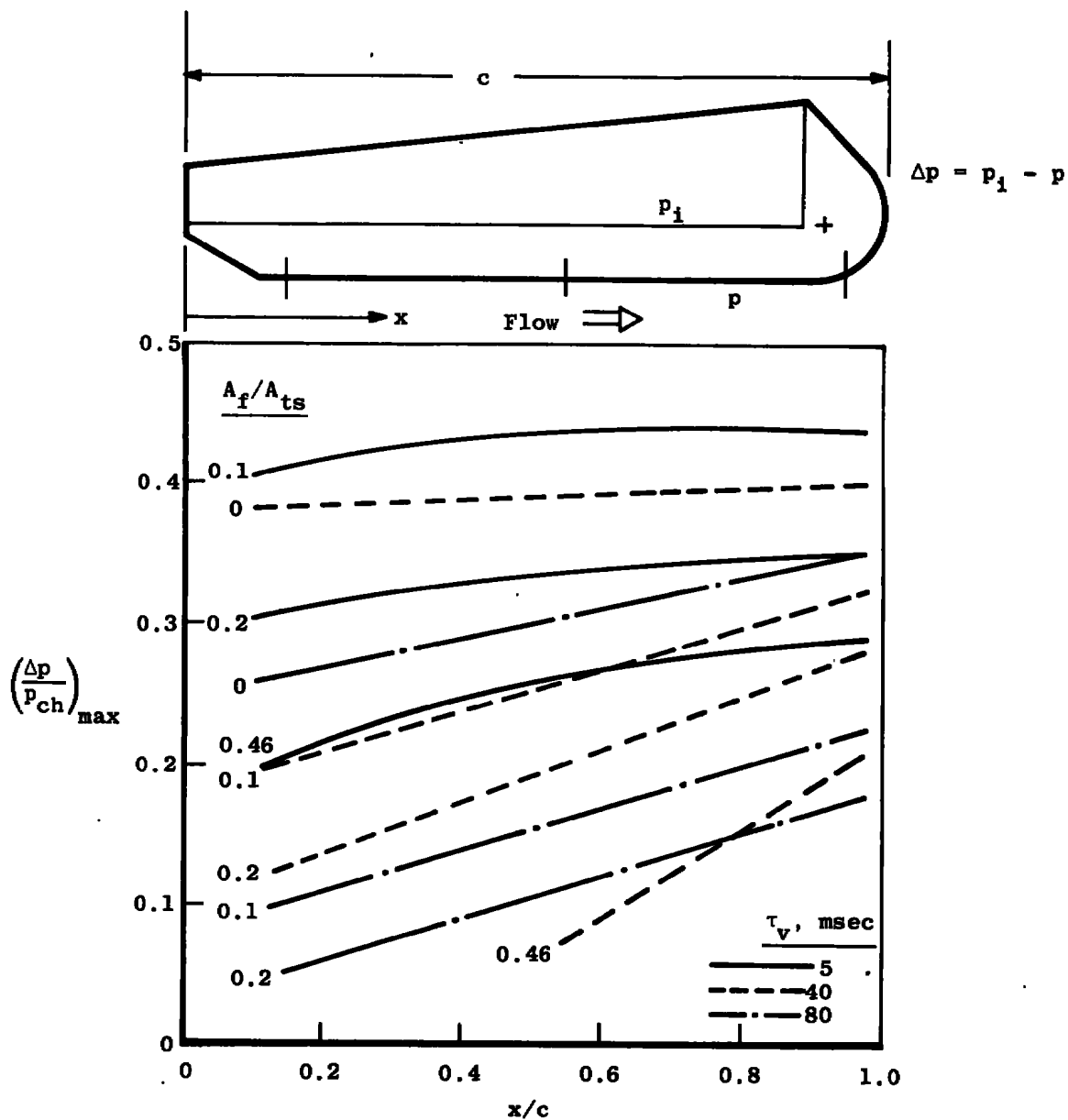


Figure 6.24. Streamwise maximum flap differential pressure coefficient during the starting process with $\tau_w = 4.5$ percent, $V_p/V_{ts} = 2.5$, and $\dot{w}_A = 0$.

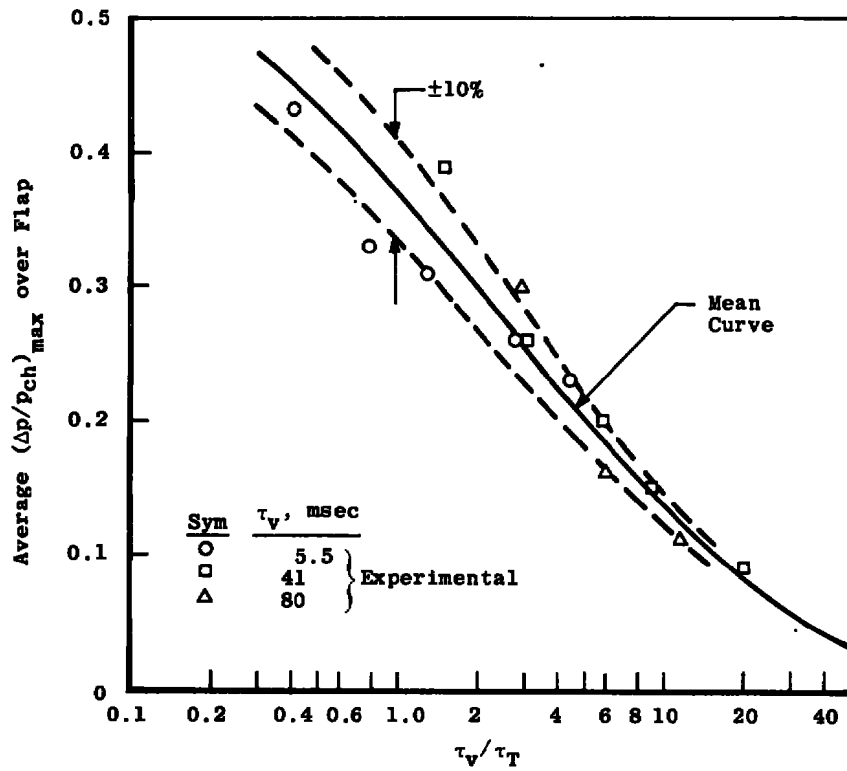


Figure 6.25. $(\Delta p/p_{ch})_{max}$ averaged over flap length as a function of τ_v/τ_T .

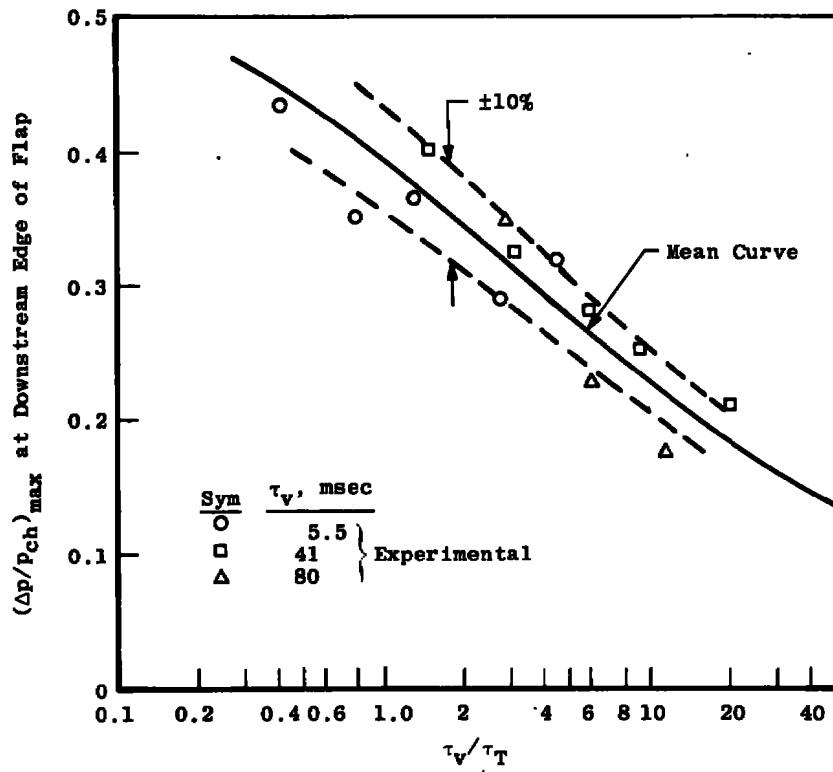


Figure 6.26. $(\Delta p/p_{ch})_{max}$ at downstream edge of flap as a function of τ_v/τ_T .

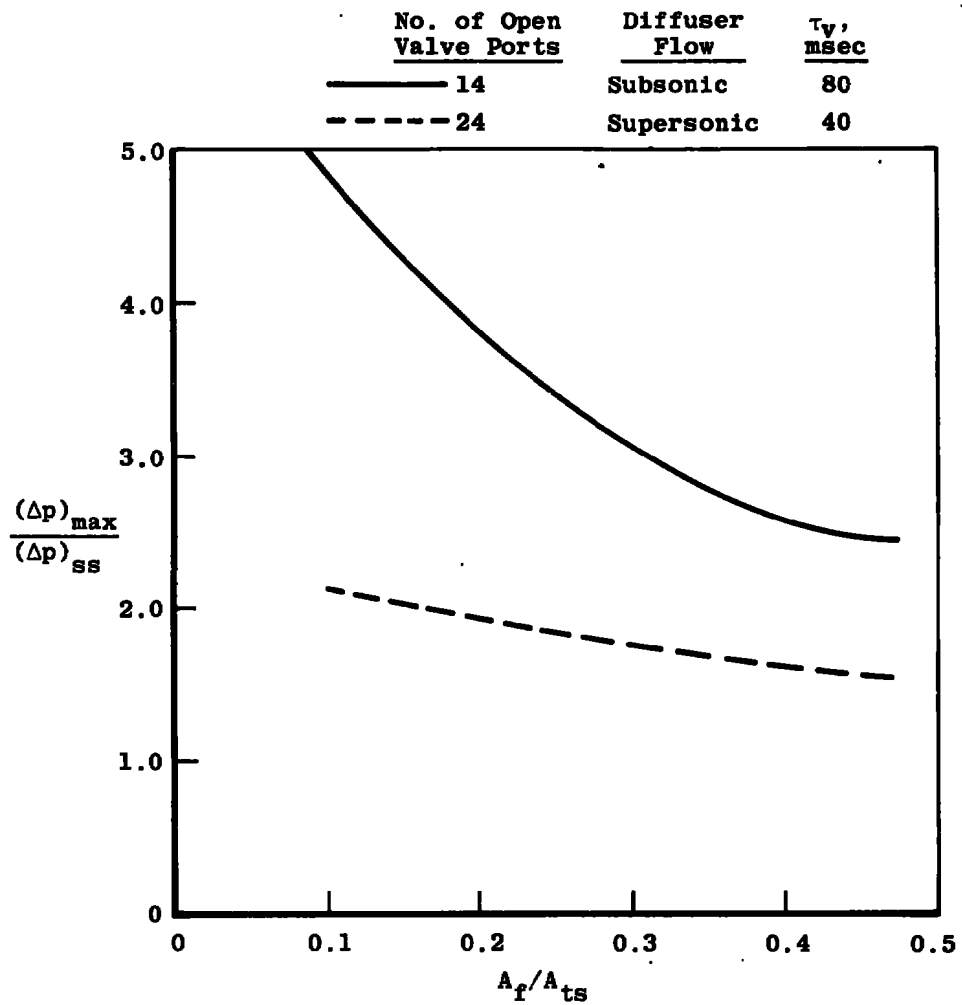
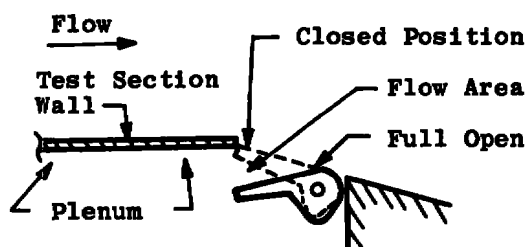
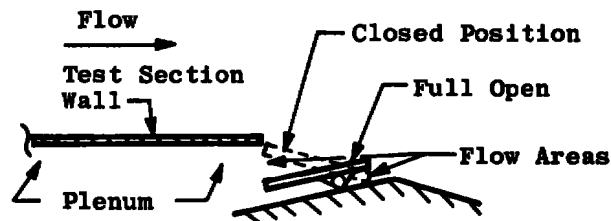


Figure 6.27. Ratio of maximum flap load to steady-state flap load as a function of A_f / A_{ts} for two cases of diffuser flow in pilot HIRT.



Pilot HIRT



A Proposed HIRT Configuration

Figure 6.28. Schematic of ejector flaps for pilot and envisioned full-scale HIRT showing geometric differences.

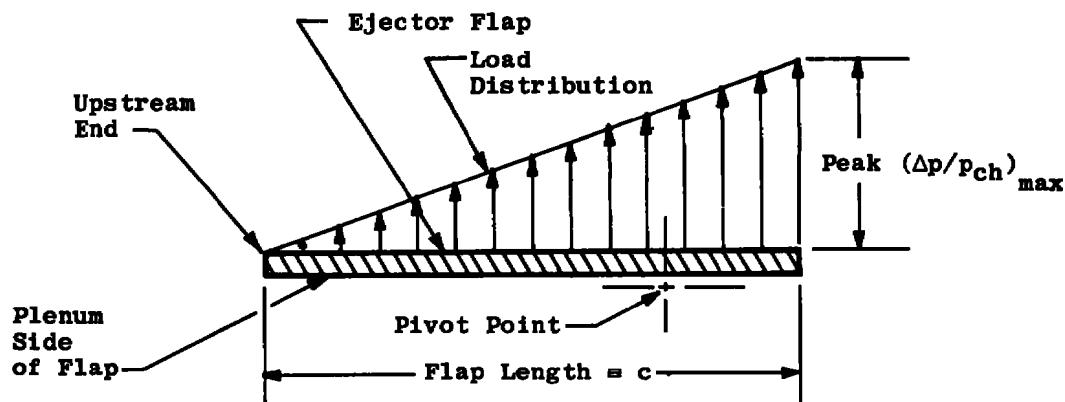


Figure 6.29. HIRT ejector flap load distribution for flap in full open position during starting process for pivot point as shown.

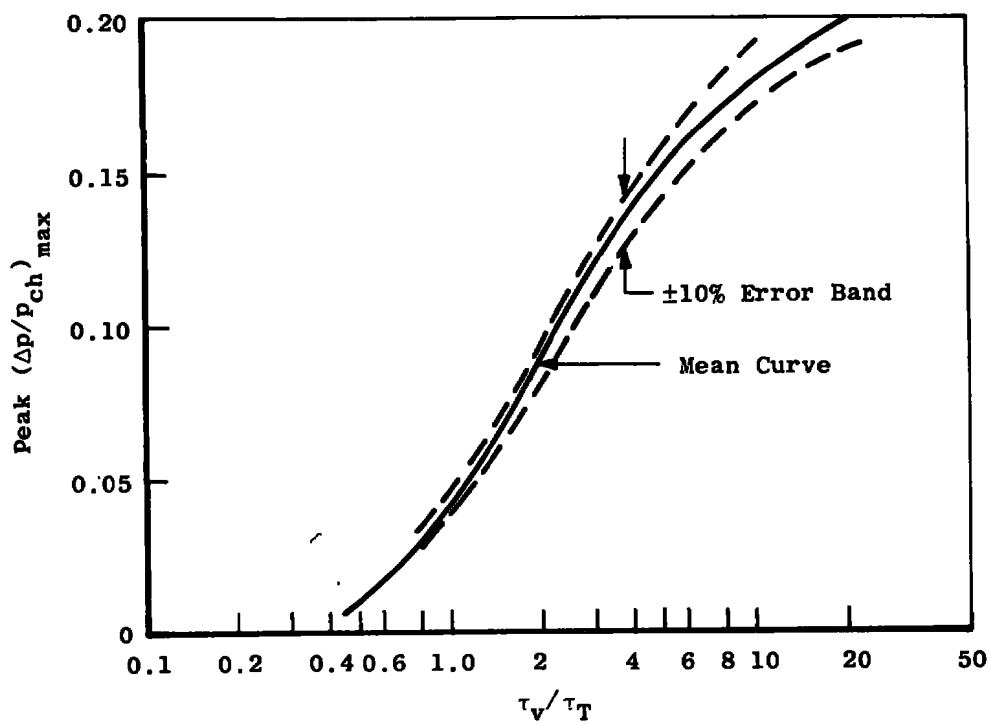
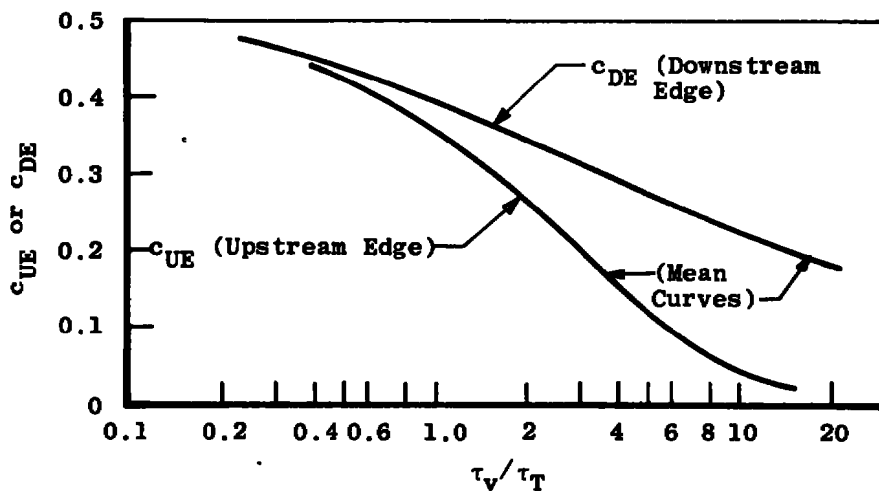


Figure 6.30. Peak $(\Delta p/p_{ch})_{\max}$ for HIRT with distribution as given in Fig. 6.29 for $A_f/A_{ts} > 0.25$.



a. Upstream and downstream pressure coefficient factor for a full-scale HIRT flap configuration versus τ_v/τ_T as illustrated in Fig. 6.28.

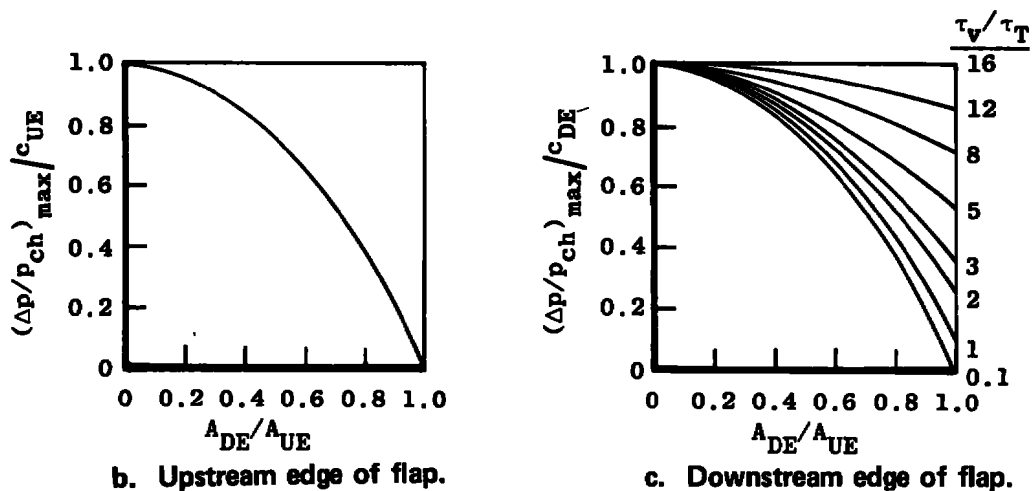


Figure 6.31. Maximum pressure coefficient distribution at the upstream and downstream edge of a typical HIRT flap configuration as a function of A_{DE}/A_{UE} .

7.0 DIFFUSER PERFORMANCE

7.1 EXPERIMENTAL PROCEDURE AND RESULTS

The start valves and plenum exhaust valves represent a significant proportion (about 15 percent) of the estimated cost of the components of a typical HIRT wind tunnel, so it is important that the required valve areas be specified precisely. Moreover, if too little valve area is provided, the operating range of the facility will be restricted until costly modifications and additional proof testing could be done. As a result, some conservatism in the valve area specification is justified and necessary to compensate for uncertainties in any engineering estimates. Aside from the definition of a valve flow coefficient, the main problem involved in sizing the start valves is in establishing the stagnation pressure at the valve intake for typical HIRT operating conditions. This requires a thorough understanding of the flow characteristics of the diffuser as constrained by the test section, ejector flap, model support, and main valve flow. Thus, an experimental program was undertaken in Pilot HIRT to assess these constraints on the diffuser flow.

Figure 7.1 illustrates the Pilot HIRT start valve and diffuser system showing the location of wall static pressure tapes in the diffuser and the total-pressure probe in the valve manifold. The diffuser consists of a rectangular-to-circular transition piece followed by a conical section ending at the manifold entrance. The valve manifold, as depicted in Fig. 7.1, is cylindrical in shape with 27 equally spaced, circumferentially positioned ports.

In order to examine the effects of the main valve on the diffuser flow, the valve discharge area was varied. By opening or closing a number of the 27 ports located on the valve manifold (see Fig. 7.1), the valve discharge area ratio, A_d/A_e , where A_d is the port area and A_e is the diffuser exit area, could be varied from 0 to 0.945.

The influence of the test section and ejector flaps on the behavior of the diffuser flow was shown by varying the auxiliary suction, \dot{w}_A , through the plenum exhaust system and by changing the ejector flap suction through a change in the flap opening, δ_f (see Fig. 7.2). A complete evaluation of the operating envelope of the diffuser required the addition of a sector and sting during the experimental program.

Figure 7.2 is a sketch of the nominal location and geometry of the sector installed in the Pilot HIRT showing the relative location of the ejector flaps. Figure 7.3 is a view of the sector and sting installed in the diffuser section of the Pilot HIRT. In addition, measurements were taken with the sting at pitch angles, α_s , of 0 and 12 deg to determine the influence of sting pitch on the diffuser flow. The cross-sectional area distribution of the diffuser section of Pilot HIRT is given in Fig. 7.4 as a function of position showing the influence of the addition of the sector.

Figure 7.5 is a plot of the static pressure distribution along the diffuser wall with the sector installed and with no auxiliary or ejector flap pumping and shows the effect of changing the discharge area ratio as reflected in the change in N where N is the number of open ports on the valve manifold. Also included in Fig. 7.5 are the total pressures measured in the end of the manifold (Fig. 7.1) for each run. As can be seen, a distinct correlation exists between the number of open ports and the character of the diffuser flow. For increasing N from 11 to 20, with reference to Fig. 7.5, the shock-like structure occurring in the vicinity of static tap number one becomes gradually more pronounced. This is due primarily to the fact that as the discharge area is increased (N increasing) the total pressure at the valve manifold must decrease in order to hold constant Mach number in the test section for a constant sonic area. As a result, the flow in the diffuser becomes progressively more supersonic. This fact is further confirmed by noting the significant loss in total pressure, as given by the difference in test section total pressure and end of manifold total pressure, occurring over the diffuser length and by comparing the total pressure losses as the number of ports, N , is increased. No significant change in the test section Mach number M_∞ , was observed for N values greater than 12.

Thus, it may be inferred that for small N , the diffuser is subsonic in character with the test section Mach number directly influenced by the port open area (directly related to N). As N is increased, a value is reached where the flow near the upstream end of the diffuser chokes. Further increase in the port open area beyond this value does not influence the test section Mach number since the flow control point has been shifted from the valve ports to the sonic throat area. An increase in N beyond this critical value mainly causes the diffuser flow to become supersonic to satisfy the imposed total-pressure loss.

The influence of the sector and sting on the diffuser flow field is illustrated in Fig. 7.6 with flaps open at a setting of $\delta_f = 0.2$ in. A comparison of Figs. 7.6a and 7.6b reveals some local sector influence

on the diffuser flow field for N values between 14 and 17. Little influence of the sector is observed for N values less than or equal to 14 and greater than 17. Diffuser performance, as reflected in the ratio p_{t_0}/p_{t_d} , is seen to be relatively insensitive to the presence of the sector for the values of N examined. Results for a sting pitch angle of 12 deg are presented in Fig. 7.6c for open port numbers of 13, 14 and 20. A comparison of this and Figs. 7.6c and 7.6b indicates no effect of sting pitch angle on the diffuser flow for comparable N values for an ejector flap opening of 0.2 in.

Pressure distributions are presented in Fig. 7.7 for flaps open at a setting of $\delta_f = 0.4$ in. revealing similar trends as observed for the $\delta_f = 0.2$ -in. case. A comparison of Figs. 7.7a and 7.7b with Figs. 7.6a and 7.6b for N increasing from 14 to 20 does indicate, however, that the presence of the sector tends to reduce the effectiveness of ejector flap pumping in establishing a test section Mach number, M_∞ . Moreover, the reduction in effectiveness is increased as the number of ports, N , is increased.

The effect of auxiliary suction on the diffuser flow distribution is given in Fig. 7.8 for the cases of sector installed and removed with N fixed at 14. Figure 7.8a clearly shows that large variations in auxiliary flow result in a diffuser flow field variation of the same order as those produced by changes in ejector flap pumping (see Figs. 7.6b and 7.7b). The diffuser flow field is shown in Fig. 7.8b for the sector removed indicating a trend similar to Fig. 7.8a for the sector installed. However, with the sector removed, the diffuser flow is slightly more supersonic for a given N . Even though the resulting test section Mach numbers for the sector installed and removed cases are comparable for a given auxiliary mass flow, the pressure distributions, locally, (around $x = 15$ in.) deviate from one another as auxiliary mass flow is increased.

In order to clarify the parameters of importance in determining diffuser performance, the variation of discharge total pressure, diffuser exit, and plenum static pressure are given in Figs. 7.9a and 7.9b as a function of the number of open ports, N , and flap opening, δ_f . As can be seen, as N is increased the discharge total pressure, p_{t_d} , and diffuser exit static pressure, p_e , decrease monotonically. The plenum pressure, p_c , on the other hand, decreases with increasing N until a critical value, N_{crit} , is reached. For N values greater than N_{crit} the plenum pressure and, hence, the Mach number, M_∞ , for constant free-stream total pressure, p_{t_∞} , remains constant. A comparison of Figs. 7.9b with

7.9a indicates a negligible effect of the flap setting, for the two conditions compared, on the variation of p_{td} and p_e with N . With reference to Fig. 7.9b, the plenum pressure, however, decreases to a lower value of pressure (and free-stream Mach number for fixed $p_{t\infty}$) resulting in a higher N_{crit} as compared to the case for $\delta_f = 0.2$ -in. (Fig. 7.9a).

The influence of the sector on diffuser performance is shown in Figs. 7.10a and 7.10b as a function of the number of open ports, N , for $\delta_f = 0.2$ and 0.4 in., respectively. An examination of the manifold discharge pressure for the diffuser empty case as compared to the sector installed case shows negligible difference for N near 14 and a difference of almost five percent as N approaches 20. The effect of sting pitch angle is also included in Fig. 7.10a indicating little measurable difference for the data at angles of 0 and 12 deg. The variation in plenum pressure as a function of N is also included in Figs. 7.10a and 7.10b verifying the fact that, as N increases, the difference in plenum pressure for the sector installed and removed cases increases and approaches a constant difference. Moreover, this constant difference in plenum pressure for large N increases as the flap setting, δ_f , is increased. Diffuser exit pressure, p_e , is given in Figs. 7.10a and 7.10b showing no influence of the sector installed compared to the removed configuration, sting pitch angle or flap opening on the variation with N .

Some general trends have been inferred from the data presented and are given in Fig. 7.11. As indicated earlier, as the flap setting is increased, the value of N_{crit} and of the maximum test section Mach number for $N \geq N_{crit}$ with no auxiliary pumping, $M_{\infty max}$, increases. The effect of the sector on N_{crit} and $M_{\infty max}$ is also included showing little effect on the value of N_{crit} and increased importance for $M_{\infty max}$ as the ejector flaps are opened.

The total-pressure loss through the diffuser system as influenced by auxiliary suction, flap setting, and number of open ports on the manifold versus the free-stream Mach number, M_{∞} , is shown in Fig. 7.12. For the sector installed configuration, as the flap opening is increased at a fixed Mach number for no auxiliary suction, the total-pressure loss in the diffuser system decreases. With the application of auxiliary suction, the total-pressure ratio curves for 14 open ports on the 16-in. SSV tend to collapse at Mach numbers above 1. This trend reflects the change in the mechanism by which test section Mach number is established. By using increased ejector flap pumping (which results in a higher N_{crit} to attain higher Mach numbers) high diffuser losses, as

illustrated in a comparison of Figs. 7.10a and 7.10b, result. Implementation of auxiliary suction to attain the same higher Mach numbers causes little change in the diffuser flow (see Fig. 7.8) and, hence, smaller comparable diffuser losses. With the sector removed, the influence of ejector flap pumping on the diffuser flow is decreased, and the diffuser loss associated with the sector geometry is eliminated. This results in lower diffuser total-pressure losses but of similar trend when compared to the sector installed results.

Operationally, the test section centerline Mach number distribution would be used to determine an optimum flap setting as a function of M_∞ and porosity, τ_w . Calibration of other tunnels (Ref. 7) indicates that flap settings for Pilot HIRT should be between 0.2 and 0.4 in. Thus, diffuser overall total-pressure losses for Pilot HIRT (when flow quality is maximized) will be bounded by the curves for flap settings of $\delta_f = 0.2$ and 0.4 in.

7.2 DIFFUSER MODELING

In order to properly match the main valve and diffuser system to accommodate given flow requirements in a full-scale HIRT-type facility, the losses through each must be known precisely as a function of the aerodynamic and geometric constraints. Since the pilot tunnel results presented in the previous section considered only one geometric configuration, the pressure losses attributable to the diffuser and the valve could not be separated. Thus, the analysis presented here is intended to provide a method by which the diffuser and main valve system performances may be separately estimated.

If it may be assumed that flow properties are uniform in planes normal to the flow direction, mass conservation between any two stations in the diffuser requires that

$$f(M) A_{p_t} T_t^{-1/2} = \text{constant} \quad (7.1)$$

where $f(M) = 0.92M/(1 + 0.2M^2)^3$ for $\gamma = 1.4$ and M , A , p_t , and T_t are the local diffuser Mach number, area, total pressure, and temperature, respectively. If there is no heat transfer, the total-pressure ratio is

$$\frac{P_{t_1}}{P_{t_2}} = \frac{f(M_2) A_2}{f(M_1) A_1} = \frac{A_2/A_1}{f(M_1)/f(M_2)} \quad (7.2)$$

The Mach number function for the mass flow rate, $f(M)$, is plotted in Fig. 7.13, whereas that for the total-pressure ratio for a choked discharge, $f(M_1)/f(1)$, is plotted in Fig. 7.14 for the ranges of interest in a typical HIRT facility. Equation 7.2 shows that the ratio, (p_{t_e}/p_{t_d}) , increases directly with valve discharge area ratio, A_d/A_{ts} , for a given free-stream Mach number, M_∞ , and a critical valve discharge ($M_d = 1$). This fact is represented in Fig. 7.15 for the range of discharge areas available in the Pilot HIRT tunnel. Of course, there is a minimum total pressure at the discharge (about $14.3 \times 1.89 = 27$ psia) which is required to assure choked flow from the valve with an atmospheric discharge and this, in turn, defines the minimum free-stream total pressure required for a given downstream ducting geometry and operating conditions. This minimum total pressure, relative to the discharge static, is given in Fig. 7.16 for the same range of conditions as the total-pressure ratio in Fig. 7.15.

Since the discharge ports of the start valve system are located in the wall of the manifold duct (see Fig. 7.1), the flow leaving the diffuser must turn up to 90 deg. It is well established that an incompressible flow, when turning through an angle of 90 deg, experiences a total-pressure loss in some proportion, K_d , to the dynamic pressure of the entry flow (Ref. 10). This is given in Eq. (7.3).

$$p_{t_e} - p_{t_d} = K_d q_e \quad (7.3)$$

A value of $K_d = 1.0$ is considered representative of the magnitude appropriate to Pilot HIRT. An estimate of the losses for a onedimensional adiabatic flow in the manifold is given in Fig. 7.17 along with an estimate of the maximum Mach number at the entrance to the manifold. The manifold losses, given in the form of total-pressure ratio in the lower plot, are shown to be decreased by a reduction in discharge area, i. e., for a decrease in the ratio A_d/A_e . Moreover, a maximum loss is prescribed by the onset of choking at the entrance when the discharge is sufficiently large, i. e., $A_d \leq 1.59 A_e$. Of course, this area would change if the losses were different from those assumed for this example ($K_d = 1.0$).

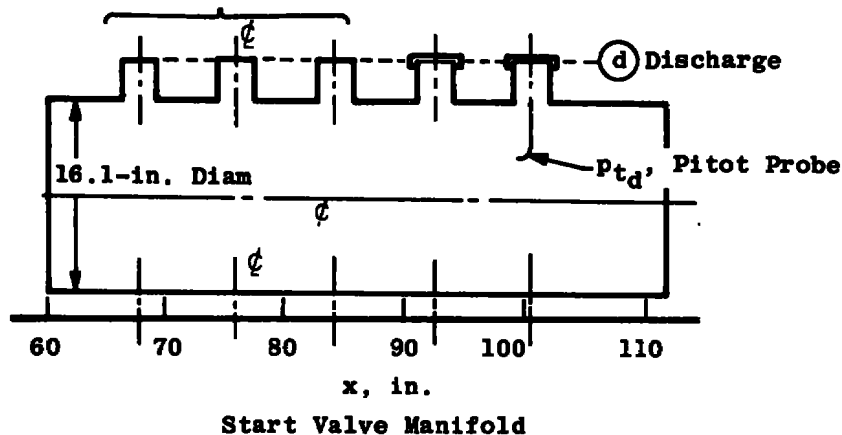
The previous estimates of the manifold entrance Mach number (with a choked discharge valve) are similarly estimates of the diffuser exit Mach number for the same losses in the manifold ducting. By specifying the inlet Mach number of the diffuser as the same as the test section, e. g., $M_\infty = 1.0$, the diffuser total-pressure ratio may be estimated for the range of discharge areas of interest at fixed diffuser

area ratios. The results of these estimates, based on the onedimensional flow assumption, are presented in Fig. 7.18 for diffuser area ratios, A_e/A_{ts} , of 1.5 and 3.0.

For the diffuser, the two curves in the upper plot of Fig. 7.18 show that losses in excess of those for a normal shock at the exit are required for the majority of the range in discharge area available with the $A_e = 1.5 A_{ts}$ diffuser system, whereas with the Pilot HIRT geometry ($A_e = 3.0 A_{ts}$) an exit normal shock can satisfy the critical total-pressure ratio requirements over most of the discharge area range, i. e., at $A_d \leq 0.93 A_{d \max}$. The estimated diffuser total-pressure ratio sets the lower limit on the possible operating range. The shaded areas in the figure therefore indicate the conditions and area ratios at which it should be possible to operate with nominally attached flows in the diffuser system and discharge ports. These estimates also show that the diffuser area ratio (A_e/A_{ts}) has a most pronounced influence on the losses across the diffuser, being the least for the smallest area ratio.

For the manifold, the two curves in the lower plot of Fig. 7.18 show that the diffuser area ratio also has a pronounced effect on its losses but in the reverse sense, being the most for the smallest area ratio. This is the result of the higher Mach numbers at the diffuser exit (manifold entrance) which yield higher losses in the 90-deg turn because of the higher dynamic pressures. It should be noted that the loss factor, K_d , which was used in these estimates was an assumed value that could have been larger. If it were larger, the manifold pressure ratios could be increased, whereas the diffuser pressure ratios would be expected to be decreased because the critical pressure ratio (Fig. 7.15) must remain fixed regardless of the distribution of losses in the diffuser system.

(Ports Shown Schematically)
 Three Stations with Nine
 Nipples Each, 40-deg Apart
 (3.0-in. Diam) Controlled by
 Sliding Sleeve



End of
 Test Section

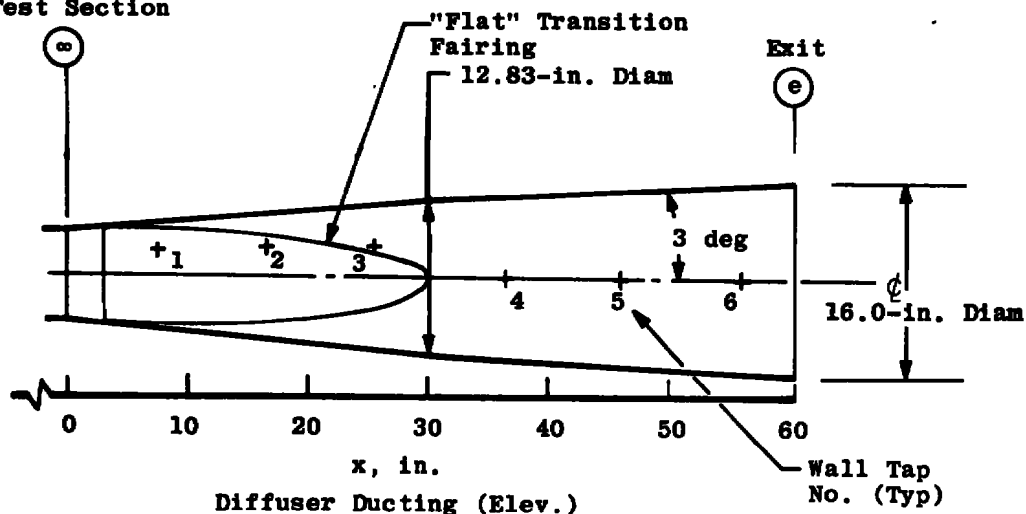


Figure 7.1. Pilot HIRT diffuser system.

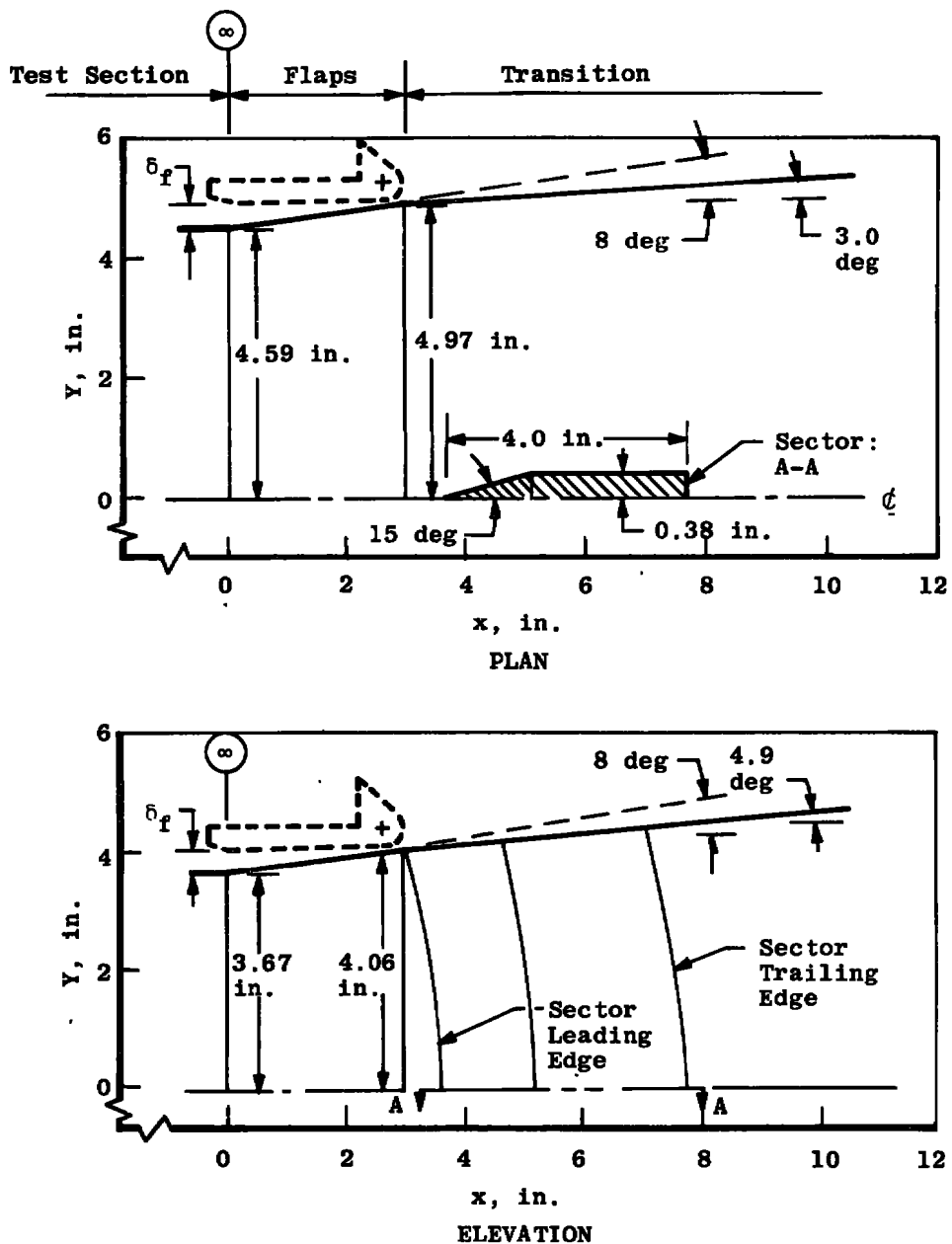


Figure 7.2. Ejector flap section of pilot HIRT.

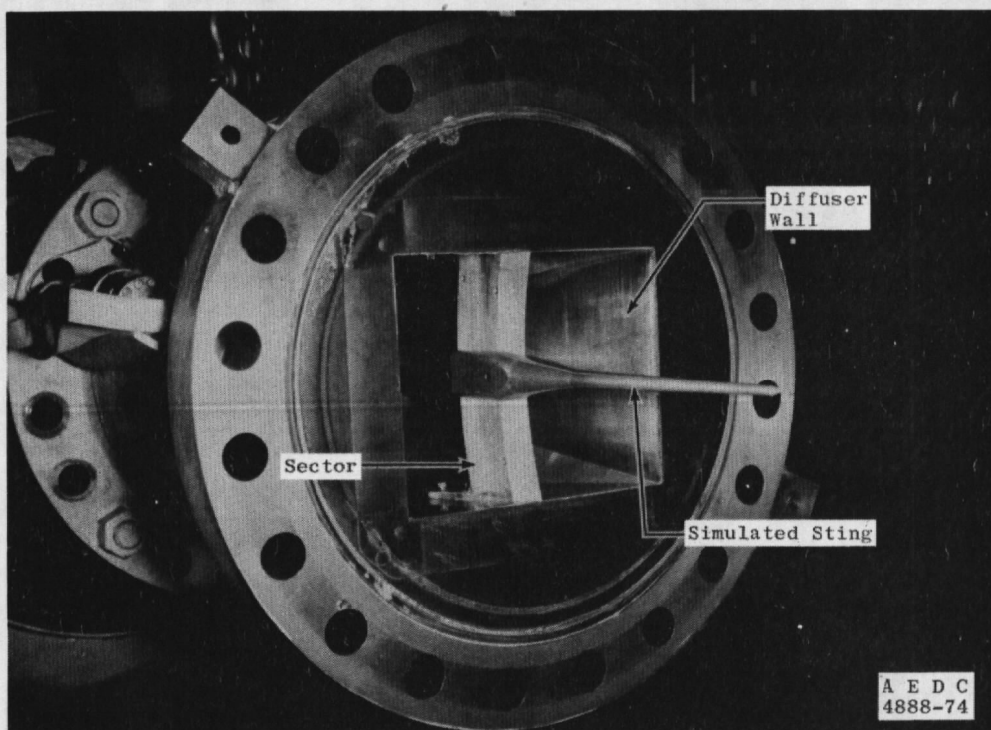


Figure 7.3 Installation view of sector in upstream end of diffuser of pilot HIRT.

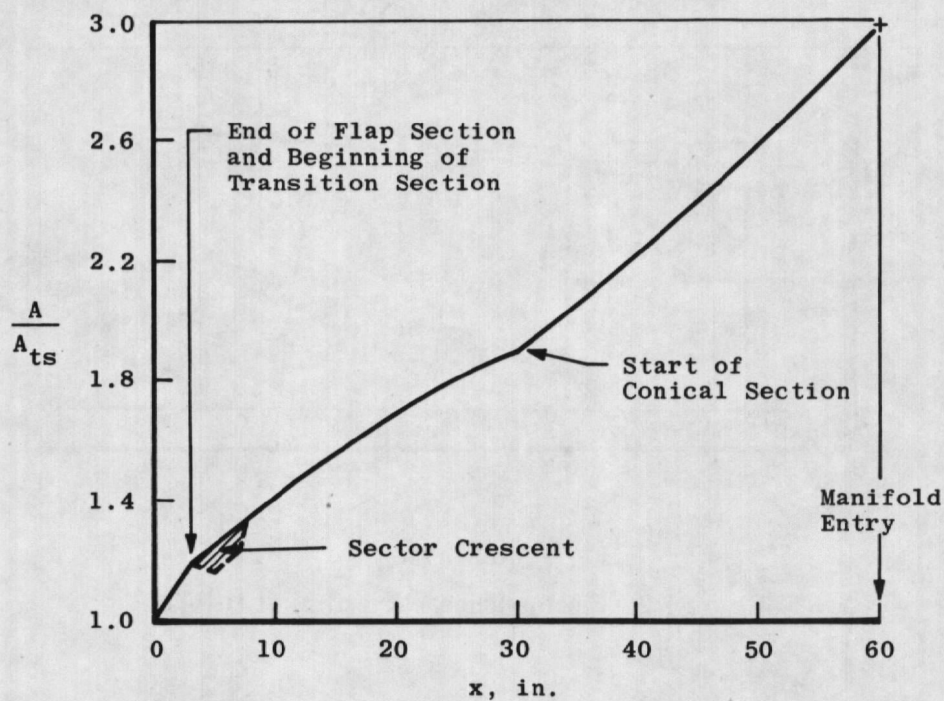


Figure 7.4. Pilot HIRT diffuser area distribution.

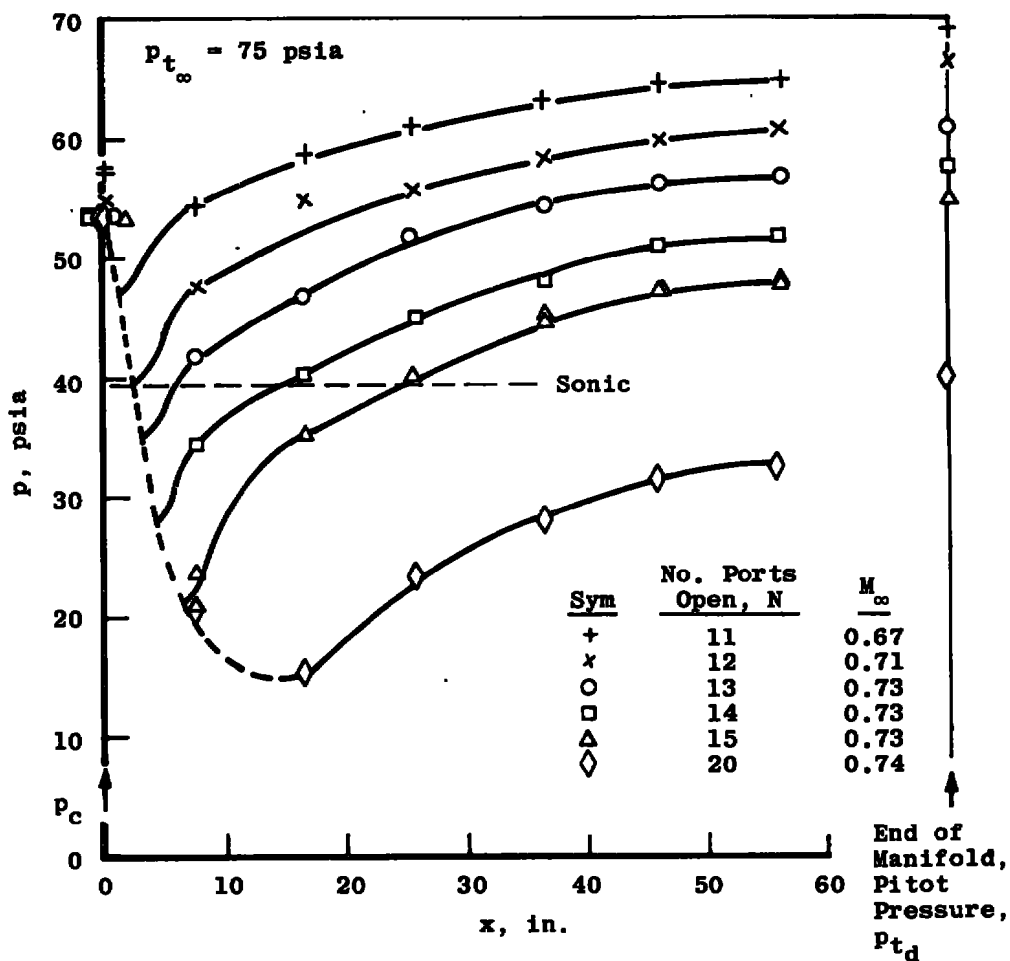


Figure 7.5. Pressure distributions for all ejector flaps closed, $t = 170 \text{ msec}$, with no auxiliary suction, sector installed ($\alpha_s = 0$).

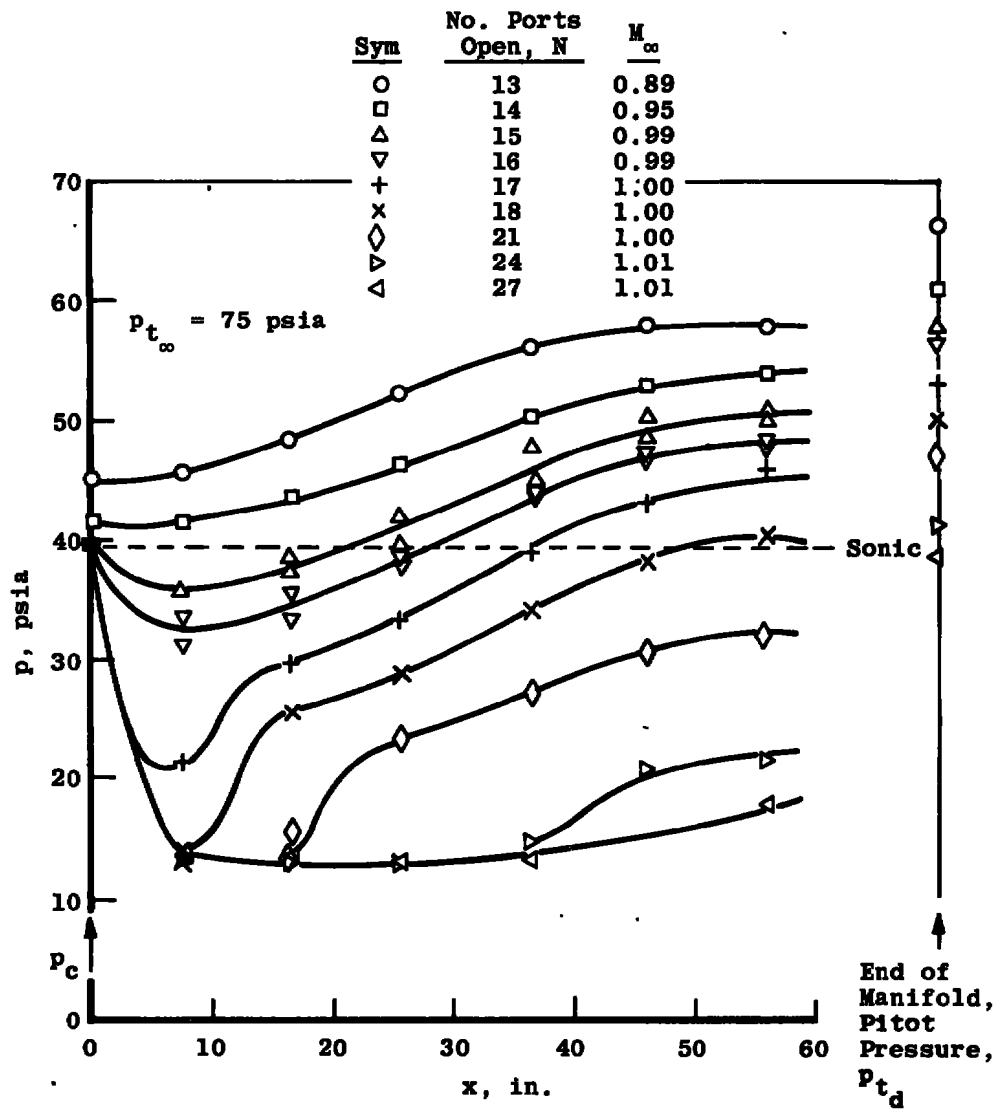
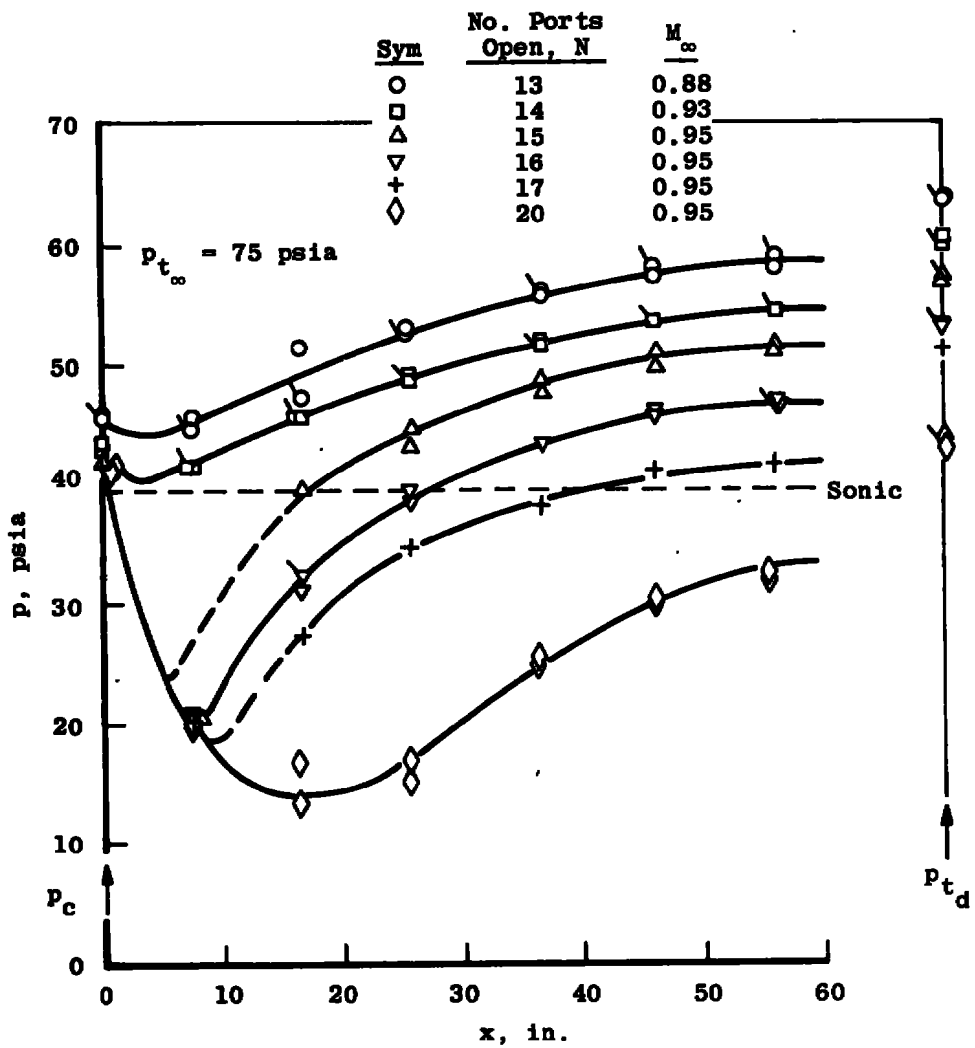
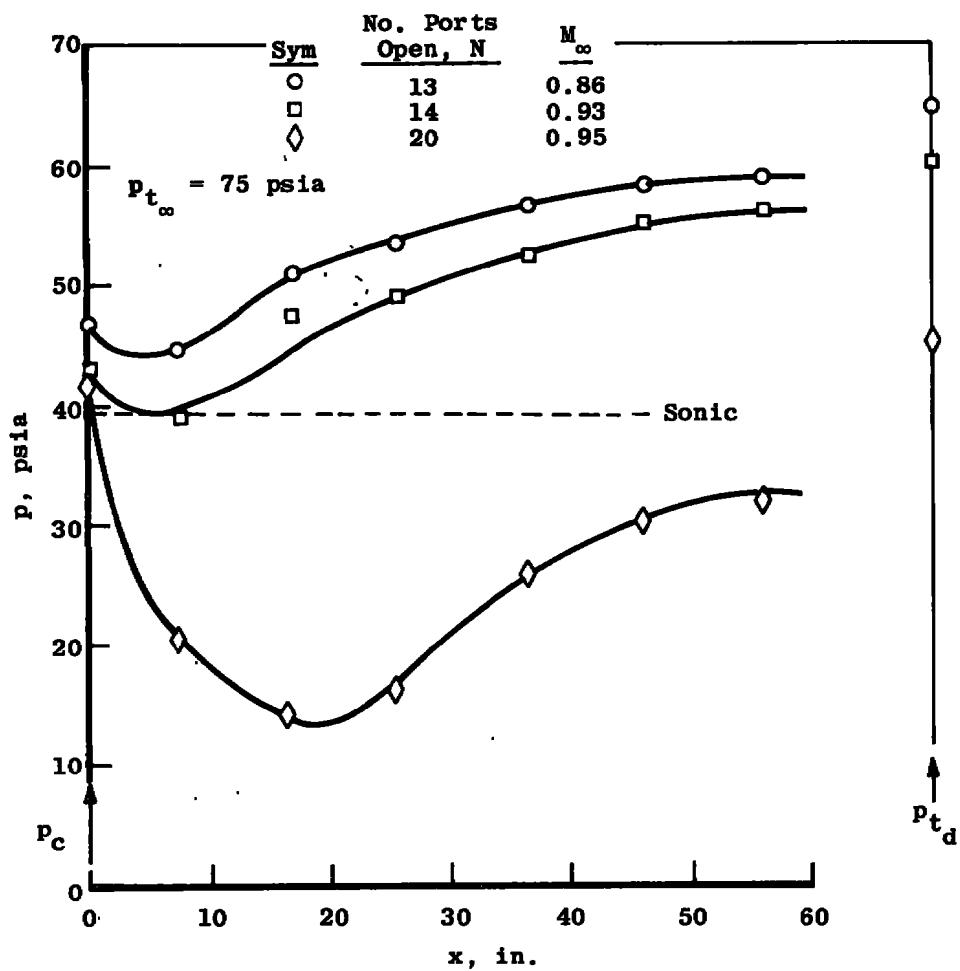


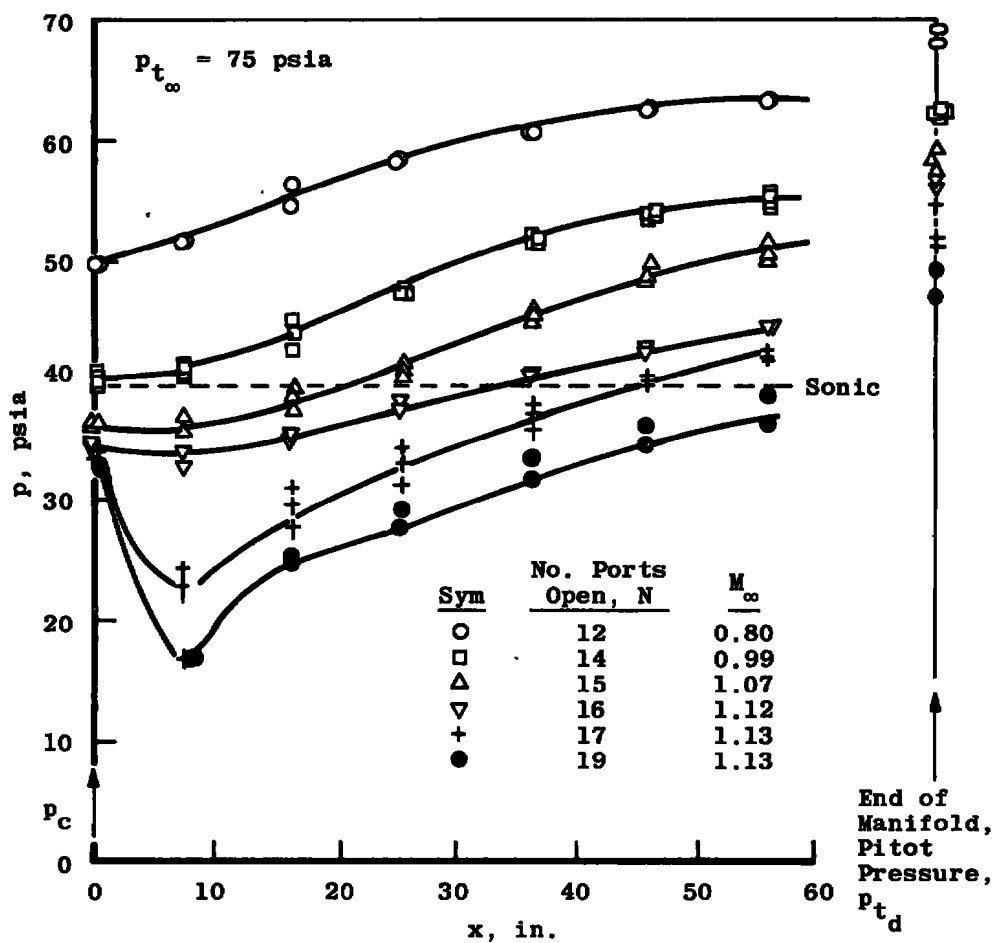
Figure 7.6. Pressure distributions for all ejector flaps open 0.2 in., $t = 170$ msec, with no auxiliary suction.



b. Sector installed at $\alpha_s = 0$
Figure 7.6. Continued.

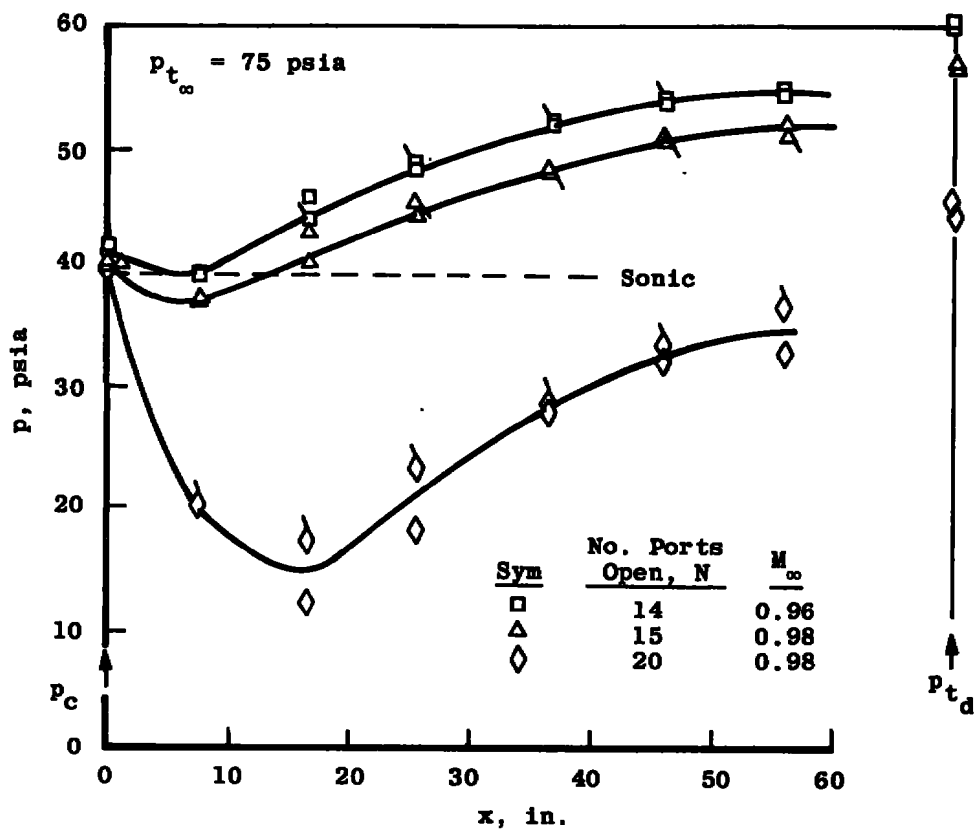


c. Sector installed at $\alpha_s = 12^\circ$.
Figure 7.6. Concluded.

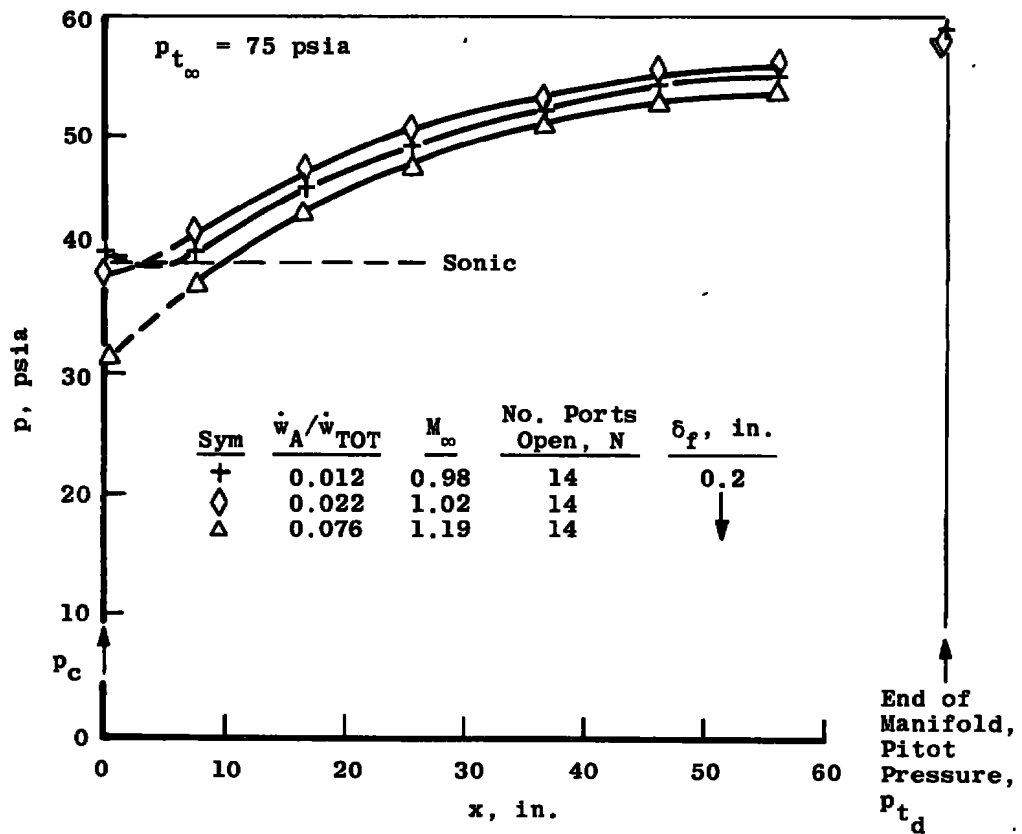


a. Sector removed

Figure 7.7. Pressure distributions for all ejector flaps open 0.4 in., $t = 170 \text{ msec}$, with no auxiliary suction.

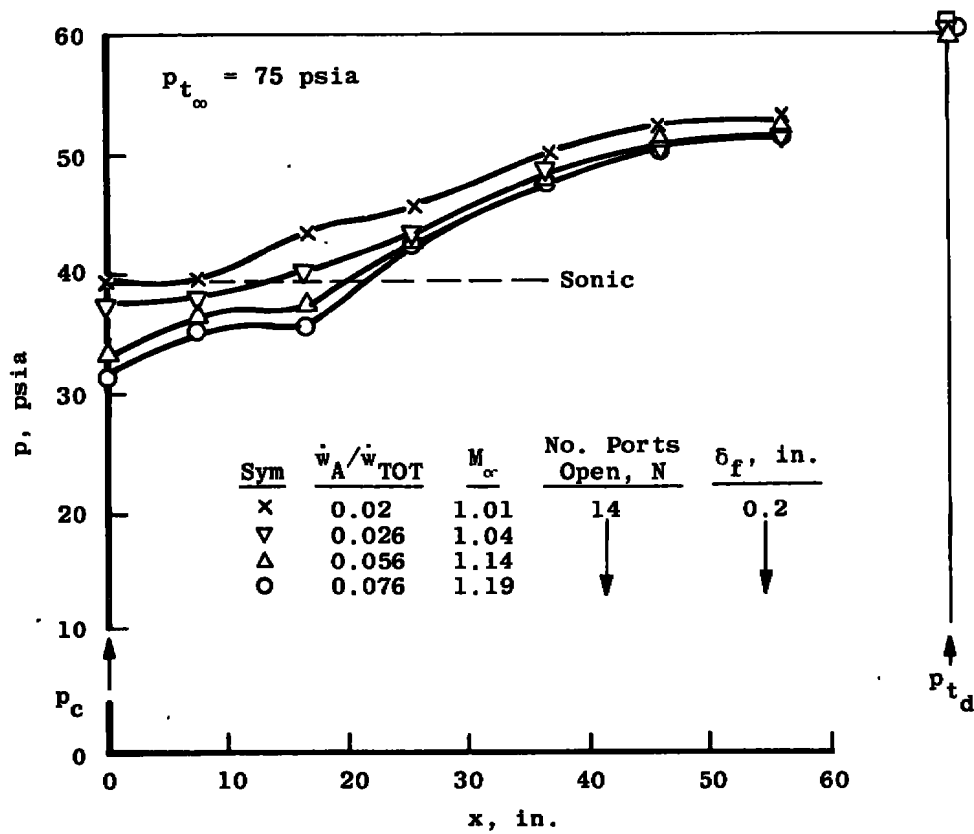


b. Sector installed at $\alpha_s = 0$
Figure 7.7. Concluded.

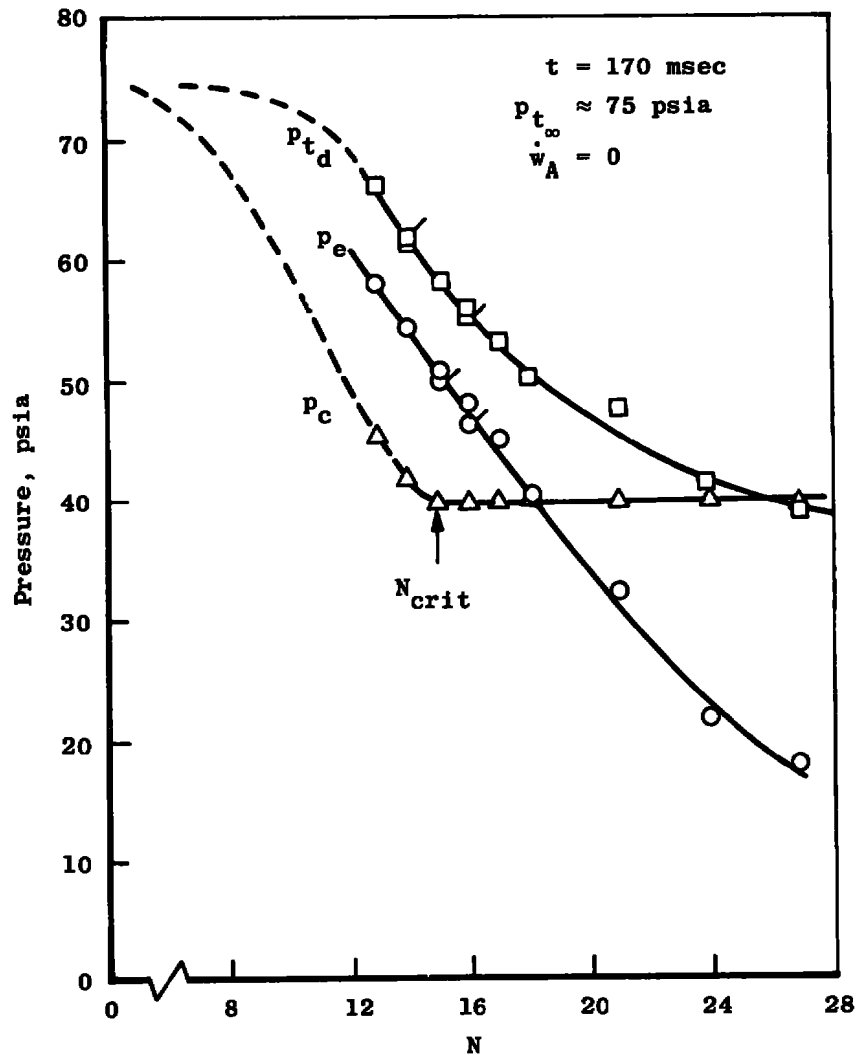


a. Sector installed, $\alpha_s = 0$

Figure 7.8 Pressure distributions for all ejector flaps open, $t = 170 \text{ msec}$, with auxiliary suction.

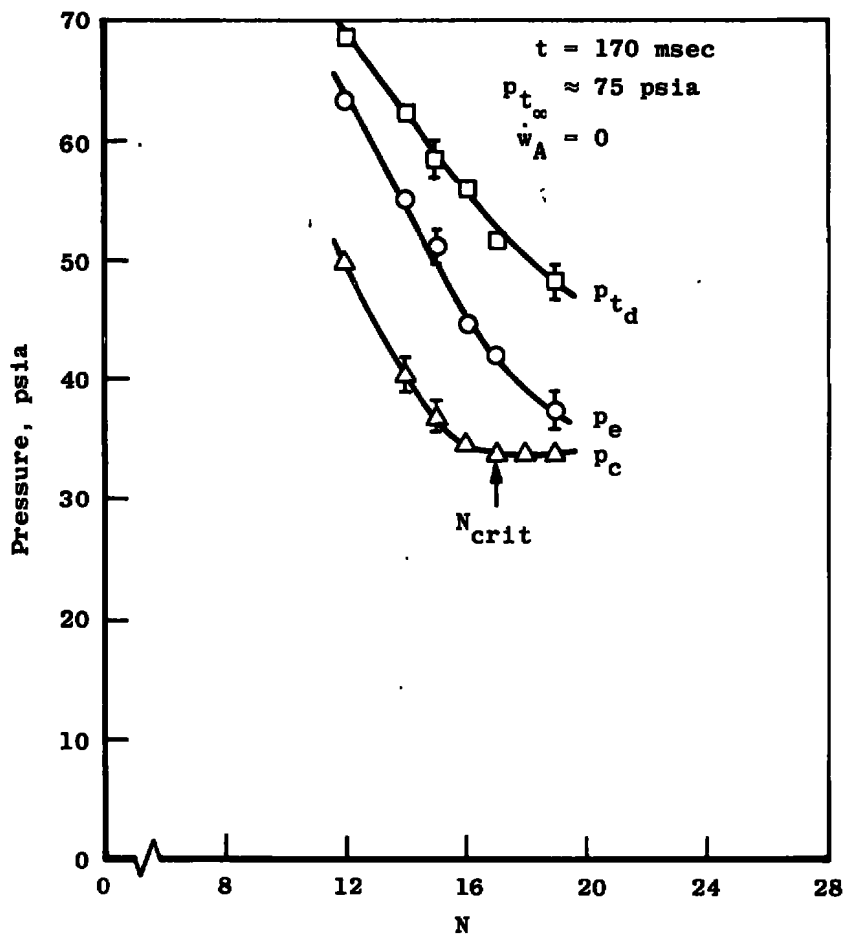


b. Sector removed
Figure 7.8. Concluded.

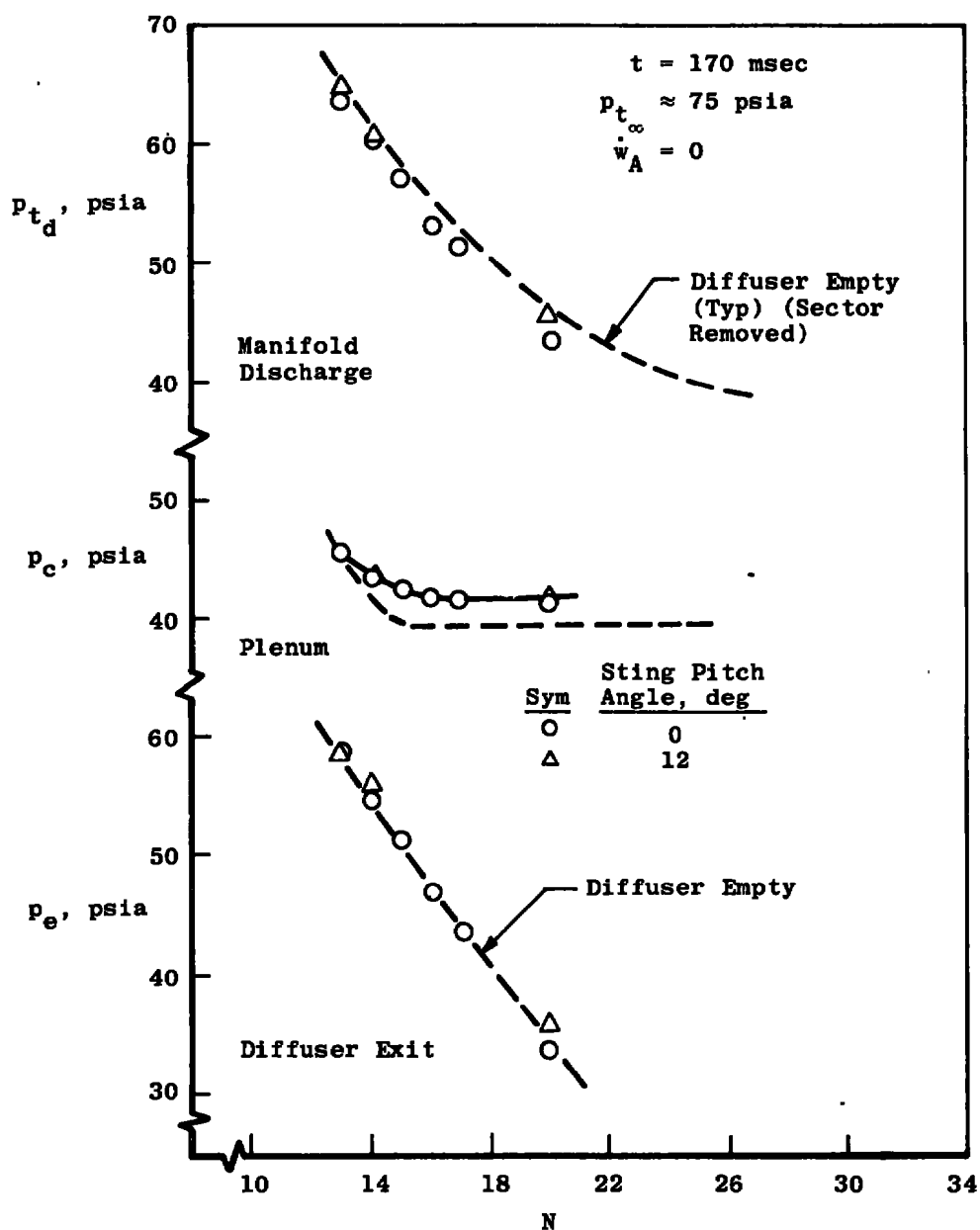


a. Flaps open 0.2 in.

Figure 7.9. Influence of number of ports opened on pressures in pilot HIRT diffuser with sector removed.

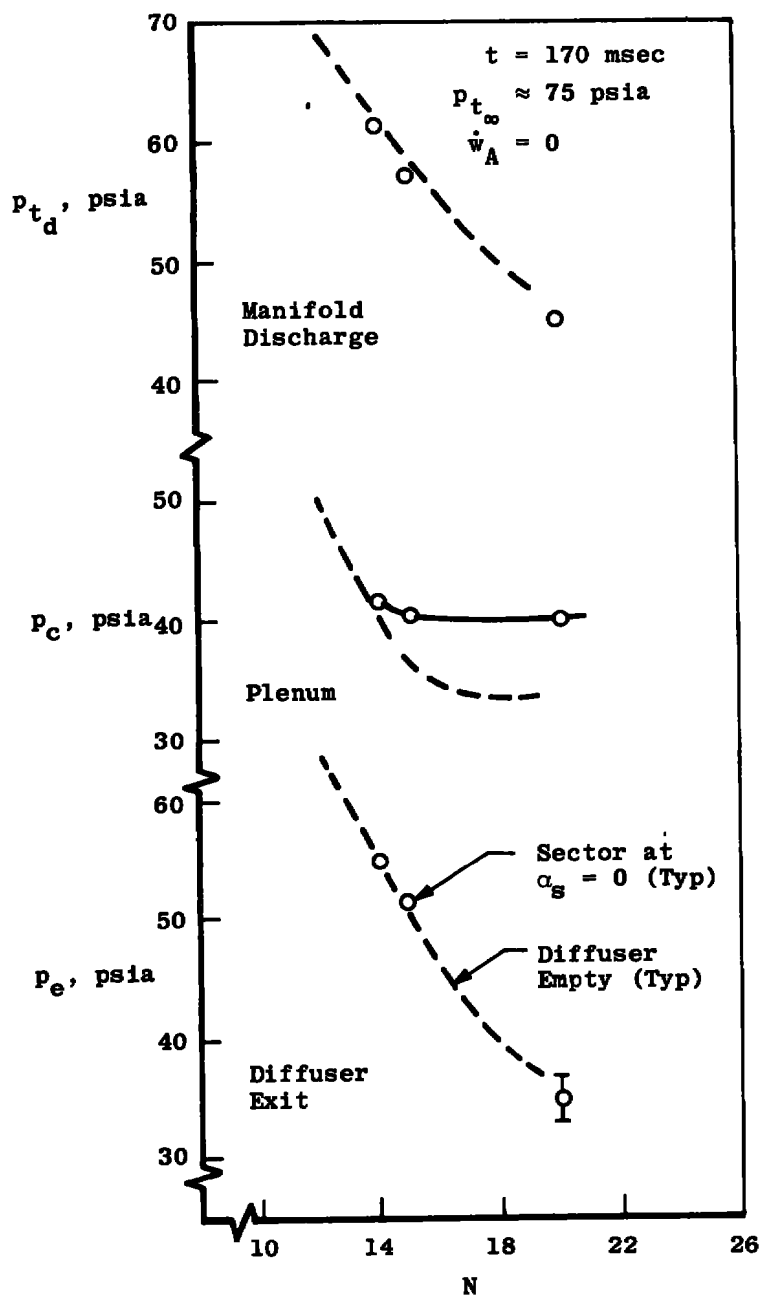


b. Flaps open 0.4 in.
Figure 7.9 Concluded.



a. Flaps open 0.2 in.

Figure 7.10. Influence of sector on diffuser pressures.



b. Flaps open 0.4 in.
 Figure 7.10. Concluded.

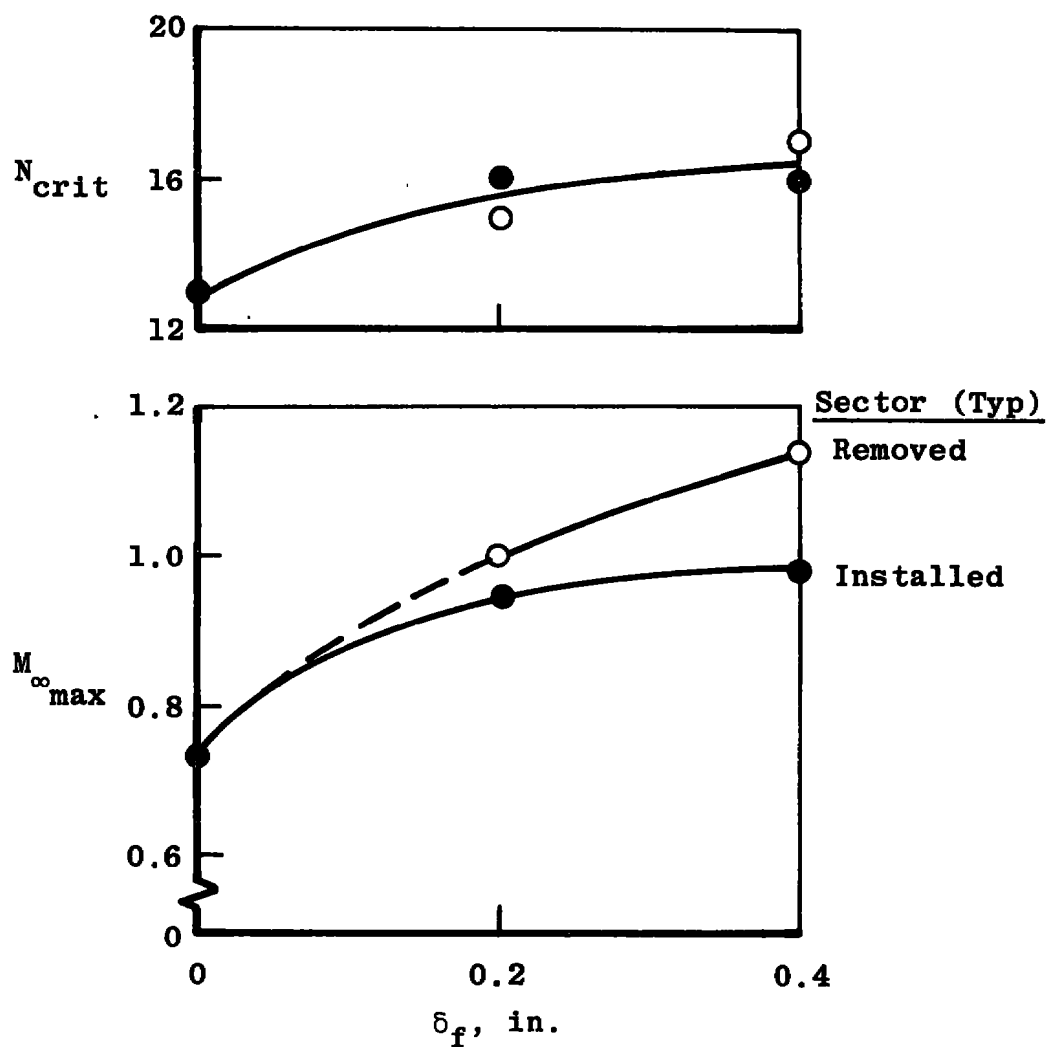


Figure 7.11. Effect of ejector flap opening on operating conditions in plenum and manifold without auxiliary suction, $t = 170$ msec, $p_{t_{\infty}} = 75$ psia.

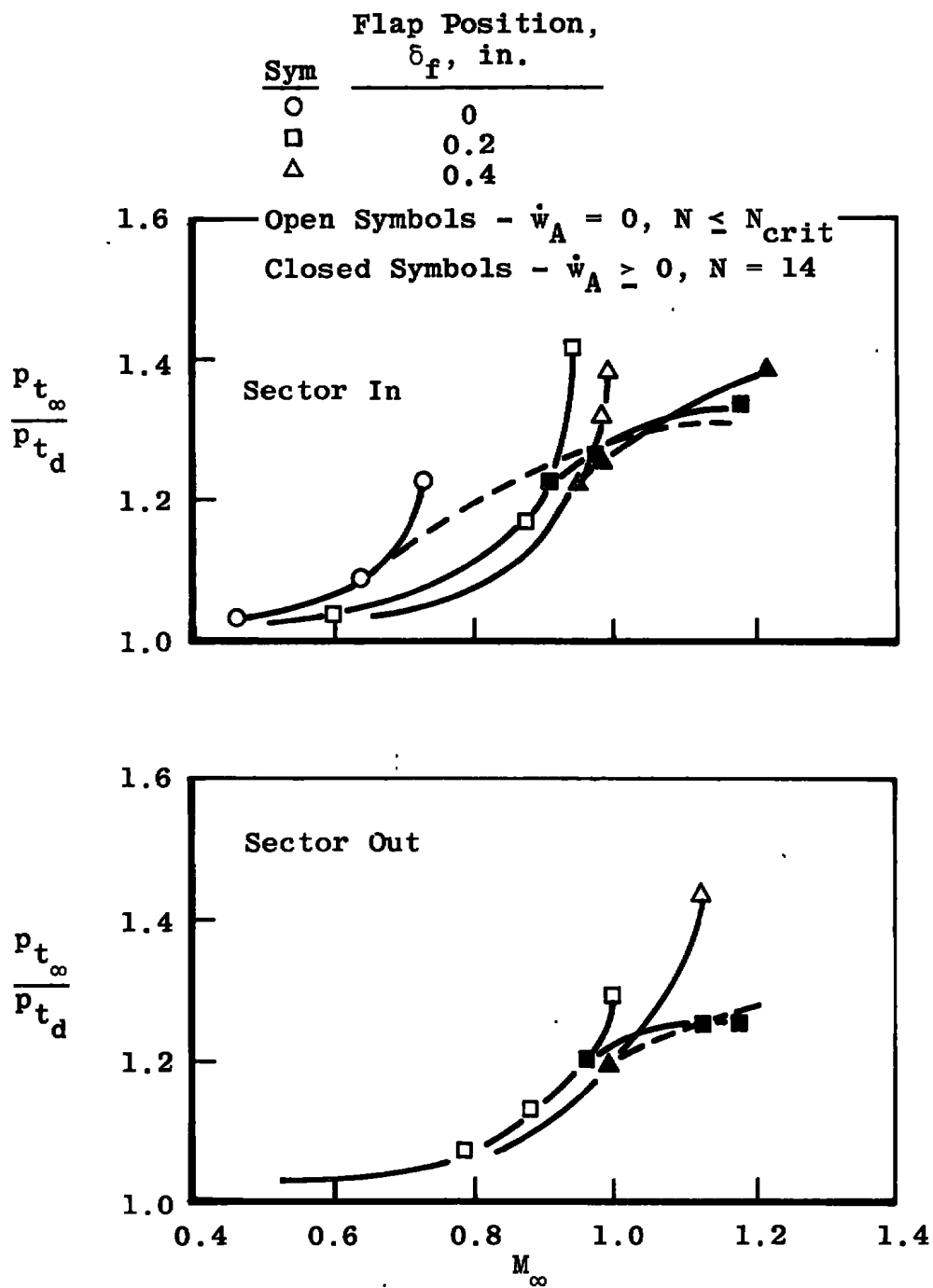


Figure 7.12. Effects of sector and auxiliary suction on overall total-pressure ratio, $t = 170$ msec, $p_{t_\infty} = 75$ psia.

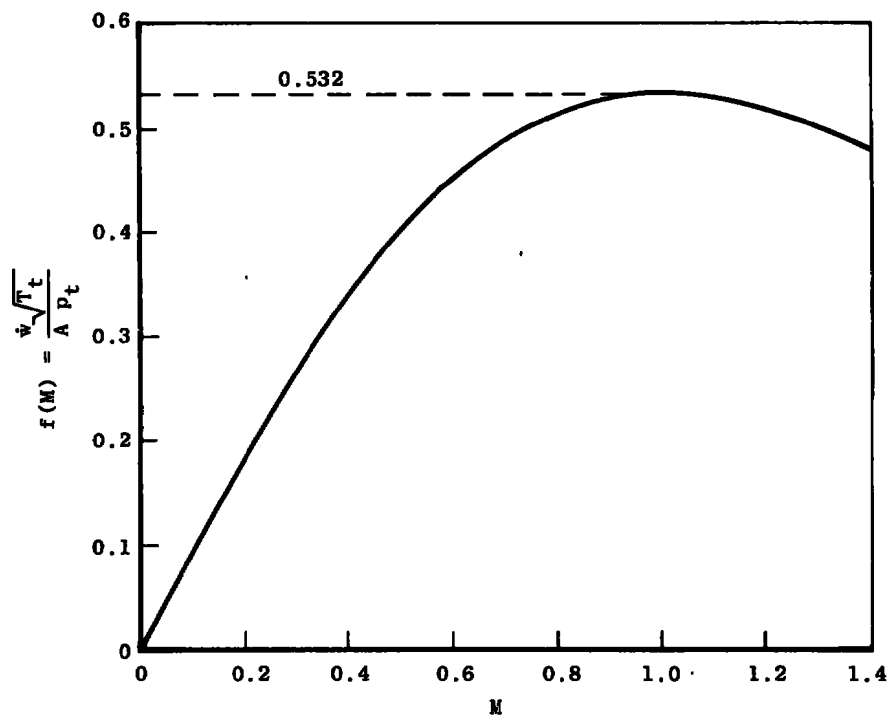


Figure 7.13. Mach number function in mass flow equation for uniform flow.

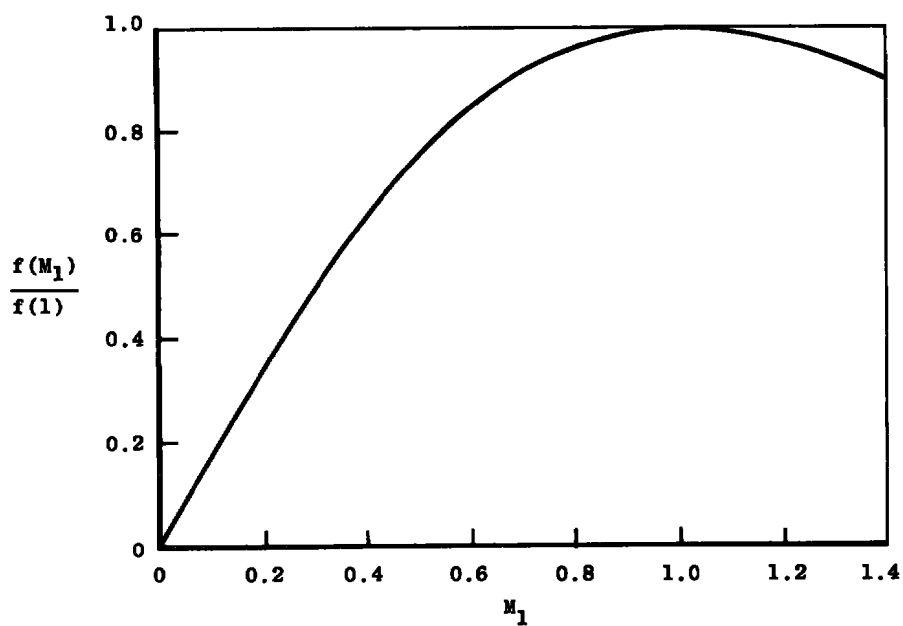


Figure 7.14. Mach number function for total-pressure ratio with choked flow.

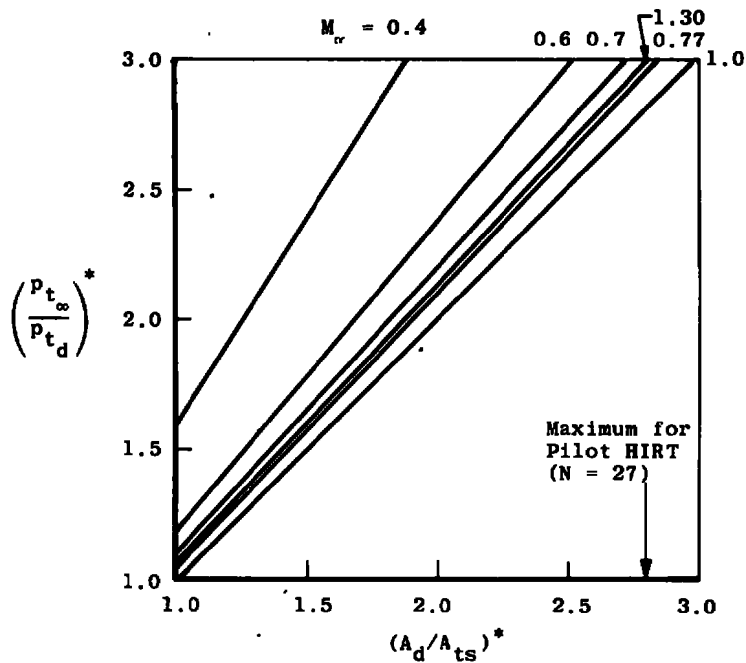


Figure 7.15. Critical total-pressure ratio providing a choked flow at the discharge ($M_d = 1$).

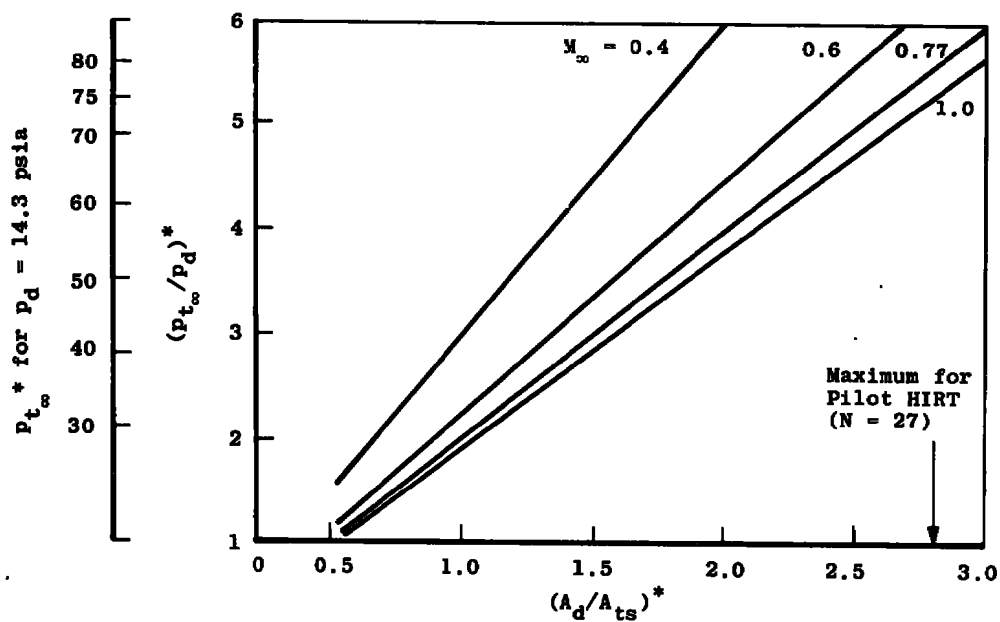


Figure 7.16. Critical or minimum stagnation pressure required to choke at discharge area.

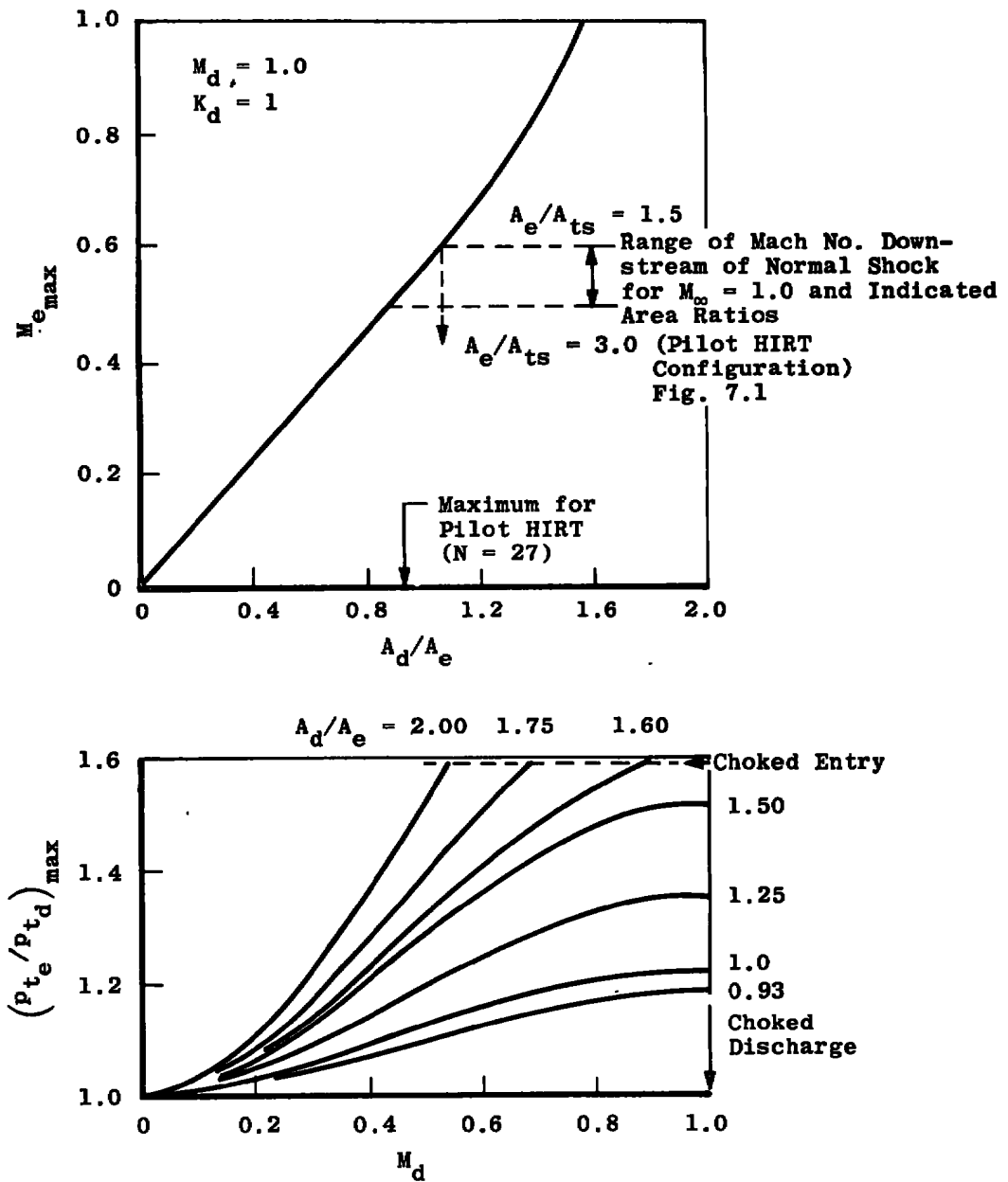


Figure 7.17. Maximum pressure ratio and entrance Mach number for valve manifold with flow-turning losses.

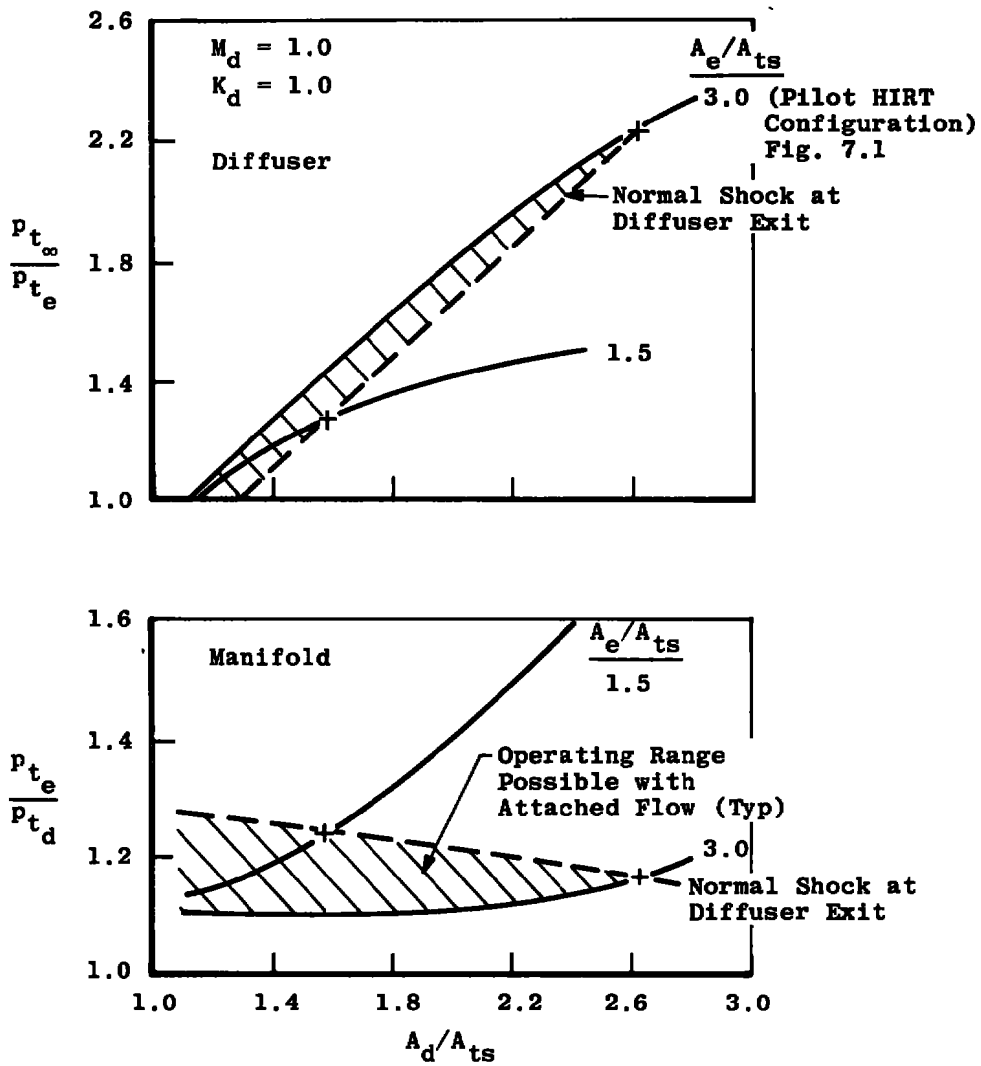


Figure 7.18. Estimated losses in diffuser system for range of discharge areas at $M_{\infty} = 1.0$.

8.0 CONCLUDING REMARKS

This report has presented the results of continued studies into the details of the aerodynamic processes which govern the operation of a Ludwig tube transonic wind tunnel. Experimental studies of the nozzle design, test section aerodynamics, the plenum volume and auxiliary flow system, test section wall and ejector flap aerodynamic loads, and the diffuser performance were made and mathematical models were formulated allowing for refinements in the configuration of the flow-conditioning channel.

The Pilot HIRT sonic nozzle flow was examined experimentally in order to assess Mach number uniformity. Wall and centerline static pressure measurements revealed differences at the nozzle entrance which were comparable with theoretical predictions. As a result, a longer sonic nozzle is suggested in order to eliminate the indicated pressure difference.

The effect of ejector flap pumping on the test section flow was investigated using a centerline pipe to obtain axial pressure distribution data. Standard deviation and the differences between average test section and plenum chamber Mach number were determined from the data as a function of free-stream Mach number and flap opening. The results revealed the inability of the particular flap design to perform satisfactorily in eliminating Mach number variations with porosity and indicated the need for longer flaps in order to improve their aerodynamic effectiveness.

The influences of the plenum volume and auxiliary flow system on the tunnel starting characteristics were studied both experimentally and theoretically. Experimentally, increasing plenum volume increased directly the tunnel start time, whereas providing excess auxiliary flow allowed for a decrease in the possible tunnel starting time. A simple theoretical model for minimum start time was formulated that confirmed the trends derived from the experimental data. Steady-state auxiliary flow requirements to attain a specific free-stream Mach number for a given flap opening were also examined.

Test section wall and ejector flap loads were determined for both the tunnel starting process and the steady-state conditions. The experimental data showed a streamwise wall load gradient during the starting process whose magnitude was a function of the main valve opening time, the response time of the plenum chamber including the effect of the flaps and the tunnel auxiliary mass flow requirements. Ejector flap loads

revealed trends similar to those for the test section walls. Theoretical models of the ejector flap and wall loads were established using empirically determined constants. The models allowed for the isolation of the important parameters governing the loading process and their effect. Steady-state loads and loads attributable to premature main valve closure were also examined and shown to be, in some cases, as severe as the starting loads.

An experimental determination of the diffuser performance of the Pilot HIRT diffuser system was undertaken. The total-pressure loss through the diffuser system was found to be primarily a function of the test section Mach number, the main valve open area, the ejector flap open area, and sector geometry. Theoretical estimates of the diffuser aerodynamic characteristics based on a one-dimensional flow model defined the optimum operating envelope of the diffuser for various tunnel flow constraints.

In summary, emphasis has been placed on understanding and describing the fundamental mechanism which governs the aerodynamic behavior of the tunnel, allowing for the establishment of meaningful performance estimates as well as design criteria for a larger scale facility.

REFERENCES

1. Ludwig, H. "Tube Wind Tunnel - A Special Type of Blowdown Tunnel." Paper Presented at the Eleventh Meeting of the AGARD Wind Tunnel and Model Testing Panel, Scheveningen, Holland, July 8-12, 1957.
2. Davis, J. W. "A Shock Tube Technique for Producing Subsonic, Transonic and Supersonic Flows with Extremely High Reynolds Numbers." Paper No. 68-18, AIAA 6th Aerospace Sciences Meeting, January 1968.
3. Whitfield, Jack D., Schueler, C. J., and Starr, Rogers F. "High Reynolds Number Transonic Wind Tunnels - Blowdown or Ludwig Tube?" Paper 29-1, AGARD-CP-83-71, August 1971.
4. Starr, R. F. and Schueler, C. J. "Experimental Studies of a Ludwig Tube High Reynolds Number Transonic Tunnel." pp. 267 Vol. 12, No. 3, AIAA Journal March 1974, Also AEDC-TR-73-168 (AD771646), December 1973.

5. Sivell, J. C. "Calculation of the Boundary-Layer Growth in a Ludwig Tube." AEDC-TR-75-118.
6. Jacocks, J. L. and Hartley, M. S. "Calibration of the AEDC-PWT 4-ft Transonic Tunnel with Modified Walls." AEDC-TR-69-134 (AD853841), June 1969.
7. Gunn, J. A. "Calibration of the AEDC-PWT Aerodynamic Wind Tunnel (4T) Using Diffuser Flap Plenum Suction." AEDC-TR-70-74 (AD867975), April 1970.
8. Starr, R. F. "Experiments to Assess the Influence of Changes in the Tunnel Wall Boundary Layer on Transonic Wall Crossflow Characteristics." AEDC-TR-75-97.
9. Jacocks, J. L. and Banks, M. R. "Cross-Flow Characteristics of Variable - Porosity Perforated Plates at Mach Numbers from 0.9 to 1.2." AEDC-TR-69-33 (AD847674), February 1969.
10. Compressed Gas Handbook. NASA SP-3045, Rev. 1970.

NOMENCLATURE

A	Test section wall flow area as defined by Eq. (6.11) or flow area
A_A	Auxiliary flow area
A_{AE}	Excess auxiliary flow area
\bar{A}_{AE}	Steady-state auxiliary flow area
A_{DE}	Flow area-plenum side of upstream edge of ejector flap
$A_{d_{max}}$	Critical valve discharge area ($N = N_{crit}$)
A_f	Flow area of flap opening
A_{ts}	Cross-sectional area of test section
A_{UE}	Flow area-plenum side of upstream edge of ejector flap
A_W	Test section wall area
a_∞	Free-stream speed of sound
CMR	Center of model rotation
c	Streamwise length of ejector flap
c_{DE}	Constant as defined in Fig. 6.31a
c_{UE}	Constant as defined Fig. 6.31a
$f(M)$	Function of Mach number as given in Eq. (7.1)
H	Test section height
K_d	Total-pressure loss factor as defined in Eq. (7.3)
k	Flow coefficient for the porous test section wall defined by Eq. (6.2)
k_f	Flow coefficient for the flap flow area defined by Eq. (6.3)

L	Test section length
M	Mach number
\bar{M}	Average Mach number
$M_{\infty \max}$	Maximum test section Mach number as defined in Fig. 7.11
N	Number of open valve ports (see Fig. 7.1)
N_{crit}	Critical number of open valve ports (see Fig. 7.9)
p	Time-varying static pressure at the test section exit, diffuser static pressure, or nozzle static pressure
p_c	Steady-state plenum chamber pressure
p_{ch}	Tunnel charge pressure
p_i	Time-varying plenum chamber pressure
p_t	Total pressure
p_{∞}	Steady-state test section static pressure
q	Dynamic pressure
R	Gas constant
T	Temperature
T_{ch}	Tunnel charge temperature
T_o	Test section stagnation temperature
T_t	Total temperature
t	Time
t_p	Theoretical time to peak wall load as given in Fig. 6.16
t_s	Tunnel start time

u	Streamwise velocity
u_f	Flow velocity through the flap open area
u_i	Equivalent flow velocity through the test section wall
V_p	Plenum volume
V_{ts}	Test section volume
\dot{w}	Mass flow rate
\dot{w}_A	Auxiliary mass flow rate (equals \dot{w}_{AS} in the steady state, see Fig. 5.3)
\dot{w}_{AS}	Auxiliary mass flow rate (steady state)
\dot{w}_{TOT}	Total tunnel mass flow rate
x	Horizontal coordinate
Y	Vertical coordinate
α_s	Sting pitch angle
γ	Ratio of specific heats
Δp	$p_i - p$
$\Delta\tau_s$	Contribution of wave spreading time to characteristic valve time
$\Delta\tau_v$	Contribution of valve opening time to characteristic valve time
δ_f	Flap gap as depicted in Fig. 7.2
μ	p_∞ / p_{ch}
ρ	Time-varying density at rear of test section
ρ_i	Plenum chamber density
σ	Standard deviation

τ	Characteristic plenum response time for $A_f = 0$, where $\tau = V_p k a_\infty / A R T$
τ_T	Characteristic plenum response time for $A_f \geq 0$, defined by Eq. (6. 7)
τ_v	Characteristic valve opening time
τ_w	Wall porosity

SUBSCRIPTS

1	Conditions at x position 1
2	Conditions at x position 2
c	Plenum chamber conditions
d	Valve port discharge conditions
e	Diffuser exit conditions
max	Maximum conditions
ss	Steady-state conditions
∞	Test section free-stream conditions

SUPERSCRIPTS

*	Critical conditions for choked flow at valve discharge
---	--